

DEVELOPMENT OF RESISTOR-BASED SILVER AND ZINC DEVICES
USING NOVEL APPLICATIONS OF INKJET PRINTING

by

ABDULAZIZ (AZIZ) NIZAR RADWAN

Submitted in partial fulfillment of the requirements
for the degree of Doctor of Philosophy

Department of Electrical, Computer and Systems Engineering
CASE WESTERN RESERVE UNIVERSITY

January, 2023

CASE WESTERN RESERVE UNIVERSITY
SCHOOL OF GRADUATE STUDIES

We hereby approve the dissertation of

Abdulaziz (Aziz) Nizar Radwan
candidate for the degree of Doctor of Philosophy.*

Committee Chair

Prof. Christian A. Zorman

Committee Member

Prof. Kath Bogie

Committee Member

Emeritus Prof. Francis Merat

Committee Member

Prof. Pedram Mohseni

Date of Defense

November 28, 2022

*We also certify that written approval has been obtained for any proprietary material
contained therein.

Table of Contents

List of Tables.....	6
List of Figures.....	7
Acknowledgements.....	15
Abstract.....	17
Chapter 1: Introduction.....	19
1.1 Inkjet Printing as a Technology for Microfabrication.....	19
1.2 Inks for Inkjet Printing.....	21
1.2.1 General Properties of Inks for Inkjet Printing.....	21
1.2.2 Commonly Used Inks in Inkjet Printing.....	22
1.3 Current Limitations of Inkjet Printing.....	24
1.4 Dissertation Overview.....	26
Chapter 2: Inkjet Printing of Resistor-based Ag Devices Using AgNO₃/Ethylene Glycol-based Inks.....	27
2.1 Introduction.....	27
2.1.1 Metal Salt-Based Inks.....	30
2.1.2 The Effect of Glycol Solvent Type.....	31
2.1.3 The Plasma Reduction Mechanism.....	33
2.1.4 Opportunities for Resistor-based Devices using AgNO ₃ /EG Inks.....	35
2.2 Process Development and Material Characterization.....	40
2.2.1 Ink Development.....	40
2.2.2 Inkjet Printing.....	41

2.2.3	Plasma Treatment.....	42
2.2.4	Material Characterization.....	44
2.3	Strain Gauge Development.....	47
2.3.1	Testing Setup.....	47
2.3.2	Strain Gauge Fabrication.....	49
2.3.3	Strain Gauge Testing.....	50
2.3.4	Analysis and Discussion.....	57
2.4	Temperature Sensors.....	67
2.4.1	Sensor Fabrication.....	67
2.4.2	Testing Setup.....	68
2.4.3	Temperature Sensor Testing.....	70
2.4.4	Analysis and Discussion.....	72
 <i>Chapter 3: Fabrication of Resistor-based Zn Devices via Selective Deoxidation of ZnO</i>		
<i>Inks by Reactive Inkjet Printing.....</i>		
3.1	Introduction.....	82
3.1.1	Zn Microparticles.....	82
3.1.2	Zn Sintering at Room Temperature.....	83
3.1.3	Reactive Inkjet Printing.....	85
3.1.4	Electrochemical Sintering of Zn by Reactive Inkjet Printing.....	86
3.1.5	Scope of this Research.....	88
3.2	Process Development.....	89
3.3	Material Characterization.....	94
3.3.1	X-Ray Diffraction.....	94

3.3.2	Scanning Electron Microscopy (SEM).....	96
3.3.3	Analysis and Discussion.....	100
3.4	Development of Zn-based Microheaters.....	102
3.4.1	Introduction.....	102
3.4.2	Development of Linear Zn-based Microheaters.....	104
3.4.3	Development of Spiral and Serpentine Zn-based Microheaters.....	107
3.4.4	Stability Testing of Zn Microheaters.....	114
3.4.5	Analysis and Discussion.....	116
3.5	Development of Zn-based RC Filters.....	117
3.5.1	Introduction.....	117
3.5.2	Design and Fabrication of Zn-based RC Filters.....	120
3.5.3	Frequency Response of Zn-based RC Filters.....	123
3.5.4	Transient Response of Zn-based RC Filters.....	126
3.5.5	Analysis and Discussion.....	129
3.6	Stability Testing of Zn-based Resistors.....	133
3.6.1	Experimental Details.....	133
3.6.2	Analysis and Discussion.....	136
	Chapter 4: Conclusions.....	138
	Appendix 1.....	146
	References.....	147

List of Tables

Table 2-1: Properties of mono-, di- and tri-ethylene glycol solvents (Radwan, Sui et al. 2022). © 2022 IEEE.....	31
Table 2-2: Summary of recent publications associated with printed Ag-based strain gauges © 2022 IEEE.....	38
Table 2-3: A summary of printed Ag-based temperature sensors.....	39
Table 3-1: Summary of recently reported printed microheaters.....	103
Table 3-2: Resistance of a rectangular sample (L = 20 mm, w = 2.5 mm) after each acetic acid print pass.....	105
Table 3-3: Temperature and power consumption of a 20 mm x 2.5 mm Zn rectangular sample.....	107
Table 3-4: A Summary of Inkjet Printed RC Filters.....	119
Table 3-5: A Summary of Other Mechanically Flexible RC Filters.....	120

List of Figures

Figure 2-1: A schematic comparison of Ag film microstructure as it relates to the vapor pressure of the ink solvent after low pressure plasma treatment.....	32
Figure 2-2: A schematic diagram showing the key steps associated with low pressure plasma treatment of AgNO ₃ /ethylene glycol inks.....	34
Figure 2-3: Sheet resistance versus plasma exposure time for AgNO ₃ inks. The blue box highlights prior work in developing highly conductive inks with an AgNO ₃ concentration of 1.5M (<i>Adapted from Sui, Hess-Dunning et al. 2022 with permission from the Royal Society of Chemistry</i>) while the orange box represents the fundamental question associated with this part of the dissertation, namely can high sheet resistance be achieved using inks with an AgNO ₃ concentration of 0.5 M.....	36
Figure 2-4: Ag strain gauge fabrication steps. (a) Ink preparation (b) Inkjet printing (c) Low temperature Ar plasma treatment (d) converted Ag strain gauge samples. (Radwan, Sui et al. 2022). © 2022 IEEE.....	41
Figure 2-5: Photographs associated with sheet resistance measurements: (a) 0.5x0.5cm ² sample for 4-point probe measurements, (b) Lucas Lab 302 SP4: 4-point probe measurement device with a mounting stand used for sheet resistance measurements. (Radwan, Sui et al. 2022). © 2022 IEEE.....	44
Figure 2-6: Sheet resistance versus plasma exposure time. (Radwan, Sui et al. 2022). © 2022 IEEE.....	46

Figure 2-7: Plan-view SEM images of strain gauge samples printed using the monoEG, diEG and triEG inks after 30 min plasma treatment (a) monoEG, (b) diEG and (c) triEG (Radwan, Sui et al. 2022). © 2022 IEEE.....47

Figure 2-8: : Photograph of the custom tensile tester. (Radwan, Sui et al. 2022). © 2022 IEEE.....48

Figure 2-9: Stress-strain curve of a 70-mm long cellophane tape sample. (Radwan, Sui et al. 2022). © 2022 IEEE.....49

Figure 2-10: Photographs of a strain gauge sample printed on a 8cm x 19mm strip of cellophane tape. The inset figure is a close-up view of the strain gauge (Radwan, Sui et al. 2022). © 2022 IEEE.....50

Figure 2-11: Resistance versus displacement for the strain gauges printed using the monoEG ink for the plasma exposure times listed in the inset.....51

Figure 2-12: Resistance versus displacement for the strain gauges printed using the diEG ink for the plasma exposure times listed in the inset.....52

Figure 2-13: Resistance versus displacement for the strain gauges printed using the triEG ink for the plasma exposure times listed in the inset.....52

Figure 2-14: Measured resistance versus cycle number for strain gauges printed using mono-, di- and tri-EG inks for a maximum strain of 0.25%. The plasma treatment for each sample was 30 minutes.55

Figure 2-15: Plan-view SEM images of strain gauges printed using the monoEG, diEG and triEG inks after cyclic load testing for 1000 cycles: (a) monoEG (b) diEG and (c) triEG.(Radwan, Sui et al. 2022) © IEEE.....56

Figure 2-16: Measured resistance versus time under ambient conditions for samples printed using monoEG, diEG and triEG inks and plasma treated for 30 minutes (Radwan, Sui et al. 2022) © IEEE57

Figure 2-17: Relative change in resistance versus relative change in length for strain gauge samples printed using the monoEG ink and plasma treated for the exposure times listed in the inset (Radwan, Sui et al. 2022) © IEEE.....59

Figure 2-18: Relative change in resistance versus relative change in length for strain gauge samples printed using the diEG ink and plasma treated for the exposure times listed in the inset. (Radwan, Sui et al. 2022) © IEEE.....60

Figure 2-19: Relative change in resistance versus relative change in length for strain gauge samples printed using the triEG ink and plasma treated for the exposure times listed in the inset. Radwan, Sui et al. 2022) © IEEE60

Figure 2-20: Gauge factor versus plasma exposure time for strain gauges printed using monoEG, diEG and triEG inks. Radwan, Sui et al. 2022) © IEEE61

Figure 2-21: Normalized change in resistance versus cycle number for strain gauges printed using mono-, di- and tri-EG inks for a maximum strain of 0.25%. The plasma treatment for each sample was 30 minutes Radwan, Sui et al. 2022) © IEEE.....65

Figure 2-22: (a) Schematic of the serpentine shaped Ag EG temperature sensor. (b) Plan-view photograph of a printed temperature sensor. Silver epoxy was applied to each pad to facilitate connection to the power source.....68

Figure 2-23: (a) Cross sectional diagram of the experimental setup. The device under test was adhered to a piece of EPSON paper which was placed on a glass slide. (b)

Photograph of the testing rig showing the cotton that was used to enhance thermal insulation of the sensor, (c) Photograph of the strip heater.....	69
Figure 2-24: (a) Infrared camera view of the strip heater under power supplied by the DC power supply, (b) Temperature vs applied voltage and current for the strip heater as measured using the infrared camera.	70
Figure 2-25: Resistance versus temperature for a temperature sensor printed using the Ag monoEG ink and plasma treated for 4, 7, 10, 13, 16, 19 and 22 minutes.....	71
Figure 2-26: Resistance versus temperature for a temperature sensor printed using the Ag diEG ink and plasma treated for 15, 20, 25 and 30 minutes.....	71
Figure 2-27: Resistance versus temperature for a temperature sensor printed using the Ag triEG ink and plasma treated for 15, 20, 25 and 30 minutes.	72
Figure 2-28: Normalized change in resistance versus temperature for temperature sensors fabricated using the monoEG ink.....	73
Figure 2-29: Normalized change in resistance versus temperature for temperature sensors fabricated using the diEG ink.....	74
Figure 2-30: Normalized change in resistance versus temperature for temperature sensors fabricated using the triEG ink.	74
Figure 2-31: TCR versus plasma exposure time for temperature sensors fabricated using the monoEG, diEG and triEG inks.	77
Figure 2-32: Cyclic thermal testing for temperature sensors fabricated using each of the ink formulations. The samples were treated under plasma exposure times that yielded a maximum TCR value for each ink formulation.	78

Figure 3-1: A plot of resistance versus time for a 60 mm x 1 mm rectangular Zn sample drop cast with acetic acid. Upon drop cast treatment, the plot shows a dramatic drop in resistance over a 180 second period. <i>Adapted from (Lee, Kim et al. 2017) with permission from John Wiley and Sons</i>	84
Figure 3-2: Concept drawing of electrochemical sintering of Zn microparticles by acetic acid using: (a) conventional drop casting and (b) the proposed reactive inkjet printing.....	88
Figure 3-3: Screen printing and reactive inkjet printing process.....	90
Figure 3-4: Resistance of rectangular pattern Zn ink versus the number of acetic acid print passes at 15, 25 and 35 μm printer drop spacing (Sui, Radwan et al. 2022).....	92
Figure 3-5: Sheet resistance of 20mm square Zn ink samples versus the number of acetic acid print passes at 15, 25 and 35 μm printer drop spacing. (Sui, Radwan et al. 2022).....	94
Figure 3-6: XRD spectra from an as-printed sample (zero print passes), a sample treated with 4 print passes, a sample treated with 8 print passes and a sample treated by manual drop casting.	95
Figure 3-7: Plan-view low, medium and high magnification SEM images of screen printed Zn structures: (a) as-printed, (b) after 4 print passes, and (c) after 8 print passes.....	97
Figure 3-8: Cross-sectional SEM images of screen printed Zn structures: (a) as-printed, (b) after 4 print passes, and (c) after 8 print passes.	99
Figure 3-9: Calculated crystallite sizes from the XRD spectra presented in Figure 3-6. The inset indicates the XRD peaks used in this analysis.	101

Figure 3-10: Illustration of particle size and crystallite size for a polycrystalline microparticle. The crystallite size is typically submicron in size. <i>Adapted from (Domi, Usui et al. 2019) with permission from John Wiley and Sons</i>	102
Figure 3-11: A 20 mm x 2.5 mm Zn ink sample on a glass slide. The sample was sat on paper for better image capture.....	104
Figure 3-12: Infrared-based temperature measurements from a linear Zn ink microheater for a range of input powers.	106
Figure 3-13: Zn Heater designs. (a) Spiral, $w = 1.3$ mm, gap = 1mm, heating area = 147 mm ² (b) Double Spiral, $w = 1.3$ mm, gap = 0.65 mm, heating area = 186 mm ² (c) Three-Turn Serpentine, $w = 1$ mm, heating area = 127 mm ² , (d) Five-Turn Serpentine, $w = 1$ mm, heating area = 204 mm ²	108
Figure 3-14: (a) As-printed 5-turn serpentine heater on a glass substrate. (b) the device after acetic acid treatment. (c) Measured resistance versus print passes for this microheater	110
Figure 3-15: (a) Infrared image at 2V (42.1°C). (b) Infrared image at 4V (75.1°C). Plot of temperature and power versus input voltage.....	110
Figure 3-16: (a) An as-printed double spiral sample printed on a glass substrate. (b) Measured resistance versus print passes for this microheater.....	112
Figure 3-17: (a) Infrared image of a double spiral heater at 5V (54.1 °C). (b) Plot of temperature and power versus input voltage.....	112
Figure 3-18: (a) Three-turn serpentine sample printed on a Kapton substrate. (b) Measured resistance versus print passes.....	113

Figure 3-19: (a) Infrared image of a three-turn serpentine sample on Kapton substrate at 4V (78.1 °C). (b) Plot of temperature and power versus input voltage.....	113
Figure 3-20: The spiral serpentine sample on Kapton substrate used in the stability test. (b) Resistance for each print pass associated with the microheater.....	114
Figure 3-21: (a) Infrared image at 2.5V (peak temperature = 44.9 °C at minute 1). (b) Infrared image after 60 minutes. Peak temperature = 45.6 °C. (c) Plot of temperature and resistance over time.	115
Figure 3-22: Photograph of a Zn RC filter printed on kraft paper.	121
Figure 3-23: Pictorial representation of the RC filter fabrication process: (a) Screen printing of the RC filter (b) Exposure of the capacitor to acetic acid using 2 print passes at a drop spacing of 15 μm (c) Exposure of the resistor to acetic acid using 1 to 6 print passes at a drop spacing of 35 μm	123
Figure 3-24: Bode plots of the RC Low Pass Filter:(a) Magnitude response (b) Phase response.....	125
Figure 3-25: Transient response of a Zn-based RC filter with an input voltage ($V_{in, \text{amplitude}} = 1.375\text{V}$) at a frequency of $\sim 20\text{kHz}$, which is less than the corner frequency of the device ($f_c = 130 \text{ kHz}$).....	128
Figure 3-26: Transient response of a Zn-based RC filter with an input voltage ($V_{in, \text{amplitude}} = 1.375\text{V}$) at a frequency of 220 kHz, which is greater than the corner frequency of the device ($f_c = 130 \text{ kHz}$).....	128
Figure 3-27: Measured corner frequency versus measured resistance obtained from the device characterized in Figure 3-24.....	130

Figure 3-28: Measured corner frequency versus the reciprocal of the resistance (R^{-1}) obtained from Figure 3-25. The fitted line shows a linear relationship with squared-R, $R^2 = 0.9957$131

Figure 3-29: Measured average corner frequency versus average resistance of the Zn-based RC filter devices evaluated in this dissertation.....132

Figure 3-30: Average corner frequency versus number of print passes for the Zn-based RC filter devices developed in this dissertation.....133

Figure 3-31: Resistance versus time for Zn samples treated using a single print pass with a drop spacing of 10 μm135

Figure 3-32: Resistance versus time for Zn samples treated using a single print pass with a drop spacing of 5 μm136

Figure A-1: Measured temperature of the plasma chamber electrodes as a function of argon plasma exposure time for RF powers of 150W and 300W (Sui, Dai et al. 2019). *Copyright of John Wiley and Sons. Reproduced with Permission from John Wiley and Sons*.....146

Acknowledgements

It all started with the realization that in order to have a promising career as a research and development engineer, I need a PhD degree. My long, eight-year PhD journey at Case Western Reserve University has been a learning experience at every step, although I faced challenges and setbacks along the way. Without the continued financial and emotional support I received from my family, friends, mentors and peers, my journey towards a PhD degree would have ended prematurely.

First of all, I would like to express my special and sincerest thanks to Prof. Christian Zorman. I took an integrated circuits fabrication class with him back in 2014, and I so admired his knowledge in that area. After keeping in touch with him a few years later and his learning that I was struggling with my first PhD dissertation project with another advisor, in the summer of 2019 he offered me the chance to join his research group and serve as my advisor. Since then, my graduate research experience has changed into a much more positive one, thanks to his guidance and mentorship. I have since become a more productive student than I thought I could be, despite the challenges associated with the Covid-19 pandemic.

Secondly, I would like to thank Prof. Kath Bogie for giving me the opportunity to collaborate with her research group at Case Western Reserve University. She also trained me on how to produce high-quality publications and how to effectively communicate technical information. Such skills are vital to succeed in my future career.

I want to thank Prof. Francis Merat and Prof. Pedram Mohseni for serving on my PhD committee. Both have been supportive and given great feedback on my work.

I also want to thank Dr. Yongkun Sui for helping me prepare my experimental setup and training me on ink development, the inkjet printer and the plasma treatment process. He has also been very responsive whenever I needed help with my labwork. He has also been a great collaborator that I always enjoyed working with.

I want to thank my collaborators, Dr. Dhruv Seshadri and Nicolas Bianco. Both are intelligent, easy to work with, respectful and productive. I have learned many things from them such as lab equipment use and data summary and presentation. Both are also good friends of mine and we socialized occasionally.

I want to thank Angela Beca, Cynthia Hatcher, Heather Smith, Brooke Berger, Christine Hale, Salvatore Russo, Laura Kuhar and Sheila Campbell for their help in the administrative matters associated with my time in graduate school, all of whom were professional, responsive and friendly.

I would like to thank the Advanced Platform Technology at the Louis Stokes Veteran Affairs Medical Center through contract# VA250-17-P-4574 for access to the Dimatix DMP3000 inkjet printer and the supplies required to operate it.

Lastly, I would like to thank my parents and family for their unconditional love and support throughout my early and adult life. Without them, I would never have achieved my personal as well as my professional goals.

Development of Resistor-based Silver and Zinc Devices Using Novel Applications of Inkjet Printing

Abstract

by

AZIZ NIZAR RADWAN

This dissertation reports the development of resistor-based electronic devices fabricated using novel approaches to inkjet printing. The first component of this dissertation involves the development of resistor-based devices using particle-free inks comprised of AgNO_3 and ethylene glycol (EG) with low-pressure Ar plasma to form metallic structures. The AgNO_3 concentration was selected to produce Ag structures with sheet resistances between 10^5 and $10^1 \Omega/\square$ depending on plasma duration and the EG solvent type used in the ink. To investigate the relationships between ink composition, plasma parameters and device performance, strain gauges and temperature sensors were printed from inks that use one of three forms of EG, differing in their vapor pressure. For the strain gauges, the gauge factor (GF) depends on plasma duration and ink solvent. For each solvent, the GF decreases with increasing plasma duration. Additionally, the GF exhibited a strong dependence on the vapor pressure of the solvent with the highest GFs associated with the lowest vapor pressure. Material analysis revealed strong connections between porosity and ink solvent, establishing a

physical basis linking ink solvent to GF. The temperature coefficient of resistance (TCR) for the temperature sensors was generally found to be insensitive to plasma exposure time but strongly dependent on ink solvent. The highest TCR values were associated with the ink having the highest vapor pressure solvent and thus the lowest porosity.

The second component of this dissertation involves the development of reactive inkjet (RIJ) printing for acetic acid-based electrochemical sintering of screen-printed Zn devices in order to control electrical resistance during the sintering step. Sheet resistances range from 2×10^5 to $0.5 \Omega/\square$ depending on drop spacing and number of print passes. SEM images show that cold welding between Zn particles increases with increasing print passes, consistent with sheet resistance measurements. Zn microheaters made using the RIJ process compare favorably to conventional microheaters. The RIJ process enables the fabrication of the resistor and capacitor in a resistor-capacitor (RC) filter from a single Zn layer. The corner frequency varies from ~ 7 kHz to ~ 1 MHz as determined by the printing parameters used to form the resistor.

Chapter 1

Introduction

1.1 Inkjet Printing as a Technology for Microfabrication

Inkjet printing technology for electronic device applications can trace its roots to the development of office computers in the mid-20th century when digital printing directly from computer programs began to replace the manual typewriter for the production of paper-based documents. (Cummins and Desmulliez 2012). Inkjet printing has since been scaled up for use in office and home-based desktop publishing, customized advertising and packaging. In recent years, the same basic technological approach has been developed to print a wide range of electronic devices that were previously fabricated using conventional lithographic techniques, such as printed circuit board (PCB) assemblies and flexible electronic devices. (Cummins and Desmulliez 2012).

One of the most salient advantages of inkjet printing is that it offers an additive manufacturing alternative to the inherently subtractive approach that currently dominates microfabrication; an approach that involves thin film deposition, followed by photolithographic patterning, and then by material removal through chemical and/or plasma etching. Inkjet printing offers a maskless, direct-write additive

manufacturing alternative to microdevice fabrication with the potential for highly efficient, low cost and eco-friendly electronic component manufacturing (Cummins, 2012, Nayak, 2019, Gao, 2017).

A commonly used inkjet printing method is drop on demand (DOD) printing, in which printheads dispense inks when and where required. A digitally controlled piezoelectric actuator is used to dispense the droplets. Modern printheads are highly miniaturized and thus are capable of dispensing pico-liter scale droplets on substrates, with typical line widths of 20 to 100 μm for production-grade systems. The inkjet nozzles utilize microelectromechanical systems (MEMS)-based technologies that enable parallelization with an independent actuation mechanism. This attribute makes inkjet printing systems scalable for high throughput industrial manufacturing applications (Jabari, 2019, Hansen, 2013).

One of the most significant limitations to inkjet printing is the minimum feature size that can be printed. The minimum producible feature size on a research-grade printer is on the order of $\sim 5 \mu\text{m}$ (Cummins and Desmulliez 2012). By comparison, the minimum feature size is ~ 1 to $2 \mu\text{m}$ for the i-line and g-line photolithographic processes used in microelectromechanical systems (MEMS) fabrication and 5 nm for the extreme ultraviolet lithography processes used in state-of-the art silicon integrated circuit production (Cutress 2020). Ultimately, print resolution currently prohibits inkjet printing from becoming a universal replacement for conventional photolithography in microelectronics production. However, inkjet printing is well suited for wearable sensors, biosensors and planar energy devices such as micro-batteries and micro-supercapacitors where large surface area and/or large volume

structures are required for high quality signal transduction (Phuah, Hart et al. 2020, Yang and Fan 2020). Inkjet print is also well suited for rigid and flexible circuit board production where large feature size and high throughput manufacturing are valued.

1.2 Inks for Inkjet Printing

1.2.1 General Properties of Inks for Inkjet Printing

Inks for inkjet printing consist of liquid phase compositions or particulate materials dissolved in solvents. For inkjet printing, it is crucial to prepare a jettable, printable ink that is compatible with a variety of substrates. The formation, impact and spreading of droplets are determined by the rheological properties of the ink, which include viscosity, density and surface tension (Nayak, Mohanty et al. 2019).

Surface tension and viscosity can be simultaneously assessed using the Ohnesorge number (Nayak, Mohanty et al. 2019), which is a dimensionless quantity relating viscous forces to surface tension and inertial forces. The former is mathematically related to the Reynolds number while the latter is related to the Weber number. Hence, the Ohnesorge number (Derby 2010, Cummins and Desmulliez 2012) is given by:

$$Oh = \frac{\sqrt{We}}{Re} \quad (1)$$

and the Weber number can be calculated using:

$$We = \frac{\rho V^2 L}{\sigma} \quad (2)$$

where ρ is the density, V is the droplet velocity, L is the nozzle diameter, and σ is the surface tension. The Reynolds number is defined by:

$$Re = \frac{\rho VL}{\eta} \quad (3)$$

where η is the fluid viscosity.

Typically, the ink viscosity must be relatively low (range of 1-25 mPa) and the surface tension must be sufficiently high (over 20 mNm⁻¹) in order for a droplet to detach from the nozzle. A proper range of surface tension and viscosity is required for a printable fluid. Brian (Derby 2010) developed a model to determine the range of Ohnesorge numbers yielding printable fluids. Ink solvents play a significant role in achieving the proper range of viscosity and surface tension for successful printing.

Inkjet printing systems are compatible with different types of conductive inks such as metallic nanoparticle inks, organometallic inks and conductive polymer inks. These ink types can either be dissolved or dispersed. The conductive material choice is determined by a number of factors such as physical properties, optical transparency, adhesion to substrates and electrical conductivity. (Kamyshny, 2014, Cummins, 2012, Nir, 2010).

1.2.2 Commonly Used Inks in Inkjet Printing

1.2.2.1 Metal-Organic Decomposition Inks

Metal-Organic Decomposition (MOD) inks are a classification of conductive inks containing metals in their ionic state (Choi, 2019). As the name implies, MOD inks involve an inorganic material that is dissolved in an organic material in order for the former to decompose and, in turn, form a jettable ink (Schoner, 2011). MOD inks are commercially available and are comparatively inexpensive. Noticeable advantages of MOD inks include their low temperature sintering requirement, jetting stability and

long shelf life. However, it is difficult to form thick films with MOD inks as their volume is considerably lost after sintering (Zapka, 2017). In addition, adjusting their viscosity is more limited than other types of inks since their metallic constituents do not readily dissolve in solvents. Commonly used MOD inks are silver-MOD inks whose precursor is silver acetate, and copper-MOD inks with copper formate as the metallic precursor (Choi, 2019).

1.2.2.2 Metallic Nanoparticle Inks

Metallic nanoparticle inks comprise the largest and most commonly used class of metallic ink in inkjet printing. As the name implies, metallic nanoparticle inks contain metallic particles with diameters that are typically less than 50 nm. Reducing the particle size to the nanoscale leads to changes in the characteristics of the metal relative to bulk properties, such as a reduction in the melting point, enhanced surface-atom reactivity and distinct optical properties (Kamyshny, 2005, Bermel, 1999, Lue, 2001, Fedlheim, 2001). Silver (Ag), gold (Au) and copper (Cu) are examples of metallic nanoparticle inks that are commercially available. These inks are popular due to their ability to produce high conductivity structures at relatively low cost. Ag nanoparticle inks are the most commonly used nanoparticle ink owing to their lower cost relative to Au and lower oxidation rate compared to Cu. Also, Ag nanoparticle inks are generally characterized by a high degree of nanoparticle dispersion in the solvent, making them particularly compatible with printing (Nayak, 2019).

In most cases, Ag nanoparticle inks require a high temperature anneal (> 100°C) after printing in order to produce electrically conductive structures. Therefore,

the selection of substrates is limited to those that exhibit high thermal stability. Examples of thermostable, flexible substrates used in inkjet printing include polyethylene terephthalate (PET) (Briand and Opera, 2011), polyethylene naphthalate (PEN) (Briand and Opera, 2011) and polyimide (PI) (Briand and Oprea, 2011), all of which have been used in fabricating capacitive and resistive devices (Briand and Molina, 2011). Other attractive substrates for flexible electronics include polyvinyl alcohol (PVA) (Jang, 2017) and polycaprolactone (PCL) (Annese, 2014), which are cost effective and have unique chemical properties. However, PVA and PCL have relatively low melting points ($< 200^{\circ}\text{C}$) making them incompatible with Ag nanoparticle inks from a processing perspective. Hence, there is a compelling need to develop inks that do not require high temperature annealing.

1.3 Current Limitations of Inkjet Printing

Although inkjet printing has proven to be an effective method to produce high quality electrical conductors for use in printed circuit boards, radio frequency identification (RFID) systems and other electronic devices, three issues currently limit its expanded use in the fabrication of sensors and other technologies that could benefit from what inkjet printing has to offer. The first issue relates to the electrical conductivity of inkjet-printed structures. Process development has thus far focused on achieving metallic structures with high electrical conductivity. While these metals are used in sensors, their low resistivity largely restricts their use to transduction techniques that utilize high conductivity electrodes. As such, the number of inkjet printing processes designed specifically for resistor-based metallic devices is

significantly lacking. The second issue relates to the process temperatures associated with metallic inks. To achieve high conductivity, structures printed using metallic inks require the use of a post print thermal annealing step at temperatures $>100^{\circ}\text{C}$ which limits the use of polymer substrates to a small number that are tolerant to high temperature exposure. The third issue relates to the variety of metals that can be printed using inkjet printing processes. As mentioned previously, the three most commonly printed metals are Ag, Au and Cu. While these metals are sufficient for high-conductivity structures, this small pallet limits inkjet printing compared to other methods such as sputtering. This pallet could be expanded if the use of inkjet printing were itself expanded beyond a method to dispense inks. Another printing method used in electronic device fabrication is screen printing; a simple, flexible and economical printing method used to fabricate thick films typically in the range of $100\ \mu\text{m}$ (Rudez, 2015). The process typically requires a screen mesh with a patterned aperture, a squeegee and a viscous ink. The composition and rheology of inks are critical in producing quality screen printed films (Trease, 1972, Thibert, 2014, Somalu, 2017). A list of screen-printed electronic devices from a wide range of materials includes batteries (Tehrani, 2015), antennas (Shin, 2009), heaters (Zeng, 2019) and pressure sensors (Grabner, 2017). Approaches that seek to pair inkjet printing with screen printing have the potential to add materials to the inkjet printing pallet that do not currently exist in an ink suitable for inkjet printing.

1.4 Dissertation Overview

In an effort to address the aforementioned issues facing inkjet printing, this dissertation focuses on the development of two distinct approaches that advance the use of inkjet printing as a platform additive manufacturing technique for printed sensor and sensor-related devices on temperature-sensitive substrates. The first approach addresses a technology gap in ink technology by centering on the development of inkjet-printed, resistor-based devices using novel particle-free inks based on AgNO_3 as the metal precursor and chemically different forms of ethylene glycol as the ink solvent. This part of the dissertation explores the relationship between ink solvent, microstructure and device performance by fabricating resistor-based temperature and strain sensors utilizing three distinct molecular forms of ethylene glycol as the solvent. From a technology perspective, this project will focus on processes that keep substrate temperatures below 100°C in order to be compatible with a much broader set of polymer substrates than the state-of-the-art.

The second approach seeks to advance the development of a printing technology for the Zn-based devices, focusing on the development of inkjet printing to perform selective chemical deoxidation of native oxide on Zn particles to form metallic Zn structures by electrochemical sintering. This part of the dissertation specifically focuses on the formation of Zn structures by precision dispensing of acetic acid on screen-printed ZnO structures and explores the relationships between key printing parameters and electrical resistivity of the resulting Zn structures. To demonstrate the utility of the process, a variety of resistor-based Zn devices, including microheaters and RC filters will be fabricated and characterized.

Chapter 2

Inkjet Printing of Resistor-based Ag Devices Using AgNO₃/Ethylene Glycol-based Inks

2.1 Introduction

Flexible sensors play a critical role in a wide variety of applications, including and most notably, wearable technology (Lee and Chung 2009, Pantelopoulos and Bourbakis 2009, Patel, Park et al. 2012). These sensors, in particular flexible devices that utilize metallic sensing elements, are increasingly being fabricated using additive manufacturing (AM) processes. Arguably the most common AM method to fabricate metallic device structures is inkjet printing as it offers a great deal of flexibility at the design and fabrication stages with relatively low cost tooling requirements, and hence is straightforward to implement. Inkjet printing is compatible with both rapid prototyping and large-scale manufacturing (Courbat, Kim et al. 2011, Molina-Lopez, Quintero et al. 2012, Mattana, Kinkeldei et al. 2013, Aliane, Fischer et al. 2014).

Unlike conventional microfabrication which utilizes vacuum-based physical vapor deposition (PVD) and photolithography, inkjet printing is a direct-write technique carried out under ambient conditions, and therefore requires significantly less capital investment. PVD requires multiple fabrication pre-steps including photoresist spin-coating, ultraviolet exposure and photoresist developing whereas inkjet printing requires only a single step to deposit a patterned metallic structure. Also, PVD works under vacuum conditions while inkjet printing works under ambient conditions. Because ink formulations can be readily customized to meet the requirements for a particular application, inkjet-printed devices can have performance characteristics that are challenging to realize in devices fabricated using conventional PVD.

Nanoparticle inks comprise the largest and most commonly used class of metallic ink in inkjet printing. Silver (Ag) nanoparticle inks are used in this class due to their low cost, ease of use and long-term stability. In most cases, Ag nanoparticle inks require a high temperature anneal ($> 100^{\circ}\text{C}$) after printing in order to produce electrically conductive structures. Therefore, the selection of substrates is limited to those that exhibit high thermal stability. Examples of thermostable, flexible substrates used in inkjet printing include polyethylene terephthalate (PET) (Jahn, Blaudeck et al. 2010), polyethylene naphthalate (PEN) (Jahn, Blaudeck et al. 2010) and polyimide (PI) (Briand, Oprea et al. 2011, Choi, Seong et al. 2019), all of which have been used in fabricating capacitive and resistive devices (Briand, Molina-Lopez et al. 2011). Other attractive substrates for flexible electronics include polyvinyl alcohol (PVA) (Jang and Han 2017) and polycaprolactone (PCL) (Annese, De Venuto et al. 2014) which are cost effective and have unique chemical properties. However, PVA and PCL

have relatively low melting points ($< 200^{\circ}\text{C}$) making them incompatible with Ag nanoparticle inks from a processing perspective. Hence there is a compelling need to develop inks that do not require high temperature annealing to form conductive structures.

As an alternative to nanoparticle suspensions, our group has recently reported the development of a particle-free Ag ink consisting of silver nitrate (AgNO_3) mixed with an ethylene glycol-based solvent (Sui 2019, Sui and Zorman 2020). A low temperature ($< 100^{\circ}\text{C}$), argon (Ar) plasma reduction process is utilized to convert AgNO_3 to metallic Ag. This process eliminates the need for the high temperature thermal annealing step associated with Ag nanoparticle inks.

Previous reports by our group document the use of the plasma reduction process to fabricate a variety of Ag-based devices from AgNO_3 /ethylene glycol inks including thermistors (Sui, Kreider et al. 2019), RC filters (Ghosh 2017), and hydrogen peroxide sensors (Sui, Hess-Dunning et al. 2020). These devices were fabricated using plasma conditions designed specifically to obtain the highest achievable electrical conductivity in the printed structures. Although it was noted in these investigations that the electrical resistance of the printed structures was dependent on plasma exposure time, these studies did not seek to utilize this information to investigate the possibility of creating sensors that exploit the resistivity of the printed structures. This dissertation builds upon that work by exploring mechanisms to tune the resistivity of the printed structures by expanding the pallet of solvents used in the AgNO_3 -based ink beyond ethylene glycol. The connections between ink solvent, plasma processing conditions, electrical resistivity and device performance are evaluated in two printable

devices that rely heavily on the electrical resistance of their sensing elements, namely strain gauges and temperature sensors.

2.1.1 Metal Salt-based Inks

Metal salt-based inks are particle-free inks comprised of an inorganic metal salt dissolved in aqueous or organic solvents. The precursor salt consists of a polyatomic ionic compound that is soluble in an organic solution. For inkjet printing, the viscosity of the ink can be modified by additives such as deionized water in order to tune the ink jettability for a particular printing system. In contrast to metallic nanoparticle inks, metal salt-based inks do not utilize conventional high temperature ($> 100^{\circ}\text{C}$) thermal annealing after printing. Instead, the inks are activated using a low pressure (650 mTorr), low temperature ($< 100^{\circ}\text{C}$) argon plasma. Metallic structures are produced by interactions with argon ions as well as plasma-generated electrons (Sui 2019).

Metal salt-based inks have been developed for a wide range of technologically useful metals including silver (Ag), copper (Cu), palladium (Pd), platinum (Pt), bismuth (Bi), lead (Pb) and tin (Sn) (Sui 2019). Unlike metal nanoparticle inks that are made using complex synthesis methods, metal salt-based inks are comprised of commercially available, off-the-shelf metal salts (*i.e.*, AgNO_3) and ethylene glycol-based solvents and thus can be made at the point of use. Also, because metal-salts readily dissolve in ethylene glycol, the average shelf life of these inks greatly exceeds typical nanoparticle suspensions.

In Sui's dissertation (Sui 2019), it was found that the resistivity of structures printed using inks with a AgNO_3 concentration of 1.5M were among the lowest (6.11

$\mu\Omega\cdot\text{cm}$) compared to structures made using Pt-, Cu- and Sn-salt based inks. The crystallinity of the reduced Ag structures was found by x-ray diffraction to resemble bulk silver. Three Ag-salt based devices were developed using this ink, namely an RC filter (Sui, Ghosh et al. 2018), a thermistor (Sui, Kreider et al. 2019) and a hydrogen peroxide sensor (Sui, Hess-Dunning et al. 2022).

2.1.2 The Effect of Glycol Solvent

A component of the hydrogen peroxide sensor work by Sui (Sui, Hess-Dunning et al. 2022) involved an investigation as to whether the vapor pressure of the glycol solvent played a significant role in the plasma-liquid interactions during the plasma reduction process. Three types of glycol solvents were investigated: monoethylene glycol (monoEG), diethylene glycol (diEG) and triethylene glycol (triEG). Table 2-1 compares the density, viscosity, vapor pressure and boiling point of each of these glycol solvents (Diethylene Glycol 2021, EGF 2021, Glycol 2021, Glycol 2021, Triethylene-glycol-for-synthesis 2021). These three molecular forms of EG were selected because, while chemically similar, they differ significantly in vapor pressure

Table 2-1: Properties of mono-, di- and tri-ethylene glycol solvents. (Radwan, Sui et al. 2022). © 2022 IEEE.

<i>Organic Solvent</i>	<i>Vapor Pressure (mm Hg)</i>	<i>Viscosity (cP)</i>	<i>Boiling Point (°C)</i>	<i>Density (g/cm³)</i>	<i>Ref</i>
<i>Monoethylene Glycol</i>	0.12 at 20 °C	21	196	1.112	(EGF 2021)
<i>Diethylene Glycol</i>	0.006 at 20 °C	38	245	1.118	(Diethylene Glycol 2021, Glycol 2021)
<i>Triethylene Glycol</i>	0.00075 at 25 °C	48	285	1.120	(Glycol 2021, Triethylene-glycol-for-synthesis)

and thus presumably should exhibit different levels of stability during the plasma exposure process.

During the plasma conversion process, low-vapor pressure glycol solvents (*i.e.* diEG and triEG) extend the plasma-liquid interaction time in the AgNO₃ ink relative to high vapor pressure solvents (Sui, Hess-Dunning et al. 2022). During plasma exposure, solvated components, including Ag⁺ and NO₃⁻, diffuse through the liquid ink and interact with the plasma resulting in the production of solvated electrons, hydroxide and hydrogen radicals (Chen, Li et al. 2015, Rumbach, Bartels et al. 2015). The interaction of Ag⁺ with solvated electrons leads to the formation of metallic porous Ag structures by reactions that depends on the longevity of the ink solvent in the low-pressure plasma. As illustrated in Figure 2-1, lower vapor pressure solvents lead to longer plasma-liquid interaction and thus more porous structures after the plasma conversion process whereas high vapor pressure solvents yield dense structures

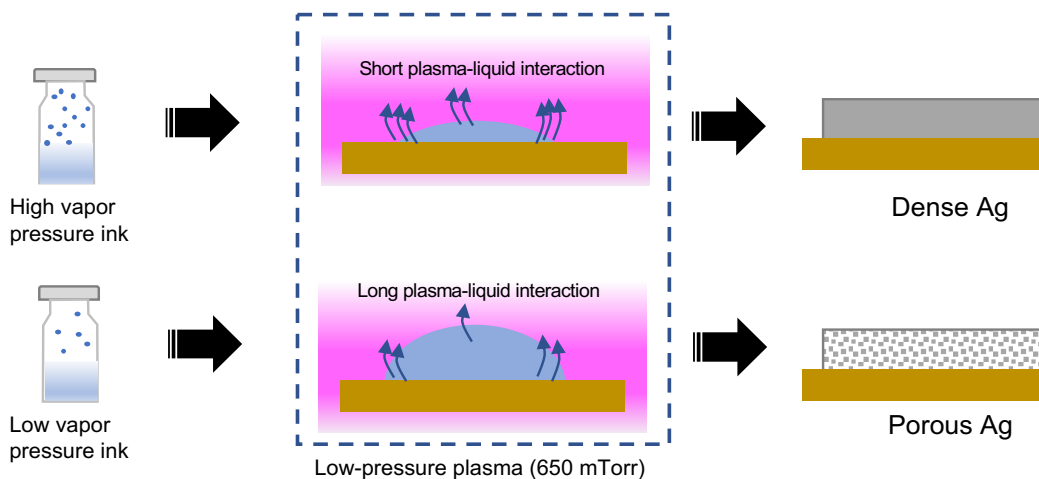


Figure 2-1: A schematic comparison of Ag film microstructure as it relates to the vapor pressure of the ink solvent after low pressure plasma treatment.

2.1.3 The Plasma Reduction Mechanism

Plasma is a form of ionized gas containing high energy electrons and ions that make the energized gas electrically conductive. Ionization is typically performed in an electric field and occurs when there are sufficiently high temperatures within the plasma due to collisions between plasma components. Plasma properties are dominated by electrical and/or magnetic forces. Because of this, plasma conducts electrical currents and reacts to electromagnetic fields (Piel 2017). A commonly used gas in low pressure plasmas is Argon (Ar) gas. Argon is chemically inert and relatively easy to ionize, forming positively charged ions (Ar^+). Argon is normally colorless, but when it is ionized in an electric field, it glows violet or purple.

Figure 2-2 is a schematic diagram showing the key steps associated with low pressure plasma treatment of AgNO_3 /ethylene glycol inks (Sui 2019). During ink synthesis, AgNO_3 in the glycol solvent dissociates into Ag^+ and NO_3^- ions. During plasma exposure, electrons from the plasma dissolve in the solvent. These solvated electrons engage in reduction reactions with the Ag^+ ions forming neutral Ag atoms. Neutral Ag atoms nucleate within the ink, forming solid Ag nuclei, which eventually coalesce to form solid structures. Concurrently, Ar^+ bombardment heats the substrate, accelerating the evaporation of both the glycol solvent and NO_3^- , and also accelerating the Ag-Ag reactions. The aforementioned reactions require the presence of the solvent. The solvent with the lowest vapor pressure survives the longest in the plasma and vice versa. The microstructure of the resulting Ag structures depends on reactions within the solvent. Consequently, the microstructure depends strongly on the vapor pressure of the ink solvent, with triEG inks producing the most porous films while monoEG

inks producing the densest films under the same plasma treatment conditions. Consequently, the selection of ink solvent can be used to “tune” the microstructure of the Ag films.

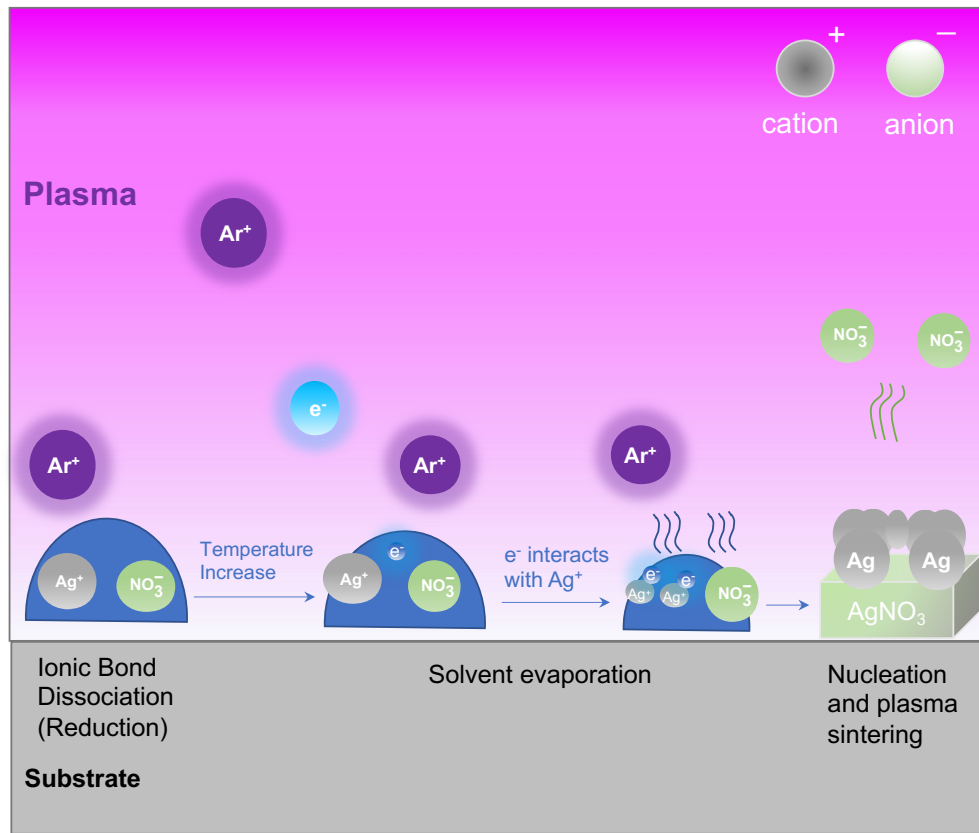


Figure 2-2: A schematic diagram showing the key steps associated with low pressure plasma treatment of AgNO₃/ethylene glycol inks.

2.1.4 Opportunities for Resistor-based Devices using AgNO₃/EG Inks

Figure 2-3 compares the current state of development for AgNO₃/EG based inks with that to be investigated in this dissertation. Previous work (enclosed in the blue box) focused on inks using monoEG, diEG and triEG solvents and a AgNO₃ concentration of 1.5M (Sui, Hess-Dunning et al. 2022). The highest sheet resistances were observed for the Ag monoEG, diEG and triEG inks after plasma exposure times of 5 min, 10 min and 15 min, respectively. As the plasma exposure time was increased to 30 min, the sheet resistance of all solvents decreased significantly, converging to $\sim 0.025\Omega/\square$, which is only threefold that of sputtered Ag. The objective of that work was to develop a hydrogen peroxide sensor, which utilizes electrochemical transduction. Consequently, the conductivity of the sensing electrodes had to be sufficiently high to improve the electron transfer rate and hence improve electrochemical sensitivity.

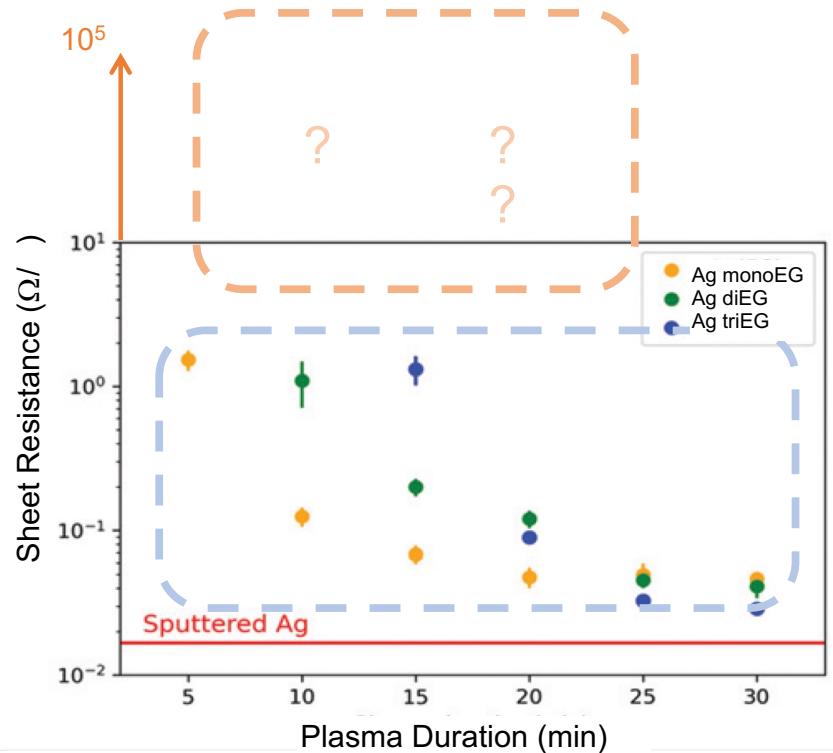


Figure 2-3: Sheet resistance versus plasma exposure time for AgNO₃ inks. The blue box highlights prior work in developing highly conductive inks with an AgNO₃ concentration of 1.5M (*Adapted from Sui, Hess-Dunning et al. 2022 with permission from the Royal Society of Chemistry*) while the orange box represents the fundamental question associated with this part of the dissertation, namely can high sheet resistance be achieved using inks with an AgNO₃ concentration of 0.5 M.

It can be observed in Figure 2-3 that the sheet resistance of structures printed using the 1.5M AgNO₃-based inks is tunable using plasma exposure time as a control parameter. The sheet resistances associated with the three solvents decreased from ~2 Ω/□ to ~0.025Ω/□ as plasma duration increased from 5 to 30 min. These sheet resistances are all relatively low because of the high AgNO₃ concentration in the inks. Unfortunately, even the highest of these sheet resistances is too low for resistor-based devices. For resistor-based devices, a far more desirable range of sheet resistances is

enclosed in the orange box in Figure 2-3. A principal hypothesis of this dissertation is that much higher sheet resistances can be achieved without compromising the relationship between ink solvent and microstructure by simply reducing the concentration of AgNO_3 in the ink. In this dissertation, a AgNO_3 concentration of 0.5M was used in monoEG, diEG and triEG inks. The sheet resistance and microstructure of printed structures as a function of plasma exposure time were assessed and resistor-based strain gauges and temperature sensors were fabricated to evaluate the utility of these inks to fabricate resistor-based devices from inkjet printed metallic films.

One of the most common sensors fabricated by inkjet printing is the metal strain gauge (Sui, Dai et al. 2019). Strain gauge performance is evaluated by assessing the device gauge factor. A notable advantage of inkjet printing is that it offers the potential to create metal structures with a range of electrical conductivities, thus facilitates more design options and improved strain gauge performance than their conventional counterparts (Borghetti, Serpelloni et al. 2016). Table 2-2 summarizes recently published strain gauges fabricated by inkjet printing. The reported gauge factors ranged from 1 to 8, with most around 2. Apart from a process that used direct electrical sintering of the printed structures (Kravchuk, Bobitski et al. 2016), all inks required that the substrate be heated to $\geq 100^\circ\text{C}$ after printing (Zlebič, Zivanov et al. 2016, Abu-Khalaf, Al-Ghussain et al. 2019, Silva, Paisana et al. 2020, Zhu, Qian et al. 2020). This ultimately restricts the selection of substrate material to those that can tolerate high processing temperatures. This significantly impacts the use of inkjet printing to fabricate strain gauges on flexible polymer substrates. A principal objective of this

dissertation is to achieve a printable strain gauge with a gauge factor approaching 8 using a plasma reduction process that does not raise the substrate temperature above 140 °C. A substantial portion of the following strain gauge development, results and analysis contents can be found in (Radwan, Sui, et al. 2021, Radwan, Sui et al. 2022)

© 2021 IEEE © 2022 IEEE.

Table 2-2: Summary of recent publications associated with printed Ag-based strain gauges. (Radwan, Sui et al. 2022). © 2022 IEEE.

<i>Reference</i>	<i>Particle size (nm)</i>	<i>Structure</i>	<i>Substrate Temperature during Sintering</i>	<i>Substrate</i>	<i>Max. Applied Strain</i>	<i>GF</i>
(Zlebić, Zivanov et al. 2016)	N/A	Lines	100 °C for 30 min	Polyimide	1% Strain	1 to 2
(Silva, Paisana et al. 2020)	20	Grid	140 °C for 10 min	Poly-urethane (gloves)	30% Strain	2
(Abu-Khalaf, Al-Ghussain et al. 2019)	180	Line & Horseshoe	110 °C for 60 min	PDMS	10% Strain	2
(Kravchuk, Bobitski et al. 2016)	30	Serpentine	2 sintering methods: a) 250 °C for 60 min b) Electrical sintering for < 5s	DuPont (Polyimide)	N/A	2.6 (electrical sintering) 2.9 (thermal sintering)
(Zhu, Qian et al. 2020)	100	Grid	150 °C	Teslin	1% Strain	8

A second device commonly fabricated by inkjet printing is the temperature sensor. Table 2-3 reviews key attributes and performance characteristics of recently published temperature sensors fabricated by inkjet-printing. Post print annealing temperatures range from room temperature to 290°C while the temperature coefficients of resistance (TCR) range from 9.06×10^{-4} to $2.99 \times 10^{-3} \text{ }^\circ\text{C}^{-1}$. For reference, the TCR of bulk Ag is $3.8 \times 10^{-3} \text{ }^\circ\text{C}^{-1}$. Ag temperature sensors fabricated by means other than inkjet printing have not been reported. A principal objective of this dissertation is to develop a printable temperature sensor with a TCR of $\sim 2 \times 10^{-3} \text{ }^\circ\text{C}^{-1}$ using a plasma reduction process that does not raise the substrate temperature above 140 °C.

Table 2-3: A summary of printed Ag-based temperature sensors

<i>Ref</i>	<i>Particle size</i>	<i>Sintering Temperature</i>	<i>Substrate</i>	<i>Operating Temperature</i>	<i>Nominal Resistance</i>	<i>TCR ($^\circ\text{C}^{-1}$)</i>
<i>This work</i>	N/A	<100 °C	Cellophane	20 – 60 °C	Varies	1.7×10^{-3}
<i>(Barmpakos, Segkos et al. 2018)</i>	20 nm	Let dry after printing for 14 days	Glossy photo-paper	25 – 75 °C	N/A	9.06×10^{-4}
<i>(Courbat, Kim et al. 2011)</i>	≤ 50 nm	@150 °C for 60 min	Raw paper coated with oxide film	-20 – 60 °C	600-710Ω	1.1×10^{-3}
<i>(Felba, Nitsch et al. 2009)</i>	6 nm	Sintered at 250 °C for 1 hour	Glass slides	20 – 200 °C	1 Ω	2.08×10^{-3}
<i>(Dankoco, Tesfay et al. 2016)</i>	N/A	1st step: drying solvent 130 °C for 10 min 2nd step: 150 °C for 30 min	Kapton® (Polyimide)	20 – 60 °C	2 kΩ	2.27×10^{-3}
<i>(Mattana, Kinkeldei et al. 2013)</i>	< 150nm	Annealed at 290 °C for 30 min	Kapton®	10 – 80 °C	52 Ω	2.99×10^{-3}

2.2 Process Development and Material Characterization

The experimental work for this part of the dissertation involves process development and basic materials characterization of printed structures made using inks comprised of monoethylene glycol (monoEG), diethylene glycol (diEG), and triethylene glycol (triEG), followed by fabrication of strain gauge and temperature sensor devices to explore the connections between ink composition, material properties and device performance.

2.2.1 Ink Development

Figure 2-4 schematically describes the inkjet printing process which involves ink synthesis, printing and plasma treatment. Silver nitrate (AgNO_3), a common inorganic silver-containing salt, was used as the metal precursor. The ink solvent consisted of deionized water mixed with either monoethylene glycol (monoEG), diethylene glycol (diEG) or triethylene glycol (triEG). As shown previously in Table 2-1, these three molecular forms of EG, while chemically similar, differ significantly in vapor pressure and thus exhibit different levels of stability during the plasma exposure process. Inks comprised of monoEG are least stable under vacuum conditions while inks comprised of triEG are most stable. Three silver ink types were made, Ag/moEG, Ag/diEG and Ag/triEG. The Ag inks were prepared by mixing 1.7g of silver salt (AgNO_3 , 98% purity, Alfa Aesar Co., Massachusetts, USA) with 16mL of the glycol-based solvent and 4mL of deionized water in a vial in order to form inks with a molarity of 0.5M. The mixture was then stirred for 15 minutes. The Ag salt

was left to dissolve in the solvent for 24 hours. Deionized water was used to match the viscosity and surface tension of the ink to the requirements of the inkjet printer.

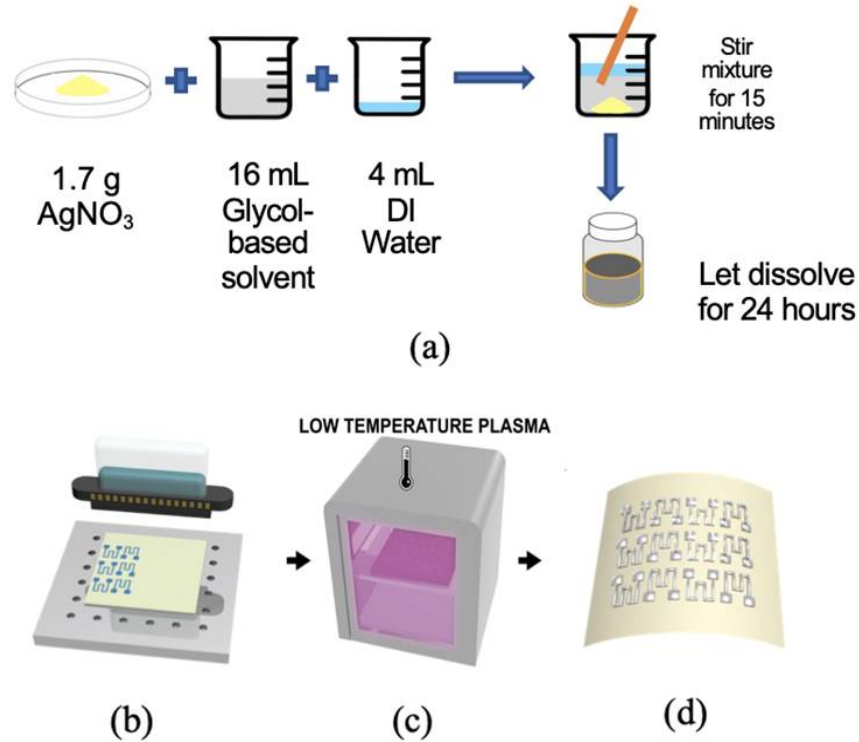


Figure 2-4: Ag strain gauge fabrication steps. (a) Ink preparation (b) Inkjet printing (c) Low temperature Ar plasma treatment (d) converted Ag strain gauge samples. (Radwan, Sui et al. 2022). © 2022 IEEE.

2.2.2 Inkjet Printing

Silver structures were printed using a Dimatix DMP3000 series inkjet printer. The DMP3000 is a production-grade inkjet printer equipped with a DMC-11610 cartridge and a 12 x 12 in² platen for printing on large area substrates. Using a syringe, the Ag ink was loaded into the print cartridge which is designed to produce 10 pL droplets. The printer drop spacing was set at 15 μm and the platen temperature was set at 50°C for Ag/monoEG, 43°C for Ag/diEG, and 41°C for Ag/triEG inks to

produce uniform patterns on cellophane substrates. The heated platen facilitates evaporation of the deionized water while leaving the EG solvent virtually unaffected. The nozzle voltage was set at between 28 and 30V. Multiple, consecutive nozzles were activated simultaneously to print a single strain gauge structure within 5-6 minutes. Cellophane tape was selected as the flexible substrate material due to its chemical compatibility with EG (EG is used as a plasticizer in cellophane (Morris 2016)), favorable wetting properties of these ink formulations on cellophane substrates, compatibility with the Ar-based plasma reduction process and extensive prior experience by our group in using cellophane as a substrate (Sui, Ghosh et al. 2018, Sui, Kreider et al. 2019). Moreover, the adhesive properties of cellophane tape make it an attractive substrate for inkjet printed “stick-on” sensors. To facilitate handling, cellophane tape substrates were adhered to rigid glass slides prior to printing. No special surface treatment steps were performed on the substrates prior to printing.

2.2.3 Plasma Treatment

Immediately after printing, the as-printed samples were placed inside a plasma chamber (March PX250, March Instruments, California, USA), which was connected to a 13.56 MHz, 300W RF Generator (ENI, ACG-3B, MKS Instruments, Boston, Massachusetts, USA). The plasma system was connected to two gas feed lines: Argon (Ar) for the AgNO₃ reduction step, and nitrogen (N₂) for purging the system before and after plasma treatment. The plasma treatment step was performed in an Ar atmosphere at a pressure of 650 mTorr. After the pressure was stabilized, treatment was initialized by setting the RF power at 150W for samples printed using the

monoEG ink and 300W for samples printed using the diEG and triEG inks. Plasma exposure times ranged from 5 to 30 minutes in order to explore the effect of plasma exposure on material properties. A power of 300W was selected for samples printed using the diEG and triEG inks because previous work with 1.5M inks showed that a power of 150W was insufficient to create structures with measurable electrical conductivity even after 20 minutes of plasma exposure and thus was not investigated in this research (Radwan, Sui et al. 2022, Sui, Hess-Dunning et al. 2022). Conversely, a power of 150W was used for samples printed using monoEG inks because previous work showed that 200W produced structures with maximum conductivity in less than 15 minutes (Sui, Ghosh et al. 2018), which was deemed too short to tune the resistance of printed structures using plasma exposure time as a control parameter. Previous work also showed that for these plasma power conditions, the substrate temperatures range from 35°C for an exposure time of 5 minutes at 150 W to 135°C for an exposure time of 30 minutes at 300W (Sui 2019). Figure A-1 in Appendix 1 shows plots of measured substrate temperature as a function of plasma exposure time for plasma powers of 150W and 300W.

2.2.4 Material Characterization

2.2.4.1 Sheet Resistance Measurements

The sheet resistance of samples printed using each type of ink and the full range of exposure times described above was measured using a 4-point probe (Lucas Lab 302, Gilroy, California, USA). For each of the six exposure times, four-point probe measurements were made on three, $0.5 \times 0.5 \text{ cm}^2$ samples in order to determine an average sheet resistance for each exposure time. A photograph of a representative sample is shown in Figure 2-5. The 4-point probe device consists of four uniformly spaced probes with a probe spacing of 1 mm. A fixed current was supplied through the outer probes and the resulting voltage was measured across the two inner probes. The probes were connected to a source meter instrument (Keithley 2400 Source Measurement Unit) in order to measure the sheet resistance in Ω/\square .

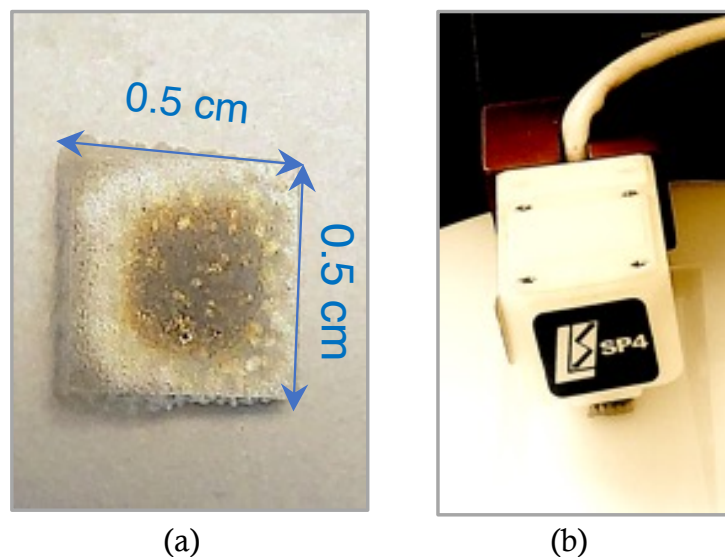


Figure 2-5: Photographs associated with sheet resistance measurements: (a) $0.5 \times 0.5 \text{ cm}^2$ sample for 4-point probe measurements, (b) Lucas Lab 302 SP4: 4-point probe measurement device with a mounting stand used for sheet resistance measurements. (Radwan, Sui et al. 2022). © 2022 IEEE.

Figure 2-6 is a plot of average sheet resistance versus plasma exposure time for samples printed using each type of ink solvent. Average sheet ranged from a high of $\sim 10^5 \Omega/\square$ for the triEG ink to a low of $\sim 10^1 \Omega/\square$ for all three of the inks. For all of the ink formulations, the sheet resistance decreases with increasing plasma exposure time. A plasma exposure time of 5 minutes was sufficient to produce a measurable sheet resistance in samples printed using the monoEG and diEG inks; however, a measurable sheet resistance was not realized for plasma exposure times below 15 minutes for the triEG ink. The most significant decrease in sheet resistance was observed between 5 and 10 minutes for the monoEG and diEG inks (by a factor of $\sim 100X$) and between 15 and 20 minutes for the triEG ink (by a factor of $\sim 10^4$). For an exposure time of 30 minutes, the sheet resistances of all ink types converge to $\sim 10\Omega/\square$. These data indicate that the sheet resistance of the inkjet printed samples is sensitive to two process-related parameters: (1) plasma exposure time and (2) ink solvent. Assuming that a continuous conductive structure is required to measure sheet resistance, Figure 2-6 suggests that the threshold for the formation of a continuous Ag structure occurs at a plasma exposure time of no more than 5 minutes for the monoEG and diEG inks and 15 minutes for the triEG ink. It is likely that the threshold for the monoEG ink is considerably less than 5 minutes given that the sheet resistance was only $10^3 \Omega/\square$ at that time point. The data in Figure 2-6 also indicates that sheet resistance is most sensitive to plasma exposure during the first ~ 5 minutes after continuous formation of Ag structures for the monoEG ink, during the first 15 minutes for the diEG ink and the first 5 minutes for the triEG ink.

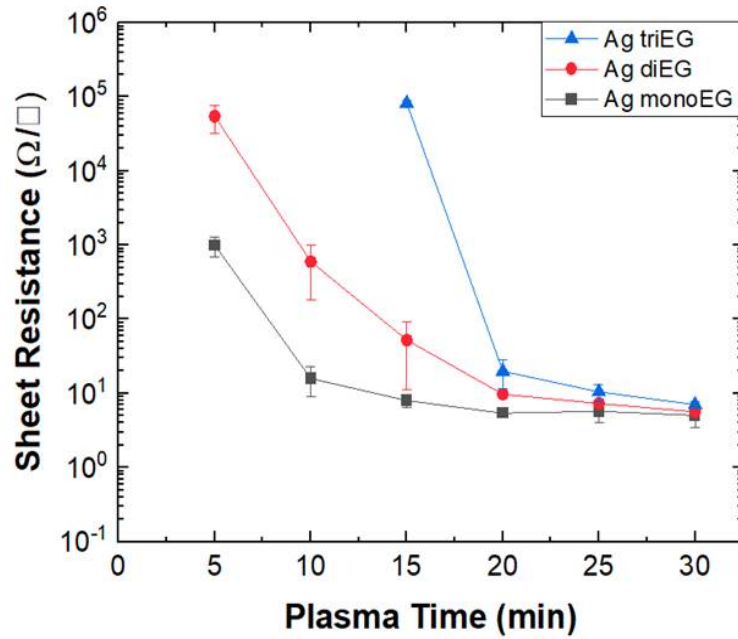


Figure 2-6: Sheet resistance versus plasma exposure time. (Radwan, Sui et al. 2022). © 2022 IEEE

2.2.4.2 Scanning Electron Microscopy

Scanning electron microscopy (SEM) imaging (Thermo Fisher Aprero2) was performed to investigate the relationship between ink composition and microstructure. Figure 2-7 presents plan-view SEM images from samples printed using monoEG, diEG and triEG inks after 30 minutes of plasma exposure. Figure 2-7a shows that the sample using the monoEG ink exhibits the smooth surface texture characteristic of a fully densified structure. In contrast, Figure 2-7b and 7c show qualitatively that the surface roughness increase significantly for the samples printed using the diEG and

triEG inks, with the roughest, most porous morphology observed for the sample printed using the triEG ink. These observations are consistent with AFM measurements made on these samples which showed that the average surface roughness was 52.6 nm, 56.6 nm and 62.6 nm for samples printed using monoEG, diEG and triEG inks, respectively.

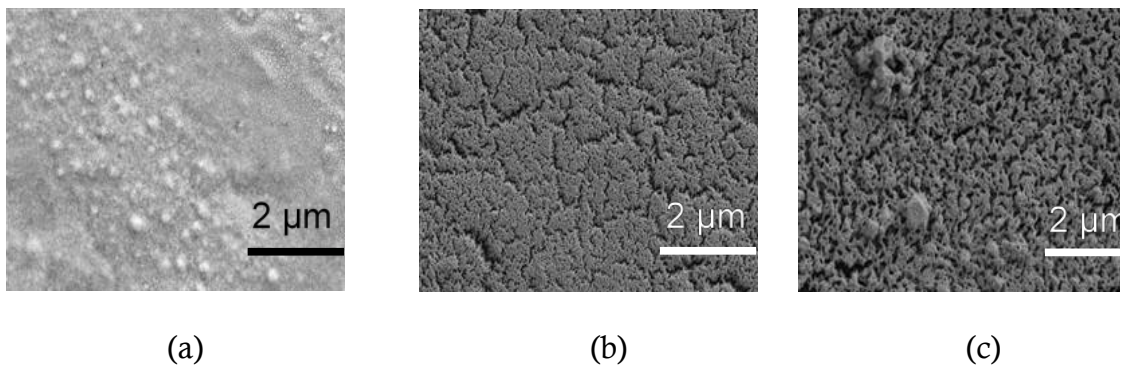


Figure 2-7: Plan-view SEM images of strain gauge samples printed using the monoEG, diEG and triEG inks after 30 min plasma treatment (a) monoEG, (b) diEG and (c) triEG. (Radwan, Sui et al. 2022). © 2022 IEEE.

2.3 Strain Gauge Development

2.3.1 Testing Setup

The electromechanical properties of strain gauges using each ink type and the full range of plasma exposure times were measured using the custom-built, stepper motor driven tensile tester shown in Figure 2-8. LabView-based control software enables this system to perform both single-cycle and cyclic testing under tightly controlled conditions in an automated manner. For samples that exhibit a measurable electrical resistance, this system is capable of measuring electrical resistance as a function of applied strain. In such cases, electrical resistance is calculated from I-V

measurements made at a particular applied strain. These I-V measurements are made using a precision current meter (Keithley 6485) and a voltage source (Keysight E3631A). Both instruments are controlled and I-V data collected by a customized LabView I-V program.

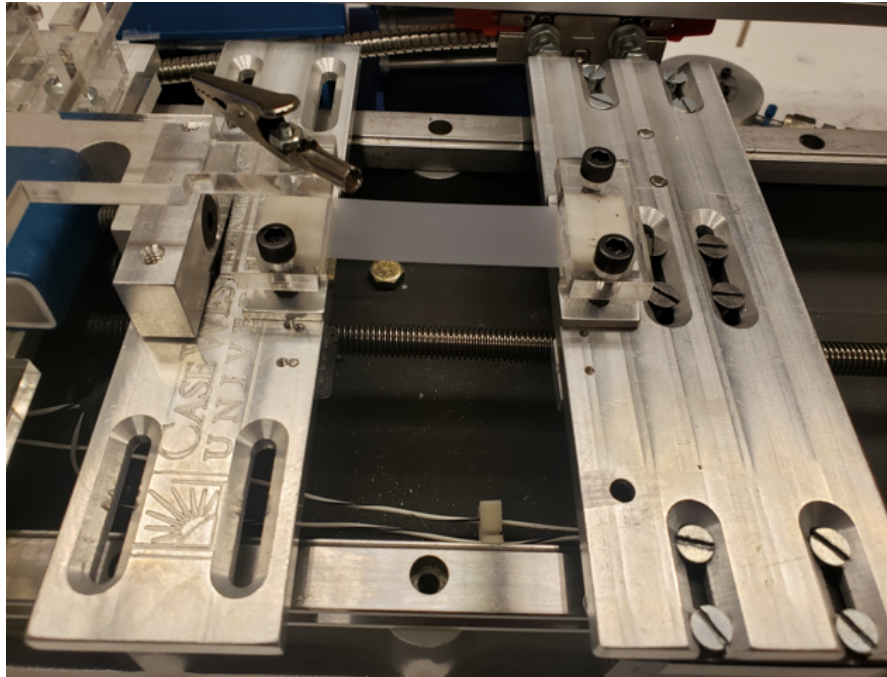


Figure 2-8: Photograph of the custom tensile tester. (Radwan, Sui et al. 2022). © 2022 IEEE

Prior to characterizing the inkjet printed strain gauges, single-cycle stress-strain measurements were performed on a cellophane tape substrate in order to determine its elastic properties in order to ascertain the appropriate strain range for strain gauge testing. Stress strain curves, such as the plot shown in Figure 2-9, were generated from cellophane test specimens with dimensions of $8 \times 1.9 \text{ cm}^2$. By analyzing the linear region of the stress strain curves, which corresponds to strains between 0% and 1%,

the Young's modulus was calculated to be 3.86 GPa which is consistent with data published elsewhere (Paunonen 2013). More importantly, Figure 2-9 also shows that the onset of non-linear elastic behavior occurs at $\sim 1.25\%$ strain which corresponds to a stress of ~ 52 MPa. It was determined from these data that the applied strain used to evaluate the printed strain gauges would not exceed 1%.

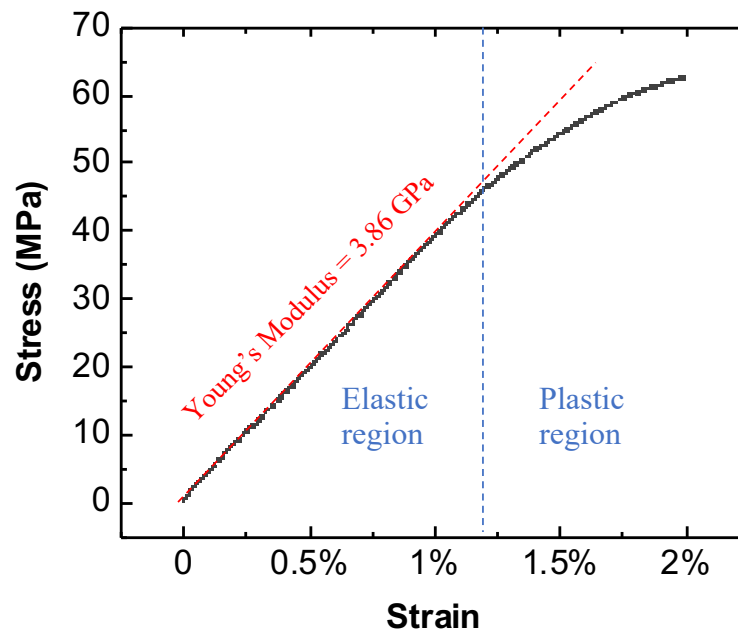


Figure 2-9: Stress-strain curve of a 70-mm long cellophane tape sample. (Radwan, Sui et al. 2022). © 2022 IEEE

2.3.2 Strain Gauge Fabrication

Figure 2-10 presents photographs of a typical Ag strain gauge developed in this dissertation. Each device consisted of a 7-turn serpentine resistor with a nominal line width of $200\ \mu\text{m}$ and a nominal thickness of $5\ \mu\text{m}$. Each end of the device was terminated with a $800\ \mu\text{m} \times 800\ \mu\text{m}$ contact pad. The overall areal dimensions of each device was $2.8\ \text{mm} \times 4.4\ \text{mm}$.

Strain gauges were printed using the monoEG, diEG and triEG inks developed for the sheet resistance measurements. The sheet resistance measurements presented in Figure 2-6 above were used to determine the plasma exposure time for each strain gauge device. For the devices printed using the monoEG ink, seven distinct plasma exposure times ranging from 5 to 30 minutes were selected for study. For the devices printed using the diEG and triEG inks, four distinct plasma exposure times ranging from 15 to 30 minutes were selected. A total of 3 to 5 devices were fabricated for each plasma exposure time.

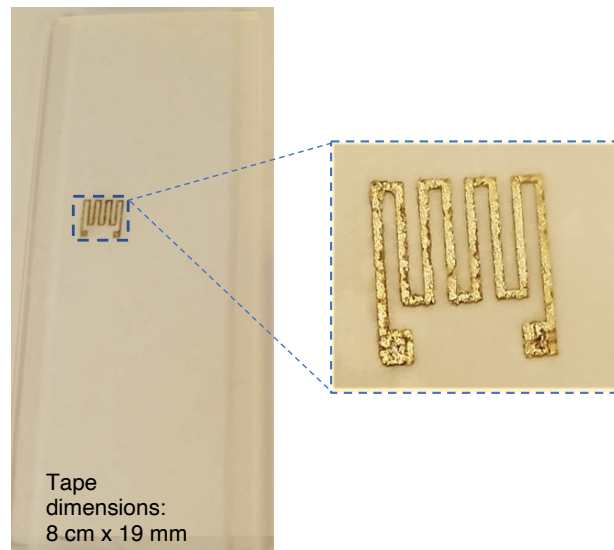


Figure 2-10: Photographs of a strain gauge sample printed on a 8cm x 19mm strip of cellophane tape. The inset figure is a close-up view of the strain gauge (Radwan, Sui et al. 2022). © 2022 IEEE

2.3.3 Strain Gauge Testing

2.3.3.1 *Single-cycle Resistance-Strain Measurements*

Single-cycle resistance-strain measurements were made on each inkjet printed strain gauge sample. Each sample was mounted into the test fixture and an initial resistance (R_0) measurement was made in the unstrained position. At a rate of 20 $\mu\text{m/s}$,

each sample was then elongated to 200 μm , at which a resistance measurement was made. This process was repeated for elongations of 400 μm , 600 μm and 800 μm , corresponding to applied strains of 0%, 0.25%, 0.5%, 0.75% and 1%.

Figures 2-11, 2-12 and 2-13 present measured resistance versus displacement for the strain gauges printed using the monoEG, diEG and triEG inks respectively. Each data point in these plots represents the average resistance at each displacement value, with the error bars representing the distribution of the measured resistance

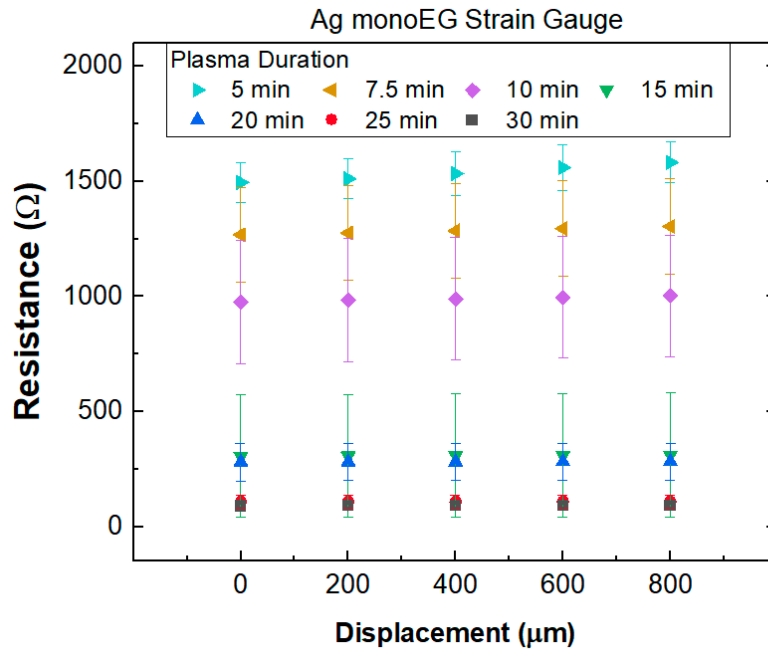


Figure 2-11: Resistance versus displacement for the strain gauges printed using the monoEG ink for the plasma exposure times listed in the inset.

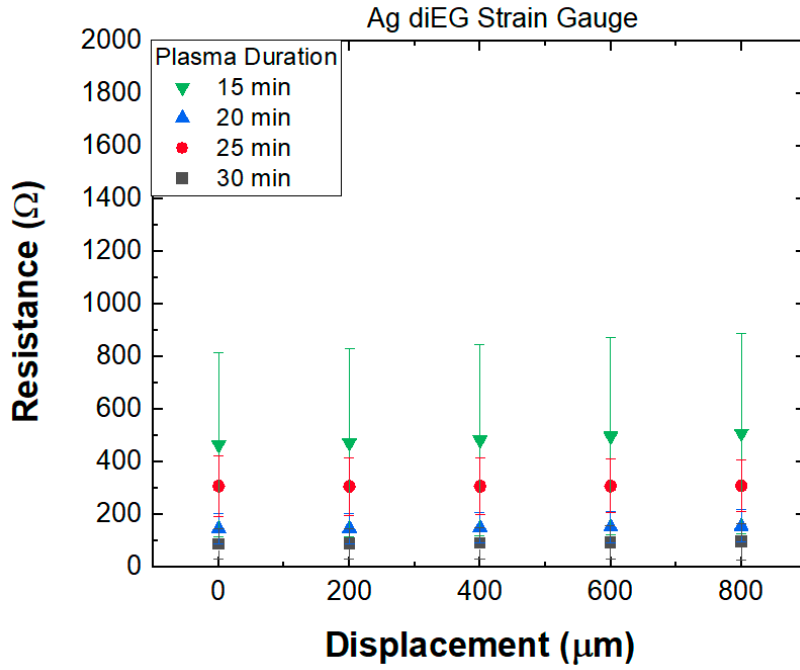


Figure 2-12: Resistance versus displacement for the strain gauges printed using the diEG ink for the plasma exposure times listed in the inset.

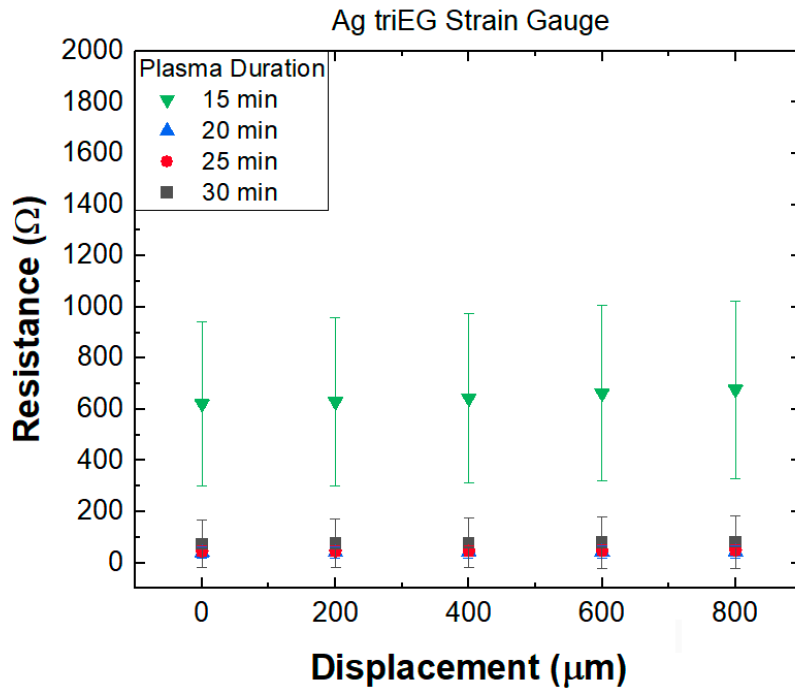


Figure 2-13: Resistance versus displacement for the strain gauges printed using the triEG ink for the plasma exposure times listed in the inset.

values. Without exception, the resistance exhibits a linear relationship with displacement. For strain gauges prepared using the diEG and triEG inks, the spread in measured resistance values is largest for the shortest plasma exposure times, which correspond to the highest resistance values. This is not surprising since the shortest plasma exposure times used in this experiment correspond to plasma exposure times near the threshold for the formation of continuous Ag structures. Consequently, it is expected that the spread in measured resistance values would be highest for these plasma exposure times.

2.3.3.2 Cyclic Resistance-Strain Measurements

Cyclic resistance-strain measurements were made on a strain gauge printed using each of the ethylene glycol-based inks. In order to provide a reliable comparison with respect to each ink solvent, a plasma exposure time of 30 minutes was used for each strain gauge. As with the single cycle tests, each sample was mounted into the test fixture and an initial resistance (R_0) measurement was made in the unstrained position. At a rate of 10 $\mu\text{m/s}$, each sample was then elongated to 200 μm , corresponding to a strain of 0.25%, at which a resistance measurement was made. The displacement was then returned to the unstrained position and the measurement was repeated for a total of 1000 cycles. Each cycle took about 2 minutes to complete. At each half a cycle, the stepper motor was paused for 30 seconds to measure the resistance at strains of 0% and 0.25%.

Figure 2-14 presents plots of resistance versus cycle number for the test samples printed using each of the ink types. For each cycle, the plots show the measured

resistance at both 0% and 0.25% strain. To varying degrees, all three samples exhibit an increase in measured resistance with increasing cycle number. After 1000 cycles, the sample printed using the monoEG ink exhibited an overall increase in resistance of 3.89 Ω at 0% and 3.60 Ω at 0.25% strain. The samples printed using the diEG ink showed an increase in resistance of 2.63 Ω at 0% strain and 2.15 Ω at 0.25% strain after 1000 cycles. The sample printed using the triEG ink exhibited the largest change in resistance after cyclic testing of 4.09 Ω at 0% strain and 1.36 Ω at 0.25% strain.

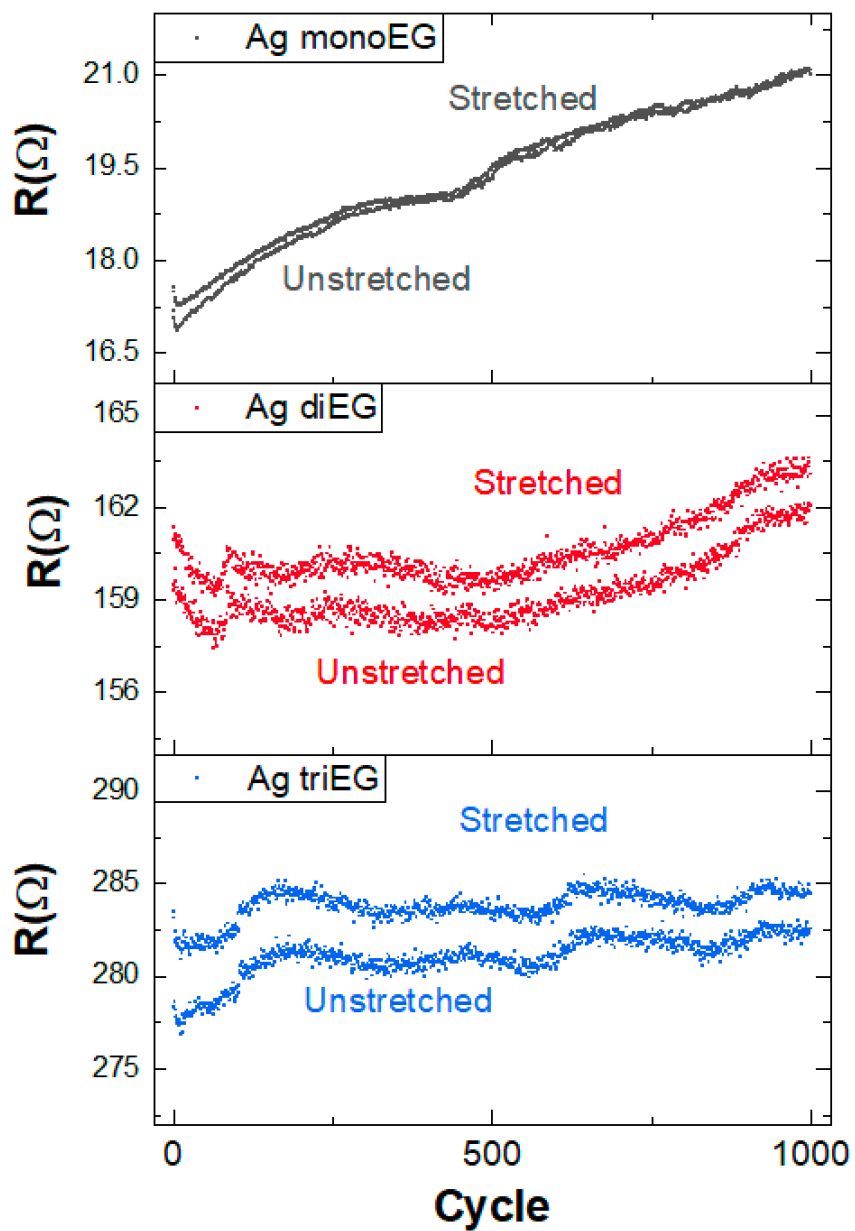


Figure 2-14: Measured resistance versus cycle number for strain gauges printed using mono-, di- and tri-EG inks for a maximum strain of 0.25%. The plasma treatment for each sample was 30 minutes.

SEM imaging was used to examine each of the strain gauges after cyclic load testing for evidence of mechanically induced damage. Figure 2-15 presents plan-view SEM images of the test samples after cyclic load testing. The approximate imaging area for each sample was $80 \times 80 \mu\text{m}^2$. Figure 2-15(a), taken from the sample printed using the monoEG ink, shows no evidence of mechanically induced damage. Likewise, Figure 2-15(b) shows that the sample printed using the diEG ink suffered no discernable damage. However, Figure 2-15(c) shows extensive microcrack formation in the sample printed using the triEG ink. The larger crack lengths appear to be on the order of 10 to 20 μm , which, in high enough density, could be sufficient to cause a measurable increase in the resistance of the test structure.

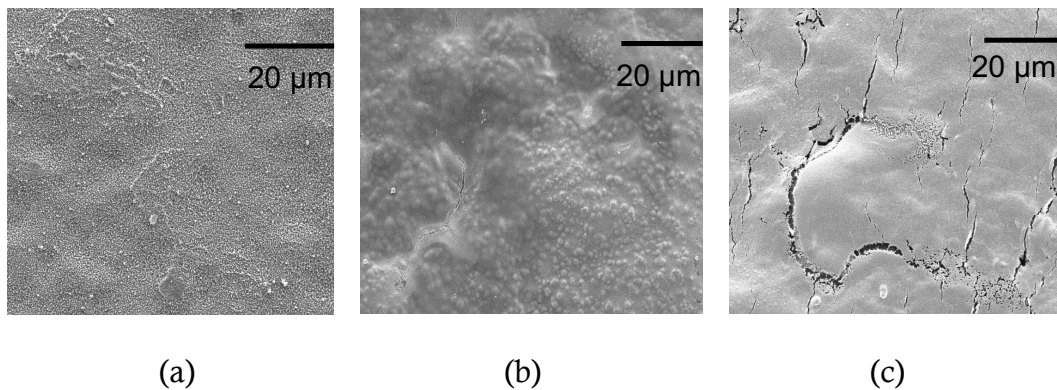


Figure 2-15: Plan-view SEM images of strain gauges printed using the monoEG, diEG and triEG inks after cyclic load testing for 1000 cycles: (a) monoEG (b) diEG and (c) triEG. (Radwan, Sui et al. 2022). © 2022 IEEE

2.3.3.3 Static Resistance Measurements

Static resistance measurements were performed over a 60-day period under ambient conditions by performing simple two-point resistance measurements once per day throughout the testing period. To ensure consistency in the measurements, wire leads were mounted to each end of the test samples using Ag epoxy. The thickness of

the epoxy relative to that of the test specimen minimized the influence of any environmentally induced changes in the epoxy on the measurements. Figure 2-16 presents a plot of measured resistance versus time for each of the test samples. For the samples printed using the monoEG and triEG inks, the resistance increased by 83% and 367%, respectively while that for the diEG sample increased by only 5%.

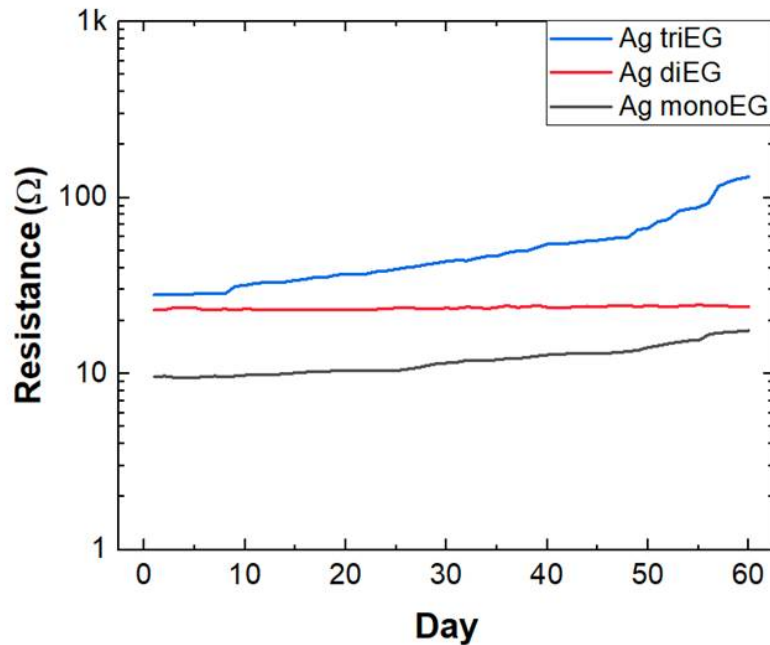


Figure 2-16: Measured resistance versus time under ambient conditions for samples printed using monoEG, diEG and triEG inks and plasma treated for 30 minutes. (Radwan, Sui et al. 2022). © 2022 IEEE

2.3.4 Analysis and Discussion

2.3.4.1 Material Characterization

The sheet resistance results presented in Figure 2-6 strongly mirror the relationships between sheet resistance and plasma exposure time for Ag/monoEG, Ag/diEG and Ag/triEG inks with 3 times the AgNO_3 concentration (1.5M) reported

previously, with the only significant difference being the distinctly lower sheet resistance values associated with the high concentration inks (Sui, Hess-Dunning et al. 2022). In that study, the sheet resistance ranged between $10^1 \Omega/\square$ and $10^0 \Omega/\square$, whereas in this study the sheet resistance ranged between $10^5 \Omega/\square$ and $10^1 \Omega/\square$. These data indicate that a three-fold reduction in AgNO_3 concentration significantly enhances the range over which sheet resistances are tunable by three orders of magnitude, in essence answering the question posed in the introduction and illustrated in Figure 2-3. The SEM observations presented in Figure 2-7 are also consistent with those reported by (Sui, Hess-Dunning et al. 2022) which showed that surface roughness and porosity of plasma-treated structures increases with decreasing solvent vapor pressure.

2.3.4.2 Strain Gauge Characterization

The principal parameter used to characterize the performance of a strain gauge is known as the Gauge Factor (GF); a parameter that can be calculated using the following formula provided that the behavior is linear:

$$GF = \frac{\Delta R / R_o}{\Delta L / L_o} = \frac{\Delta R / R_o}{\varepsilon} \quad (4)$$

where ΔL is the change in displacement, R_o is the resistance at zero displacement (sample is unstrained), ΔR is the resistance change and $\varepsilon = \Delta L / L_o$ is the mechanical strain.

Figures 2-17, 2-18 and 2-19 are plots that show the average relative change in resistance versus strain for samples made from each ink type included in this study. Each plot represents a particular ink type and presents relative change in resistance versus strain data for samples subjected to plasma treatment for a particular exposure time. The three graphs show a linear relationship between the relative change in resistance versus strain for all ink types and exposure times. For each ink type, the steepest slopes were observed for samples subjected to the shortest exposure times.

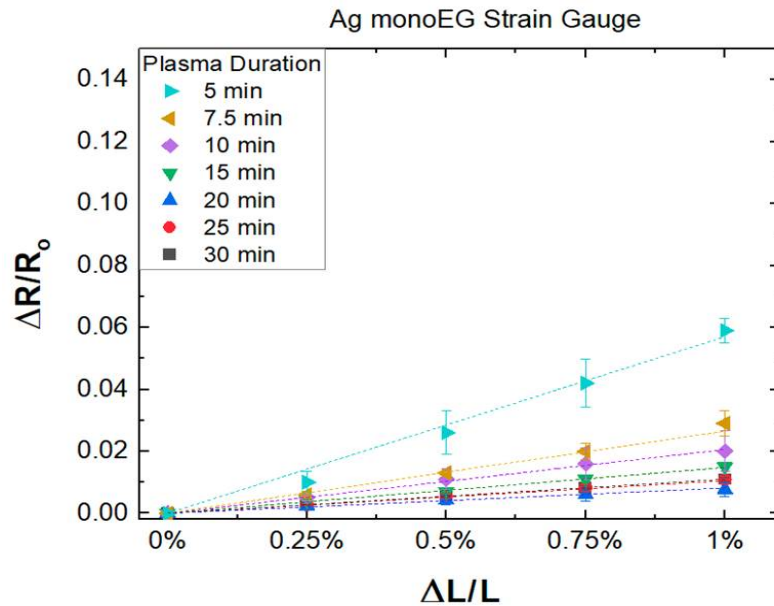


Figure 2-17: Relative change in resistance versus relative change in length for strain gauge samples printed using the monoEG ink and plasma treated for the exposure times listed in the inset. (Radwan, Sui et al. 2022). © 2022 IEEE

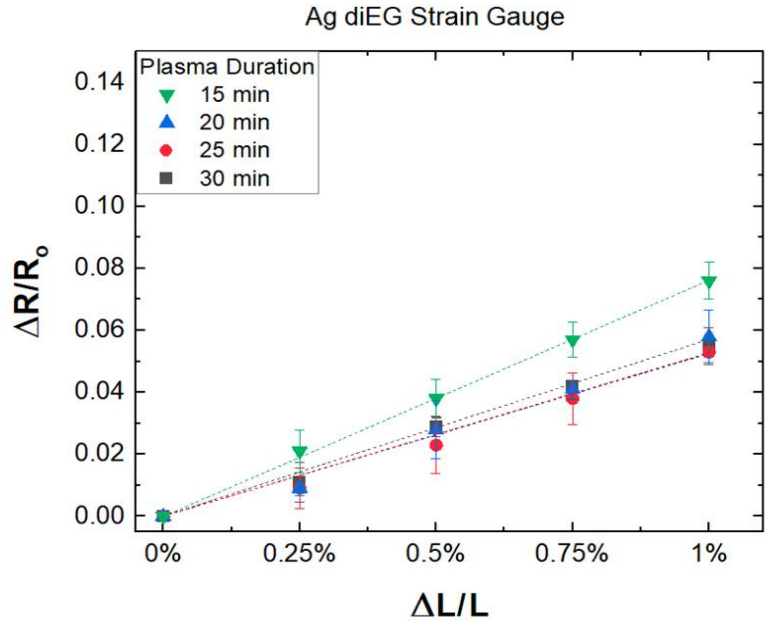


Figure 2-18: Relative change in resistance versus relative change in length for strain gauge samples printed using the diEG ink and plasma treated for the exposure times listed in the inset. (Radwan, Sui et al. 2022). © 2022 IEEE

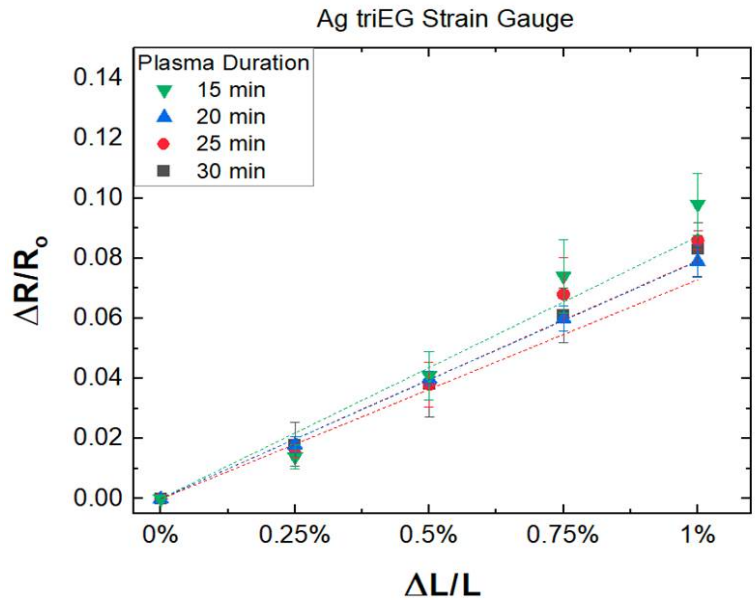


Figure 2-19: Relative change in resistance versus relative change in length for strain gauge samples printed using the triEG ink and plasma treated for the exposure times listed in the inset. (Radwan, Sui et al. 2022). © 2022 IEEE

Figure 2-20 shows the average GFs as a function of plasma exposure time for samples printed from each type of ink as determined from plots shown in Figures 2-13, 2-14, and 2-15 and computing an average GF for each exposure time. For each ink type, the average GF is highest for the shortest plasma exposure time and decreases significantly with increasing exposure time. For structures printed using the monoEG ink, the highest average GF is ~ 6 for an exposure time of 5 minutes but steadily decreases to ~ 1 for exposure times greater than 20 minutes. In contrast, for the diEG ink, the highest average GF is ~ 7.5 for a plasma exposure time of 15 minutes and decreases to only ~ 6 for an exposure time of 30 minutes. For the triEG ink, the highest average GF is ~ 10.5 for an exposure time of 15 minutes, decreasing to ~ 8.5 for an exposure time of 30 minutes. (Radwan, Sui et al. 2022).

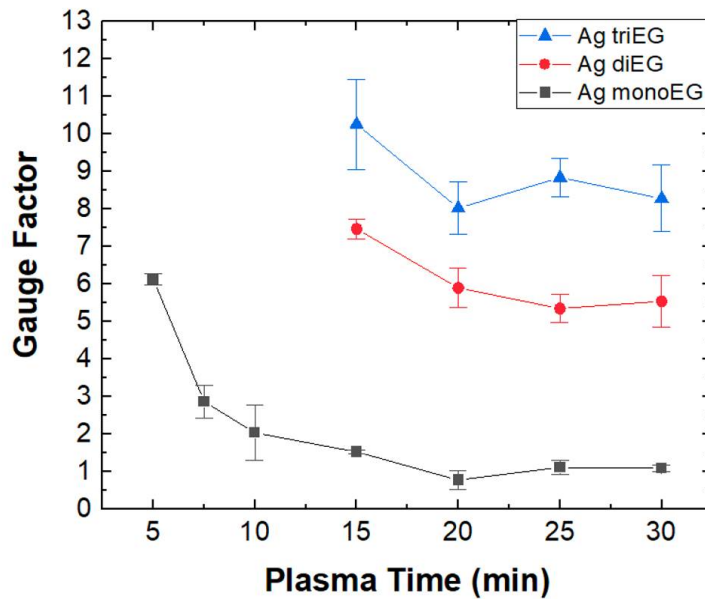


Figure 2-20: Gauge factor versus plasma exposure time for strain gauges printed using monoEG, diEG and triEG inks. (Radwan, Sui et al. 2022). © 2022 IEEE

For all Ag ink types, the decrease in GF with increasing plasma exposure time is likely attributed to Ag nucleation and growth during the formation of continuous Ag structures under plasma exposure. A relatively thin Ag film is created on top of the AgNO₃ when the sample is exposed to plasma for a short time, (5 to 15 min depending on solvent type), which creates a reflection boundary (Herrmann, Müller et al. 2007). This boundary increases electron scattering which in turn increases the total resistivity of the Ag film. As plasma exposure time increases, Ag nucleation continues and therefore the Ag film thickness increases, which minimizes electron scattering and hence the total resistivity decreases. Typically, metal foil strain gauges have GFs of ~2 (Maiwald, Werner et al. 2010). The high GFs observed in our devices are likely due to the unique microstructure of the plasma-converted silver. In previous work using AgNO₃/EG inks as well as the findings reported herein, structures printed using EG as the solvent exhibit a much higher porosity and surface area after plasma treatment than sputter-deposited Ag films, with the porosity increasing with decreasing solvent vapor pressure (Sui, Hess-Dunning et al. 2022). (Radwan, Sui et al. 2022).

From a material property perspective, the GF can be defined as:

$$GF = 1 + 2\nu + \frac{\Delta\rho/\rho}{\varepsilon} \quad (5)$$

where ν is the Poisson's ratio of the material, ρ is resistivity, and ε is strain (Beckwith and Roy 1982, Hannah and Reed 1992). The factor $(1 + 2\nu)$ is due to the change of conductor geometry under strain, and the factor $(\Delta\rho/\rho)/\varepsilon$ stands for the contribution of piezo-resistivity. For bulk silver, the Poisson's ratio is ~ 0.37 (Rahman, Moser et al. 2018). Assuming a GF of 2, the contribution of piezo-resistivity to the GF is ~18%. For porous silver, the Poisson's ratio can be as high as 0.8 (Rahman, Moser et al.

2018). Under uniaxial strain, the pores in the porous silver will contract in the lateral directions, resulting in higher contraction of the entire structure in lateral direction compared to that of a bulk counterpart under the same condition. The relationship between piezo-resistivity and porosity is likely dependent on the type of material (semiconductor vs. polymer vs. metal) and microstructure (dense vs. porous). For example, in silicon, the piezo-resistivity is higher for porous silicon than for bulk silicon (Toriyama and Sugiyama 2003, Pramanik and Saha 2006). However, a study on polydimethylsiloxane/carbon nanotube (PDMS/CNT) nano-composites showed an opposite trend (Michel, Capasso et al. 2020). For Au, an experimentally verified model showed the higher piezo-resistivity in porous gold relative to bulk gold is due to tunnel resistance (Herrmann, Müller et al. 2007). To the best of our knowledge, the piezo-resistivity of porous silver has not been systematically studied; however, the contribution of piezo-resistivity to the GF in strain gauges made from silver nanoparticle inks varied from 28% to 39% (Rausch, Salun et al. 2011, Lee, Lee et al. 2014); which, in all cases, is higher than that for fully dense Ag foil-based strain gauges. In this work, the highest GFs associated with each ink type can perhaps be explained by porosity in the plasma-treated structures, which would be most pronounced in samples subjected to relatively short plasma exposure times regardless of ink solvent. The GF data also suggests that porosity is a main contributor to GF in structures printed using AgNO_3/EG inks because as a group the highest gauge factors were observed in structures printed using triEG as the solvent, which has the lowest vapor pressure and was previously shown to produce structures with highest porosity after plasma treatment (Sui, Hess-Dunning et al. 2022). That the GFs associated with the

diEG ink is lower than the triEG ink and those associated with the monoEG ink lower still can also be understood with respect to porosity since as shown by (Sui, Hess-Dunning et al. 2022), porosity decreases with increasing solvent vapor pressure. (Radwan, Sui et al. 2022).

2.3.4.3 Cyclic Testing

Figure 2-21 presents plots of relative change in resistance versus cycle number for the test samples printed using each of the ink types. The sample printed using the monoEG ink exhibited a moderate degree of stability, with the average relative change in resistance decreasing by about 15% over 1000 cycles. The sample printed using the diEG ink exhibited a much higher degree of stability, with the average relative change in resistance varying by only 1% over the same range. In contrast, the sample printed using the triEG ink was unstable during cyclic loading, with the average relative change in resistance decreasing by ~36%. (Radwan, Sui et al. 2022).

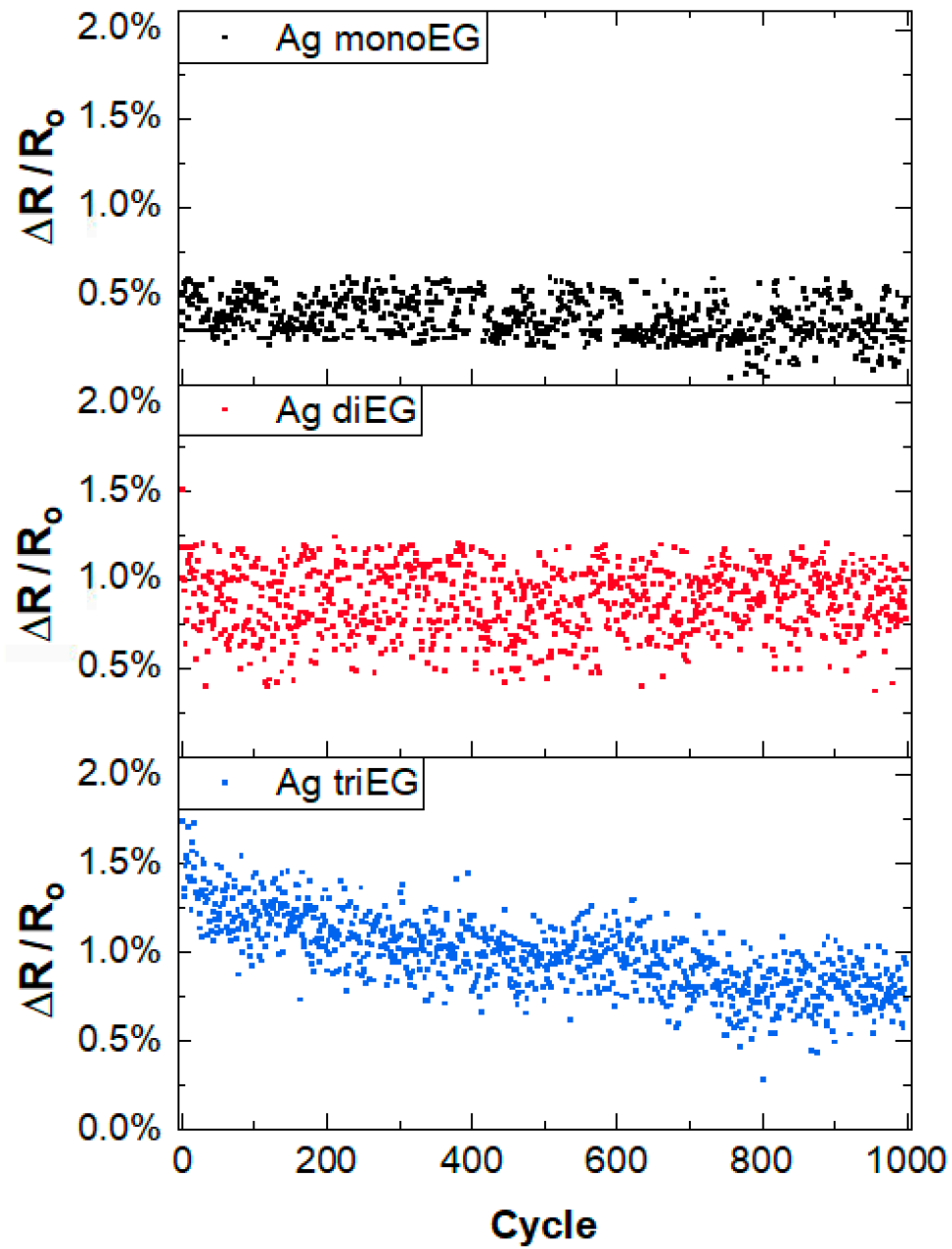


Figure 2-21: Normalized change in resistance versus cycle number for strain gauges printed using mono-, di- and tri-EG inks for a maximum strain of 0.25%. The plasma treatment for each sample was 30 minutes. (Radwan, Sui et al. 2022). © 2022 IEEE

The results of the cyclic mechanical tests and the static resistance measurements can be understood with respect to the microstructure of the test specimens. The SEM images in Figure 2-7 as well as the results presented in (Sui, Hess-Dunning et al. 2022) indicate that roughness and porosity are highest in structures printed using triEG inks. Under mechanical loading, defects can serve as initiation sites for microcrack formation, and under static ambient conditions the added surface area associated with surface defects enhances the effects of reactions with adsorbed atmospheric contaminants such as oxygen and sulfur. Both of these conditions could result in a measurable increase in resistance. It is expected that these two effects would be most pronounced in printed structures with the highest density of surface defects, which occurs in films printed using triEG-based inks, with microcrack formation likely being the largest contributor. Regarding the samples printed using monoEG ink, the relatively smooth surface morphology likely inhibits crack formation under mechanical loading. As shown in (Sui, Hess-Dunning et al. 2022), films printed using monoEG are about a factor of 2 and 1.25 thinner than those printed using triEG and diEG, respectively, therefore the observed increase in resistance could be associated with loss of conductive Ag due to surface oxidation on top surface and sidewalls of the printed structures, effectively reducing the cross sectional area of Ag conductor. As for the samples printed using the diEG ink, low surface defect density suppresses microcrack formation and its higher thickness diminishes the effects of surface oxidation relative to the monoEG sample, rendering the structures relatively stable with respect to measured resistance. (Radwan, Sui et al. 2022).

2.4 Temperature Sensors

The sheet resistance results presented in Section 2.2.4.1 show that the sheet resistance of the printed Ag structures is a function of plasma exposure time regardless of the ink solvent. Moreover, for each ink type, the sheet resistance decreased in an exponential fashion with increasing plasma exposure time. These data indicate that the sheet resistance of the printed structures is sensitive to two convenient and easy to control process parameters. The work presented in Section 2.3 shows that the gauge factor is also sensitive to both ink type and plasma exposure time thus motivating an investigation as to whether the temperature coefficient of resistance (TCR) in printed temperature sensors is also sensitive to the same process parameters.

2.4.1 Sensor Fabrication

Temperature sensors were fabricated from the three ethylene glycol-based inks using the procedure detailed in Section 2.2.1. The sensors consisted of the serpentine resistor geometry shown in Figure 2-22a. The total length of the 3-turn serpentine sensor was 51 mm and its width was 1 mm. Figure 2-22b presents a photograph of a representative sensor after printing and plasma treatment. To facilitate easy handling, the sensors, which were printed on cellophane tape (SCOTCH Matte-Finish $\frac{3}{4}$ " x 600", 3M, Maplewood, Minnesota, USA), were adhered to photo paper (EPSON, Japan).

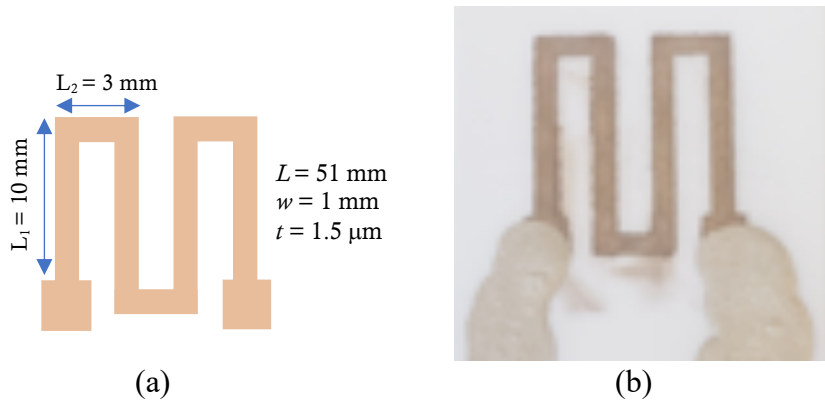


Figure 2-22: (a) Schematic of the serpentine shaped Ag EG temperature sensor. (b) Plan-view photograph of a printed temperature sensor. Silver epoxy was applied to each pad to facilitate connection to the power source.

2.4.2 Testing Setup

Temperature sensors were evaluated using the custom-built testing rig shown in Figure 2-23. The rig consisted of a transparent acrylic enclosure with penetrations for electrical connections to a strip heater and the sensor. The strip heater was placed directly on top of the sensor. In order to maximize transfer of heat by conduction to the sensor, the bottom of the sensor was affixed to a glass slide to minimize heat loss. To minimize convective heat loss, the testing enclosure was also filled with cotton balls. This provided thermal isolation while still allowing probe tips to make electrical contact to the sensor. The resistance of the sensor was monitored using a handheld multimeter (Fluke 79 III). A flexible polyimide heater strip (IC Station 12W, 12V Flexible Polyimide Heater) was used to heat the temperature sensors under test. The polyimide heater was powered using an Agilent E3630A DC power supply.

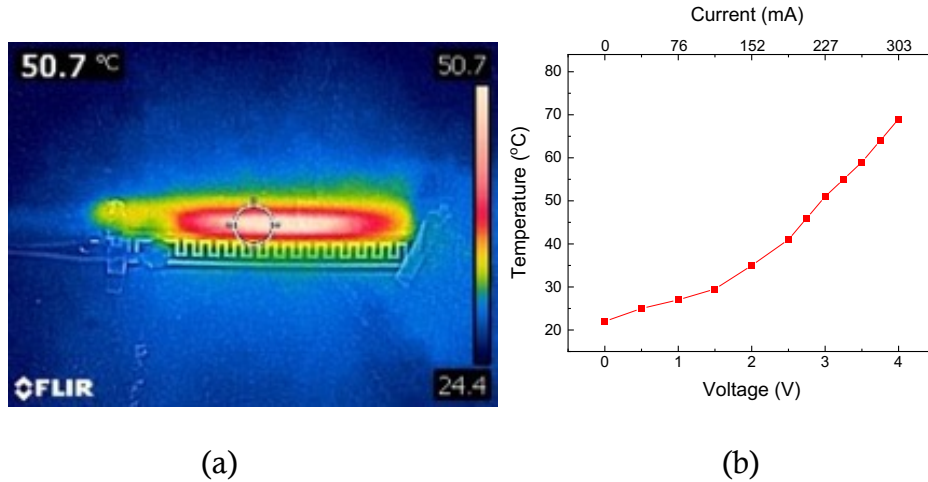


Figure 2-24: (a) Infrared camera view of the strip heater under power supplied by the DC power supply, (b) Temperature vs applied voltage and current for the strip heater as measured using the infrared camera.

2.4.3 Temperature Sensor Testing

A plot of measured resistance versus temperature for temperature sensors fabricated from the monoEG ink for a series of plasma treatment times ranging from 4 to 22 minutes is shown in Figure 2-25. The nominal resistance decreases from 1576Ω to 75Ω as the plasma sintering exposure time increases over this range. Moreover, the resistance exhibits a linear behavior with temperature between 22 and 59°C . Figures 2-26 and 2-27 present plots of measured resistance versus temperature for temperature sensors printed using the diEG and triEG inks, respectively, after plasma treatment. Like the sensors fabricated using the monoEG ink, the sensors printed using the diEG and triEG inks exhibit a significant decrease in nominal resistance with increasing plasma exposure time and a linear behavior between measured resistance and testing temperature.

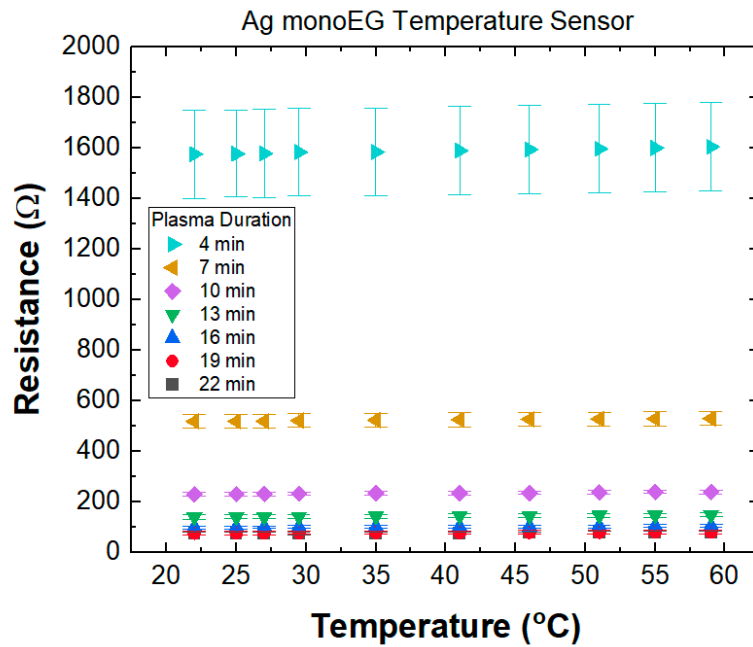


Figure 2-25: Resistance versus temperature for a temperature sensor printed using the Ag monoEG ink and plasma treated for 4, 7, 10, 13, 16, 19 and 22 minutes.

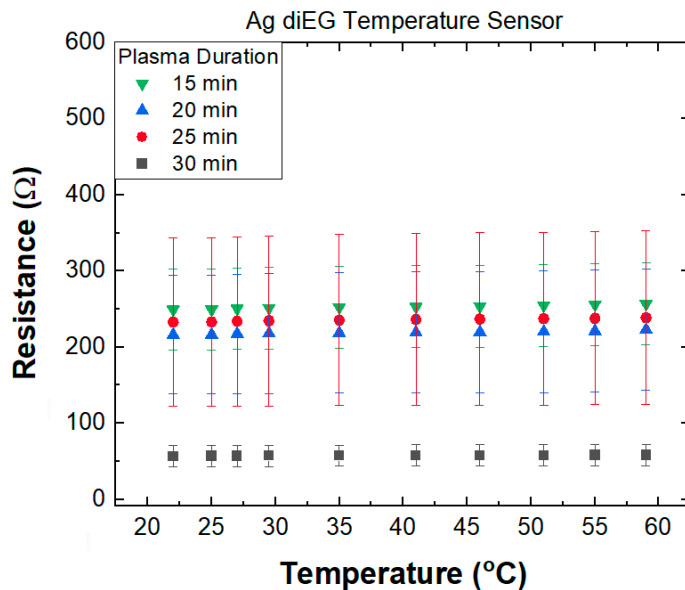


Figure 2-26: Resistance versus temperature for a temperature sensor printed using the Ag diEG ink and plasma treated for 15, 20, 25 and 30 minutes.

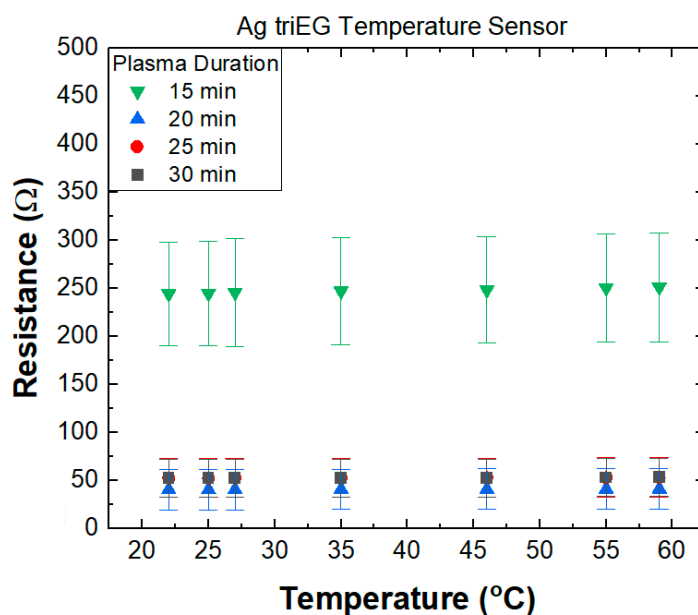


Figure 2-27: Resistance versus temperature for a temperature sensor printed using the Ag triEG ink and plasma treated for 15, 20, 25 and 30 minutes.

2.4.4 Analysis and Discussion

2.4.4.1 TCR Calculations and Comparisons

Plots of resistance versus temperature of the type presented in Figures 2-25, 2-26 and 2-27 do not clearly represent the temperature sensitivity of the printed sensors. To accurately reflect the temperature sensitivity of the sensors, plots of normalized change in resistance versus temperature were created using the data presented in Figures 2-25, 2-26 and 2-27. Figure 2-28 presents the normalized change in resistance versus temperature for sensors printed using the monoEG ink. For all plasma treatment times, the normalized change in resistance exhibits a strong linear relationship with temperature. Moreover, the slope increases as the plasma exposure

time increases from 4 min to 13 min, whereas the slopes for plasma exposure times above 16 min are essentially indistinguishable.

Figures 2-28 and 2-29 present the normalized change in resistance versus temperature for sensors printed using the di- and triEG inks, respectively. Like that for the monoEG ink, plots of the normalized change in resistance versus temperature for both ink types and all plasma treatment conditions exhibit a strong linear dependence with temperature. Unlike the monoEG ink, the spread in the slopes for the devices printed using the diEG and triEG inks is significantly smaller than that for the devices printed using the monoEG inks.

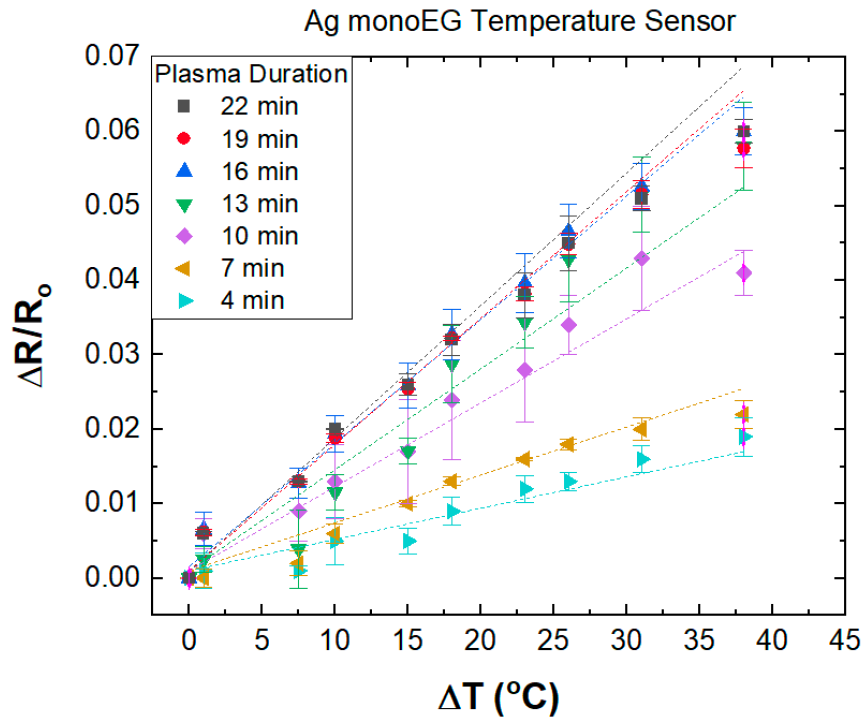


Figure 2-28: Normalized change in resistance versus temperature for temperature sensors fabricated using the monoEG ink. The plasma treatment times are listed in the inset.

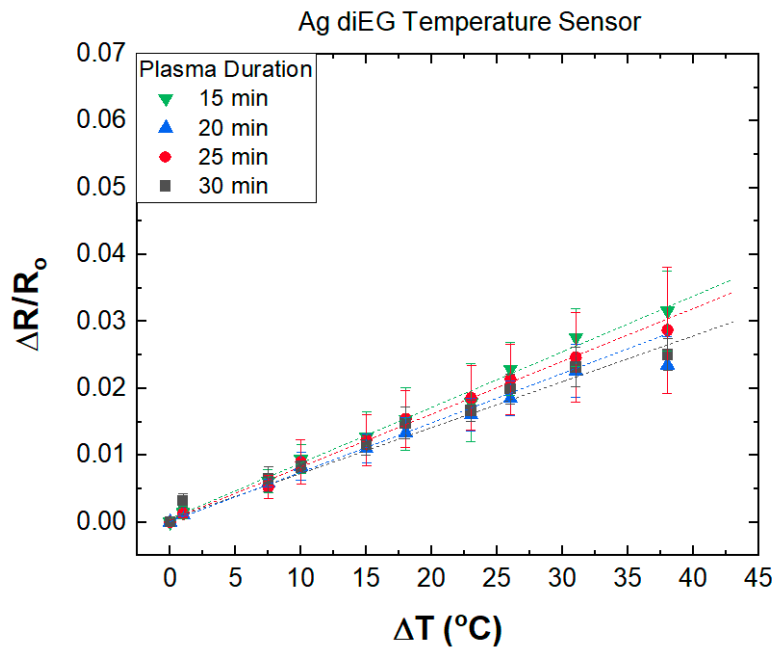


Figure 2-29: Normalized change in resistance versus temperature for temperature sensors fabricated using the diEG ink. The plasma treatment times are listed in the inset.

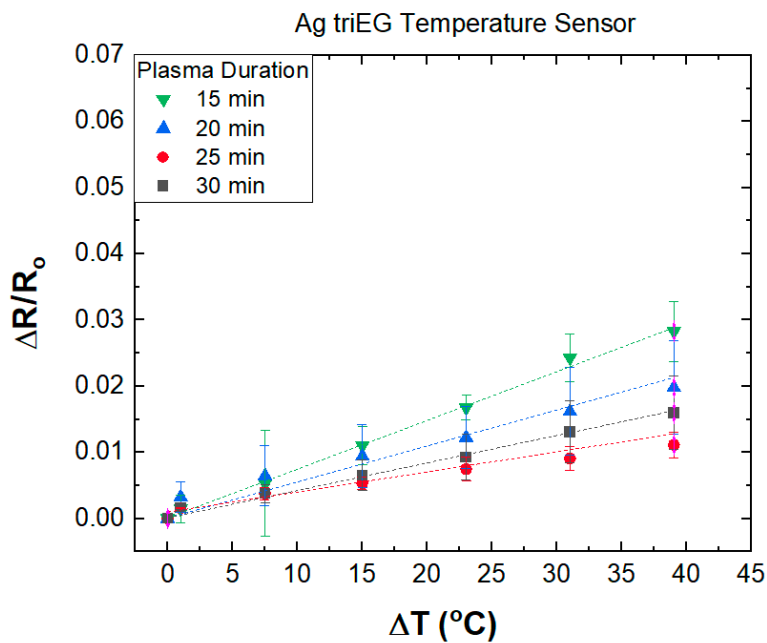


Figure 2-30: Normalized change in resistance versus temperature for temperature sensors fabricated using the triEG ink. The plasma treatment times are listed in the inset.

The slope of each line in Figures 2-28, 2-29 and 2-30 represents the TCR for each associated temperature sensor. Figure 2-31 plots the TCR versus plasma exposure time for temperature sensors printed using the mono-, di- and triEG inks. Each data point represents the mean TCR value computed from 3 test specimens and the error bars represent the spread of the three TCR values associated with the average.

As shown in Figure 2-31, for the sensors printed using the monoEG ink, the TCR steadily increases with plasma exposure time from $5.32 \times 10^{-4} \text{ }^\circ\text{C}^{-1}$ at 4 minutes to nearly $1.7 \times 10^{-3} \text{ }^\circ\text{C}^{-1}$ at 13 minutes, then maintains a relatively constant value of about $1.5 \times 10^{-3} \text{ }^\circ\text{C}^{-1}$ for plasma exposure times of 15 and 22 minutes. In contrast, the TCR values for sensors printed using the diEG and triEG inks were considerably lower, at around $7.23 \times 10^{-4} \text{ }^\circ\text{C}^{-1}$ for sensors fabricated using the diEG ink and $4.88 \times 10^{-4} \text{ }^\circ\text{C}^{-1}$ for sensors fabricated using the triEG ink. Moreover, the TCR values for sensors fabricated using the di- and triEG inks were relatively insensitive to plasma exposure time over the range evaluated in this study. It should be noted that for di- and triEG inks, plasma exposure times less than 15 minutes yielded structures with sheet resistances that were too high to measure, presumably because continuous Ag structures were not fully formed under these conditions. The highest average TCR value ($\sim 1.7 \times 10^{-3} \text{ }^\circ\text{C}^{-1}$) was realized for temperature sensors printed using the monoEG ink and subjected to a plasma exposure time of 13 min.

The results in Figure 2-31 can be understood with respect to both the microstructure and sheet resistance of the printed Ag structures. The SEM images in Figure 2-7 show that structures printed using the triEG ink exhibited the highest degree of porosity after plasma treatment while structures printed using the monoEG ink had

the lowest porosity. Comparing this information with the TCR data in Figure 2-31 suggests a strong connection between microstructure and TCR. The highest TCR values are associated with the sensor that has the lowest porosity and vice versa. Moreover, the temperature sensors fabricated using the diEG films, which exhibit a porosity between monoEG and triEG, have TCR values between these two inks. Although the effect of sheet resistance on TCR cannot be completely ruled out, the fact that the TCR values do not converge for long plasma exposure times even though the sheet resistance values do suggests that porosity plays a much stronger role in governing TCR. The low TCR values associated with the monoEG ink for the two shortest plasma exposure times is likely due to the fact that these structures are relatively thin and the sheet resistances are high as indicated in Figure 2-6. For the monoEG ink, the TCR reaches its maximum value for the same plasma exposure time that the sheet resistance reaches its lowest value, suggesting a connection between sheet resistance and TCR.

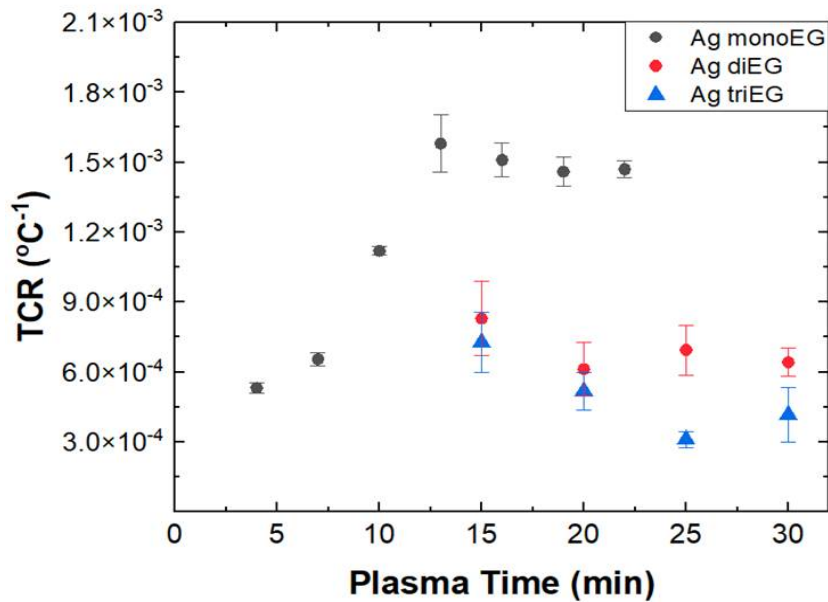


Figure 2-31: TCR versus plasma exposure time for temperature sensors fabricated using the monoEG, diEG and triEG inks.

2.4.4.2 Cyclic Testing

Cyclic thermal testing was performed in order to examine sensor repeatability and reliability. Testing was performed on temperature sensors fabricated using each ink that exhibited the highest TCR in its ink class. Each temperature cycle ranged from 22 °C to 60°C and back to 22°C. Figure 2-32 presents a plot of relative change in resistance versus cycle number for these three sensors. For the sensor printed using the monoEG ink, the resistance readings shifted upwards during the first 5 cycles and, subsequently stabilized thereafter. In contrast, the temperature sensors printed using the diEG exhibited a slight downward shift in relative change in resistance during the first 4 cycles while that for the triEG ink remained constant throughout the test. With respect to ink solvent, the cyclic testing is consistent with the observations associated

with the aforementioned TCR measurements in that the sensor fabricated using the monoEG ink maintained the highest TCR (as evidenced by the highest normalized change in resistance), following by the sensor printed using the diEG ink and then by the sensor fabricated using the triEG ink throughout the entire 15 cycle testing period.

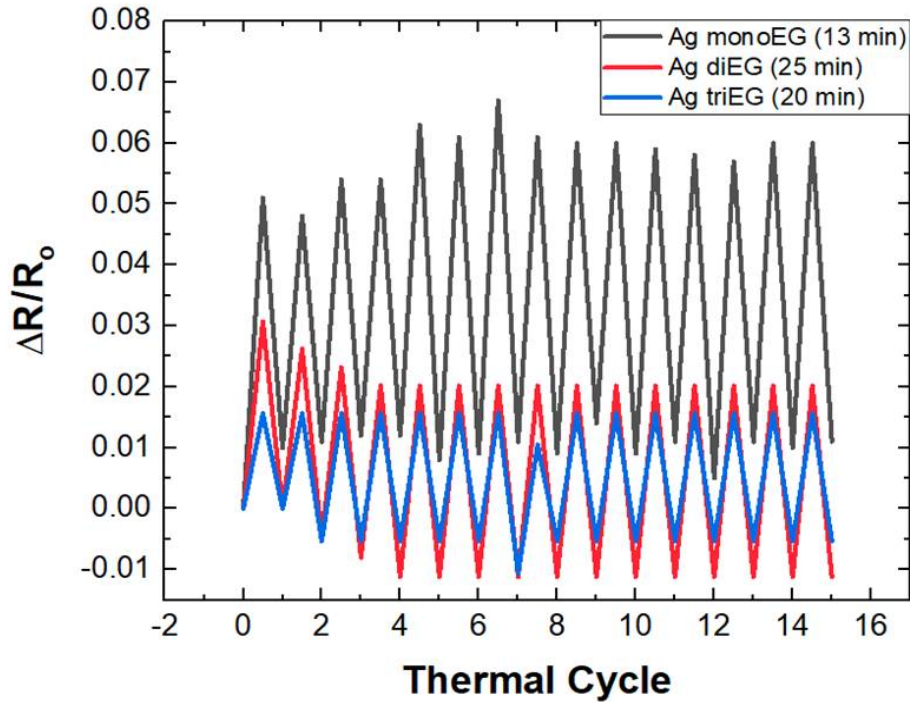


Figure 2-32: Cyclic thermal testing for temperature sensors fabricated using each of the ink formulations. The samples were treated under plasma exposure times that yielded a maximum TCR value for each ink formulation.

2.4.4.3 TCR and Microstructure

The TCR of a temperature sensing material can be computed using the following equation:

$$\rho = \rho_o[1 + \alpha(T - T_o)] \quad (6)$$

where T_o is the reference temperature, T is the current temperature, ρ is the resistivity at temperature T , ρ_o is the resistivity at temperature T_o and α is the temperature coefficient. Solving for α in equation 6 yields:

$$\alpha = \frac{\rho - \rho_o}{\rho_o(T - T_o)} = \frac{1}{\rho_o} \frac{\Delta\rho}{\Delta T} \quad (7)$$

Equation 7 suggests that α is inversely proportional to ρ_o . Hence, if the resistivity of a material at its reference temperature rises, its TCR decreases accordingly.

Equation 6 and 7 apply to metallic materials. However, one must take into account that in metals, crystalline defects serve as scattering sites for electrons; thereby resulting in an increase in resistivity. The concentration of these defects in a metal specimen is determined by temperature and material impurities. Matthiessen's rule states that the total resistivity of a metal is the sum of the resistivities due to impurity scattering, thermal vibrations and plastic deformation, and is mathematically expressed as follows:

$$\rho_{Total} = \rho_T + \rho_i + \rho_d \quad (8)$$

where ρ_T is the thermal resistivity, ρ_i is the resistivity contribution due to impurities and ρ_d is the resistivity contribution due to plastic deformation. An increase in

temperature will increase the thermal vibrations as well as lattice vacancies, which in turn increases electron scattering. As for impurities, when the concentration increases in a metal, electron scattering events increase, which translates into an increase in resistivity. Plastic deformation also increases the chances of electron scattering, which also contributes to a rise in the total resistivity. (Callister and Rethwisch 2011)

The increase in TCR with increasing plasma exposure time for the sensors printed using the monoEG ink between 4 minutes and 13 minutes can be attributed to Ag nucleation and film growth. After plasma exposure, the Ag film has a reflection boundary with an AgNO₃ layer that lies beneath the newly formed Ag layer (Sui, Ghosh et al. 2018). This layer is formed from Ag ions that are not reduced by the plasma and instead react with NO₃⁻ ions to reform AgNO₃. This interface increases electron scattering, which reduces the TCR of the Ag film. As the plasma exposure time increases, the thickness of the Ag layer increases while that of the AgNO₃ layer decreases, leading to a reduction in boundary scattering and an increase in TCR. The TCR saturates at a maximum value when the Ag layer reaches a critical thickness.

These observations suggest that there is a link between material properties and temperature sensor performance, as was the case with the strain gauge device. The results of single and cyclic temperature change tests of the three Ag ink solvents can be attributed to the microstructure of the test specimen. The results reported in (Sui, Hess-Dunning et al. 2022) and the SEM images in Figure 2-7 indicate that porosity is lowest in the Ag monoEG printed structures. As mentioned previously in Equation 6, the TCR is inversely proportional to resistivity. This is also reported by (Alhendi, Sivasubramony et al. 2020). This suggests that the sensors fabricated using the

monoEG ink exhibit the highest TCR values as a result of their dense microstructure relative to their di- and triEG counterparts.

According to Matthiessen's rule (Equation 8), the total resistivity of a material is dependent upon electron scattering by temperature-sensitive lattice vibrations (phonons) and lattice imperfections due to grain boundaries and microcracks (Peterson 2007, Alhendi, Sivasubramony et al. 2020). That the sensors printed using the monoEG ink exhibit the highest TCR values ($1.7 \times 10^{-3} \text{ }^\circ\text{C}^{-1}$) is consistent with this analysis since these structures have the densest microstructure and lowest sheet resistance. In contrast, the TCR values for sensors fabricated using the triEG, which exhibit the highest porosity for roughly the same sheet resistance, are nearly 50% lower ($\sim 7.5 \times 10^{-4} \text{ }^\circ\text{C}^{-1}$).

Chapter 3

Fabrication of Resistor-based Zn Devices via Selective Chemical Deoxidation of ZnO Inks by Reactive Inkjet Printing

3.1 Introduction

3.1.1 Zn Microparticles

Zinc (Zn) is a common metal found in water, air and soil. Generally, it harmlessly decomposes in the environment and dissolves in biological fluids such as saliva, blood and urine (Zheng, Gu et al. 2014). As such it is viewed as one of only a few metals that can be safely used in biodegradable circuits and thus is considered the leading metal to be used in environmentally-friendly printed electronics (Tan, Owh et al. 2016), in particular those to be used in biodegradable electronics (Chang, Fang et al. 2017, Lu, Liu et al. 2019).

Zn microparticles readily oxidize under ambient conditions forming a zinc-oxide (ZnO) layer on their surfaces. Although this layer is a few tens of nanometers in thickness, it is electrically insulating. As such, Zn-based microparticle inks commonly used in screen printing have relatively high electrical resistivities associated with this oxide surface coating. Syaizwadi et al. investigated the effect of sintering on crystallinity of ZnO (Syaizwadi, Noradilah et al. 2018). X-ray Diffraction (XRD) showed that as the ZnO sintering temperature was elevated from 900, 1100 and 1300°C, the XRD spectra became more intense and were narrower in full width at half maximum (FWHM), indicating improved Zn crystallinity. They also investigated the I-V characteristics and found that the electrical resistance of ZnO decreased from 20k Ω to 5k Ω when the sintering temperature increased from 900 to 1300 °C (Syaizwadi, Noradilah et al. 2018). Since ZnO has high melting temperature (*e.g.* 1975 °C), thermal sintering of Zn microparticles is challenging as it requires temperature conditions that are impractically high for most device applications.

3.1.2 Zn Sintering at Room Temperature

As a low temperature alternative to thermal sintering, Lee et al. developed a process to electrochemically sinter Zn microparticles at room temperature (Lee, Kim et al. 2017). The process was developed for screen printing using an ink that contained a Zn powder, poly-vinyl-pyrrolidone (PVP) as a binder, and isopropyl alcohol as a solvent. After drying and exposure to air, the screen-printed Zn structures became oxidized forming ZnO structures. To remove the oxide layer, the screen-printed structures were exposed to an aqueous solution of acetic acid. Small volume, manual

drop casting ($< 100\mu\text{L}$) was used to dispense the acetic acid solution onto the screen-printed structures. This deoxidation step initiated a self-exchange of Zn and Zn^{2+} between adjacent particles (Lee, Kim et al. 2017) facilitating the formation of continuous, electrically conducting Zn structures. Figure 3-1 shows the effect of deoxidation and electrochemical sintering on the electrical resistance of the screen-printed Zn structures. The data show that the resistance dramatically dropped from $\sim 300\text{ k}\Omega$ to $\sim 9\Omega$ within a period of 180 seconds, with the most dramatic decrease occurring in the first ~ 50 seconds. While this method appears to be well suited for applications that require low resistance structures, it also suggests that drop casting is likely to be ineffective in achieving structures with moderate to high electrical resistances. This data does however suggest that such structures could be fabricated if a more precise method to dispense the acetic acid were developed.

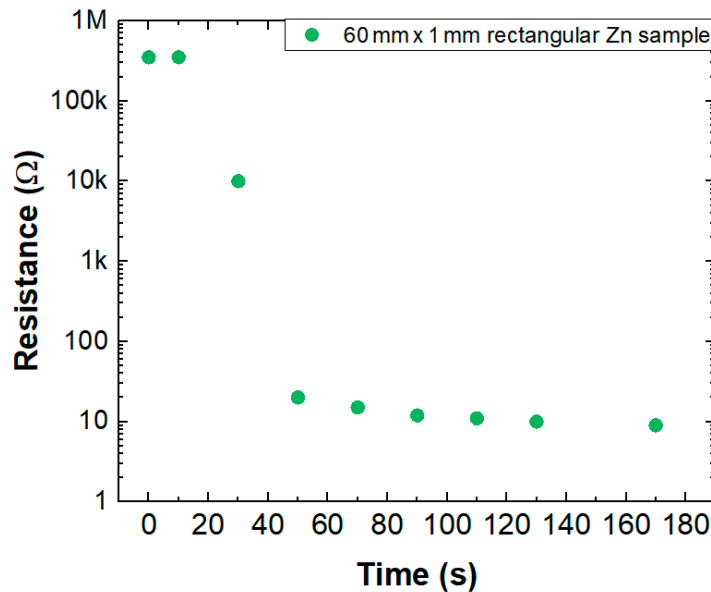


Figure 3-1: A plot of resistance versus time for a 60 mm x 1 mm rectangular Zn sample drop cast with acetic acid. Upon drop cast treatment, the plot shows a dramatic drop in resistance over a 180 second period. Adapted from (Lee, Kim et al. 2017) with permission from John Wiley and Sons.

Although deoxidation and electrochemical sintering by manual drop-casting is a simple method to form Zn structures compared to thermal, optical or electrical methods (Ferguson, Chaudhury et al. 1991, Lu, Huang et al. 2010, Magdassi, Grouchko et al. 2010), conventional drop casting of extremely small liquid volumes by is difficult to control. Therefore, the drop casting method is limited to producing high conductive patterns used in the fabrication of, for example, electrodes, capacitors or inductors. The drop casting method has its risks in that excessive acetic acid exposure can actually promote the formation of a new passivation layer that can compromise electrical conductivity (Sui, Radwan et al. 2022).

3.1.3 Reactive Inkjet Printing

Although inkjet printers are intended to dispense liquid inks, these systems are essentially high precision liquid dispensing systems capable of dispensing small volume (pico liter range) droplets at proscribed locations (Meier, Löffelmann et al. 2009). Such an attribute can also be utilized to dispense pico-liter chemical droplets at reaction sites; and multiple pico liter droplets of a reactant can be simultaneously dispensed, enabling chemical reactions to be performed at a smaller scale with precision than can be achieved by micro-liter drop casting. This process is known as reactive inkjet printing (RIJ) (Smith and Morrin 2012).

By RIJ printing, it is potentially feasible to use an inkjet printer as a high precision acetic acidic dispenser to form electrically continuous Zn structures by selective deoxidation and electrochemical sintering of Zn microparticles. Unlike drop

casting, inkjet printing could potentially enable the resistivity of Zn structures to be tuned during the deoxidation process by controlling the amount of acetic acid that is available for the deoxidation reaction. Moreover, inkjet printing offers precision lateral control of the dispensing process which could enable the fabrication of both conductive and resistive structures from the same screen printed Zn layer.

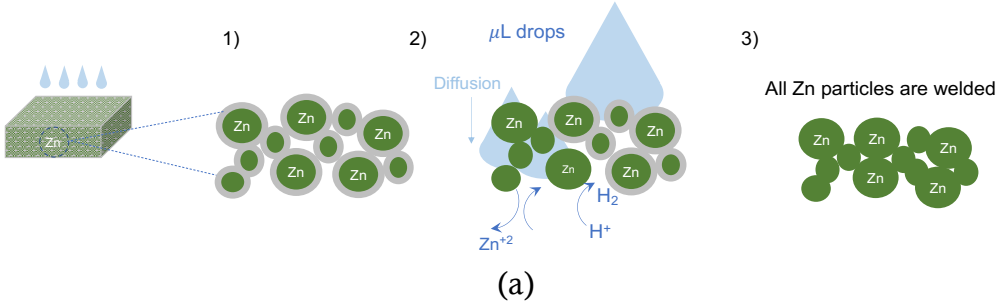
Sui, et al, recently published the first demonstration of electrochemical sintering of screen printed Zn structures by RIJ printing with a focus on fabricating structures with low electrical resistivity (Sui, Radwan et al. 2022). In this work, an ink comprised of oxidized Zn microparticles and a low vapor pressure N-methyl-2-pyrrolidone (NMP) solvent was used for screen printing. RIJ printing was used to dispense aqueous acetic acid solution onto the screen-printed structures with precision control of both volume and location. The authors reported improved electrical resistivity relative to drop casting. Moreover, it was reported that RIJ printing also played a critical role in preserving the pattern fidelity of the screen-printed Zn structures by suppressing pattern smearing caused by excessive exposure to acetic acid. Zn-based radio frequency identification (RFID) antenna devices fabricated using the RIJ printing process exhibited more than a two-fold increase in antenna reading distance relative to the same devices fabricated using drop casting (Sui, Radwan et al. 2022).

3.1.4 Electrochemical Sintering of Zn by Reactive Inkjet Printing

Figure 3-2 is a conceptual illustration that compares the conventional drop casting method of deoxidation and electrochemical sintering to the proposed reactive inkjet printing method to be developed in this dissertation. In manual drop casting,

micro liter amounts of acetic acid are dispensed and diffused into bulk of the Zn microparticles and thus the passivation layers encapsulating the Zn microparticles are dissolved en masse, resulting in the cold-welding of a high percentage of the Zn microparticles (Lee, Kim et al. 2017) throughout the bulk of the structure. On the other hand, inkjet printing dispenses pico liter amounts of acid in each print pass. Because the droplet volume is six orders of magnitude smaller than the droplets associated with drop casting, only a fraction of the Zn microparticles are subject to deoxidation and electrochemical sintering. Because the number of welded microparticles after a single print pass of acetic acid is significantly less than that of the drop casting method, the resulting electrical resistance is higher. To achieve lower resistance, repeat print passes can be performed in order to dispense additional acetic acid drops to deoxidize untreated Zn microparticles and induce additional welding. This dissertation aims to answer the question as to whether pico-liter dispensing of acetic acid via reactive inkjet printing can be used to tune the sheet resistance of screen printed Zn structures over a useful range for resistor-based Zn devices.

Drop casting:



Reactive Inkjet Printing:

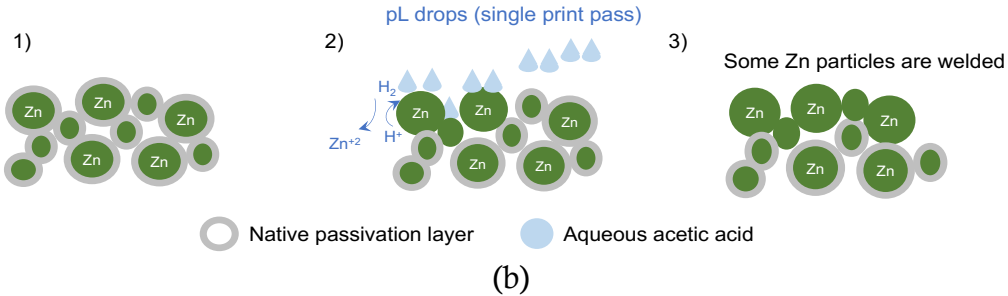


Figure 3-2: Concept drawing of electrochemical sintering of Zn microparticles by acetic acid using: (a) conventional drop casting and (b) the proposed reactive inkjet printing.

3.1.5 Scope of this Research

In this part of the dissertation, a method to dispense an acetic acid deoxidizing agent on screen printed Zn structures with an extremely high degree of volumetric and spatial control based on RIJ printing with an eye towards fabricating resistor-based devices was developed. This RIJ process precisely controls the amount of acetic acid deposited on the surface of screen-printed Zn ink structures. Inkjet printing parameters, including the number of print passes and drop spacing, can be utilized to control the amount of acetic acid dispensed on the printed Zn structure, thus enabling

unparalleled control of the deoxidation process and electrochemical sintering. Both Zn screen printing and RIJ are performed at room temperature, which makes the process compatible with temperature-sensitive substrates, including many that are attractive for flexible, wearable and biodegradable electronics. The substrate only needs to be inert to acetic acid.

3.2 Process Development

A screen-printable Zn ink using a formulation first described elsewhere (Sui, Radwan et al. 2022) was made from a mixture of Zn powders (1-5 μm particle size, Goodfellow, Coraopolis, Pennsylvania, USA), N-Methyl-2-Pyrrolidone (NMP) (Sigma Aldrich, St. Louis, Missouri, USA) and polyvinylpyrrolidone (PVP) (Sigma Aldrich, St. Louis, Missouri, USA). First, in a glass vial, 1 g of PVP powder was mixed with 5 g of NMP. The weight-to-weight ratio was 1:5 (PVP:NMP = 1:5 w/w). This 1:5 w/w, PVP/NMP mixture was stirred for 48 hours on a 50°C hotplate. Then, 30g of Zn powder was added to the PVP-NMP solution (Zn:PVP-NMP = 30:6 w/w). Immediately following this step, the mixture was loaded into a vortex mixer (Genie SI-0236, Scientific Industries, Bohemia, New York, USA) which was operated at 3200 rpm for 3 min to fully disperse the contents of the mixture. Lastly, a spatula was used to manually stir the Zn:PVP-NMP mixture to improve dissolution.

A screen with the desired patterns was designed in house and fabricated by an outside vendor (Speedline MPM-SPM, SMTNet, Portland, Maine, USA). A stainless-steel mesh (325 Cal, 0.0011 in wire diameter, 0.002 in wire opening, SEFAR Inc., Buffalo, New York, USA) with a pre-imaged screen was used to make a series of

2 x 20 mm² rectangular test specimens for two point resistance measurements and a series of 20 x 20 mm² square samples for sheet resistance measurements. Using this screen, Zn patterns were created on glass slide substrates following the standard screen printing process illustrated in Figure 3-3a.

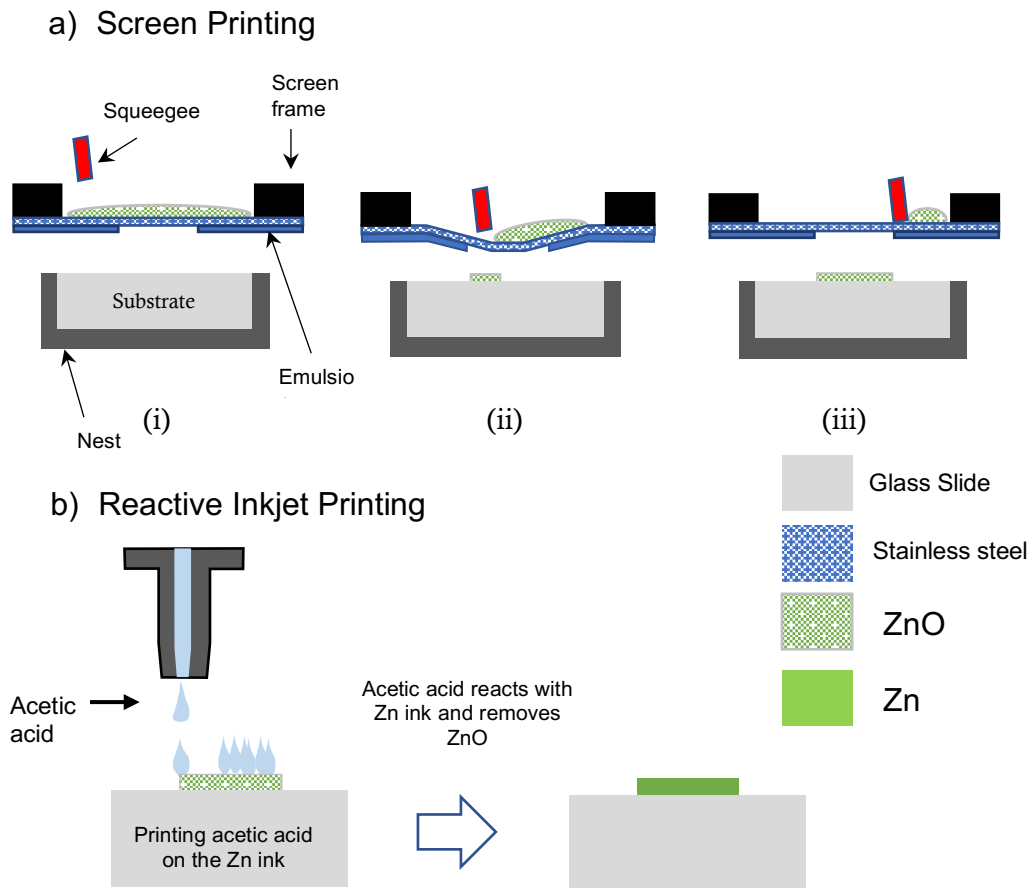


Figure 3-3: Screen printing and reactive inkjet printing process

Inkjet printing was used as a method to locally deliver the chemical deoxidizing agent to the screen printed Zn patterns. An inkjet printer (DMP-3000, Fujifilm Dimatix, Japan) was used to deposit the acetic acid deoxidizing agent. The acetic acid was diluted in deionized (DI) water (acetic acid: DI water = 1:10 v/v). This

agent was loaded in a DMP-11610 material cartridge for inkjet printing. Then, screen-printed Zn ink samples were placed on the printer platen. The temperature of the platen was set at 45°C. The image patterns that control the position of the print head were set to be approximately 5% larger than the screen-printed structures in order to ensure complete coverage of the entire Zn ink pattern by acetic acid droplets, including the side walls, during each pass of the printer. Figure 3-3b is a schematic diagram of the acetic acid-based reactive inkjet printing process.

For process development purposes, the aforementioned rectangular samples were prepared on electrically insulating glass slides for two-point resistance measurements. Each 2.5 x 20 mm² sample was approximately 80 µm thick after screen printing. Silver epoxy was applied to the ends of the rectangular samples to form electrodes. These samples were subjected to the aforementioned reactive inkjet printing process to deoxidize the screen-printed Zn-based ink. Samples were prepared using drop spacings of 15, 25 and 35 µm. After each print pass, the resistance of each sample was measured using a handheld multimeter (Fluke 79 III), with probes placed on the silver epoxy electrodes. Figure 3-4 presents a plot of the resistance versus number of print passes for each of the three drop spacings included in this study.

Figure 3-4 clearly shows a strong dependence of the electrical resistance on both drop spacing and number of print passes, with the resistance changing by 2 orders of magnitude depending on process parameters, but ultimately saturating at 1 to 2 Ω depending on the drop spacing. The highest range of resistance values, therefore the highest degree of tunability, is associated with a drop spacing of 35 µm. Saturation is achieved with the fewest number of passes; *e.g.* 9 print passes in the sample treated

using the smallest drop spacing (15 μm). Conversely, saturation is achieved after 14 print passes for samples treated using a drop spacing of 35 μm .

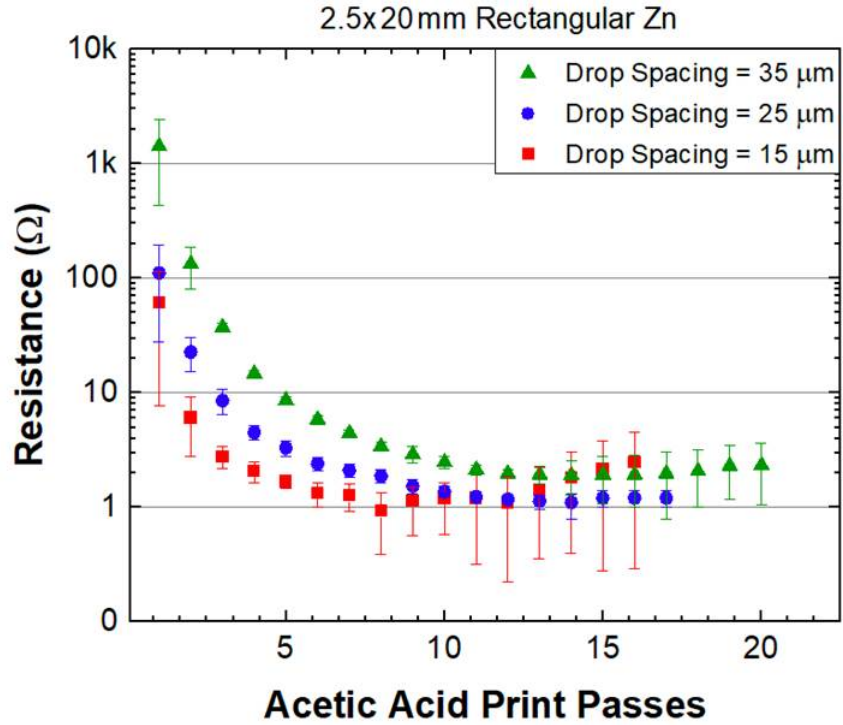


Figure 3-4: Resistance of rectangular pattern Zn ink versus the number of acetic acid print passes at 15, 25 and 35 μm printer drop spacing. (Sui, Radwan et al. 2022).

Test specimens were also prepared for sheet resistance measurements. The screen printing and reactive inkjet printing steps were identical to those used to make the resistor samples for the two-point measurements. The test specimens consisted of 20 x 20 mm² squares and, like the linear resistors, were also approximately 80 μm in thickness. Figure 3-5 presents plots of sheet resistance versus number of print passes for drop spacings of 15, 25 and 35 μm . For a drop spacing of 35 μm , the sheet resistance

decreases by roughly an order of magnitude after each acetic acid print pass. After 8 print passes, the sheet resistance drops below $1 \Omega/\square$. For a drop spacing of $25 \mu\text{m}$, the sheet resistance reaches its minimum value after 6 print passes. However, after 8 passes, the sheet resistance slightly increases for reasons still under investigation but could be due to surface passivation. For a drop spacing of $15 \mu\text{m}$, the sheet resistance drops by about an order of magnitude between 1 and 2 print passes, reaches a minimum at 3 passes and then slightly rises to a value comparable to the $25 \mu\text{m}$ drop spacing for subsequent print passes. As with the two-point resistance measurements, the number of print passes requires to reach the minimum sheet resistance decreases with decreasing drop spacing.

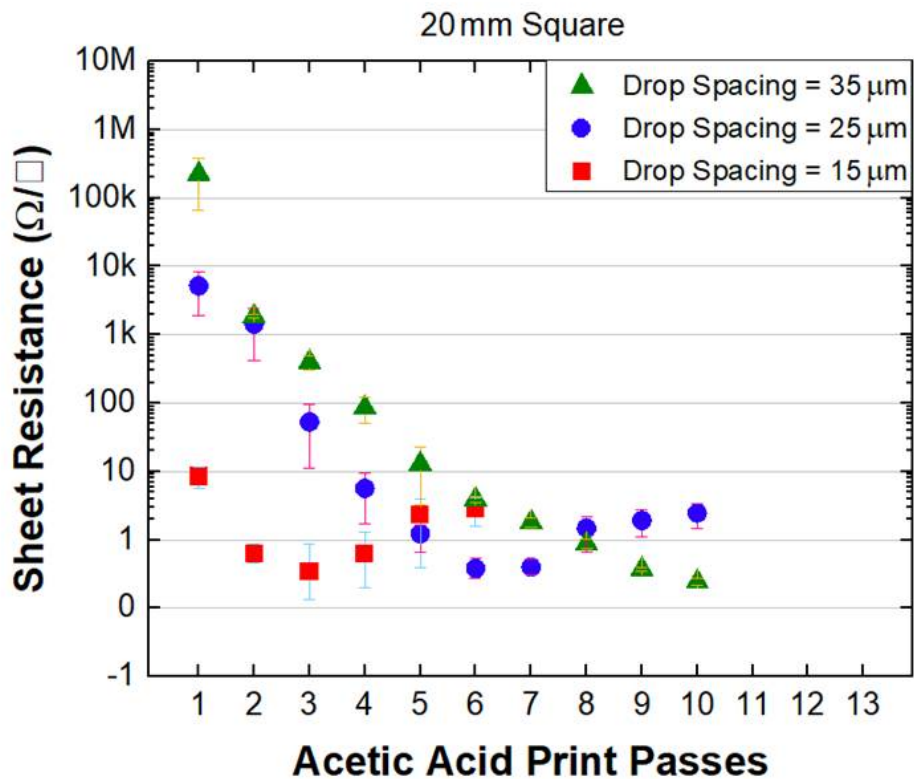


Figure 3-5: Sheet resistance of 20 mm square Zn ink samples versus the number of acetic acid print passes at 15, 25 and 35 μm printer drop spacing. (Sui, Radwan et al. 2022).

3.3 Material Characterization

3.3.1 X-Ray Diffraction

Conventional X-ray diffraction (XRD) was performed on as-printed samples as well as samples treated with acetic acid to determine the effect of acetic acid exposure on the crystallinity of the screen-printed structures. A Bruker AXS system was used to perform the XRD measurements. Samples were printed on glass slide substrate to ensure that the spectra contained no X-ray peaks from the substrate. Figure 3-6 shows

XRD spectra from an as-printed sample (zero print passes), a sample treated with 4 print passes, a sample treated with 8 print passes and a sample treated by manual drop casting. Each of the spectra contains diffraction peaks associated with the (002), (101) and (102) planes of crystalline Zn. The relative intensities of these diffraction peaks vary slightly with treatment conditions, but no systematic variation with respect to acetic acid exposure is observed, suggesting that such variation is most likely due to variations in the crystal structure of the Zn microparticles.

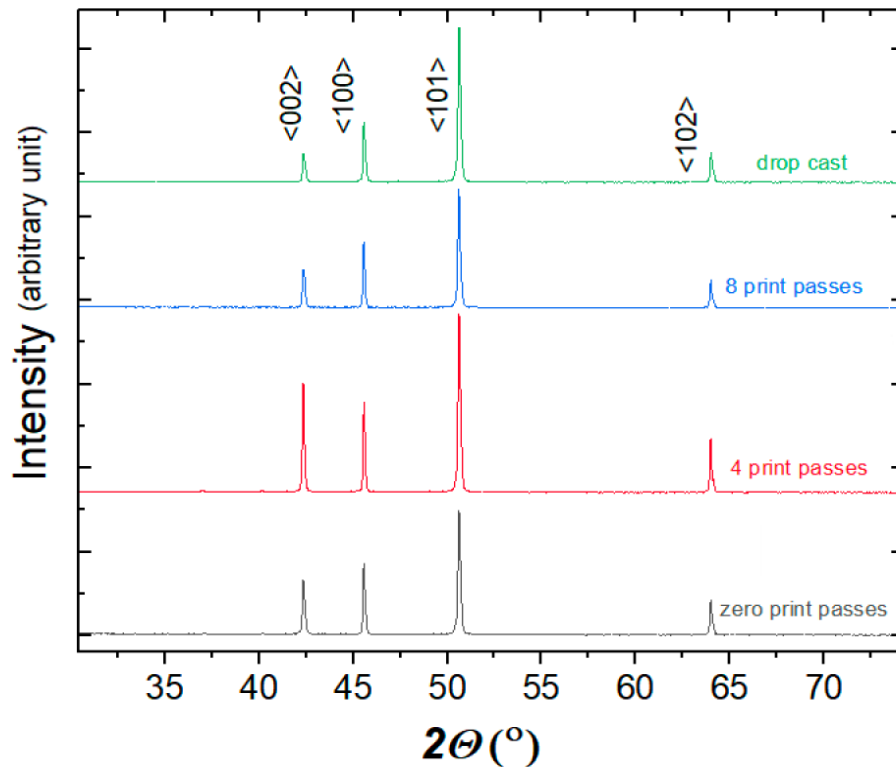


Figure 3-6: XRD spectra from an as-printed sample (zero print passes), a sample treated with 4 print passes, a sample treated with 8 print passes and a sample treated by manual drop casting.

3.3.2 Scanning Electron Microscopy (SEM)

SEM imaging was used to assess the morphology and microstructure of the printed Zn structures under various treatment conditions. Figure 3-7 presents low, medium and high magnification plan-view images of as-printed Zn structures as well as structures subjected to 4 print passes and 8 print passes at a drop spacing of 35 μm . As expected, the low and medium magnification SEM images in Figure 3-7a show that the as-printed structures are characterized by a uniform distribution of Zn microparticles in the 1 to 5 μm diameter range that appear to be densely packed. The high magnification image shows that these microparticles are not concatenated. The low and medium magnification images in Figure 3-7b taken from the sample treated with 4 print passes also show a microstructure similar to the as-printed sample. However, the high magnification image from this sample clearly shows evidence of cold welding between two neighboring Zn microparticles. The low magnification image in Figure 3-7c taken from the sample treated with 8 print passes shows a surface that appears to be more dense and less smooth than those from the other two samples. The medium magnification image from this sample shows evidence of cold welding between adjacent microparticles, evidence not seen in the medium magnification images from the other samples. The high magnification image from this sample shows that the density of cold-welded microparticles is the highest of the three samples. In fact, a network of cold-welded particles comprised of microparticles welded to multiple adjacent microparticles, can be seen in the image.

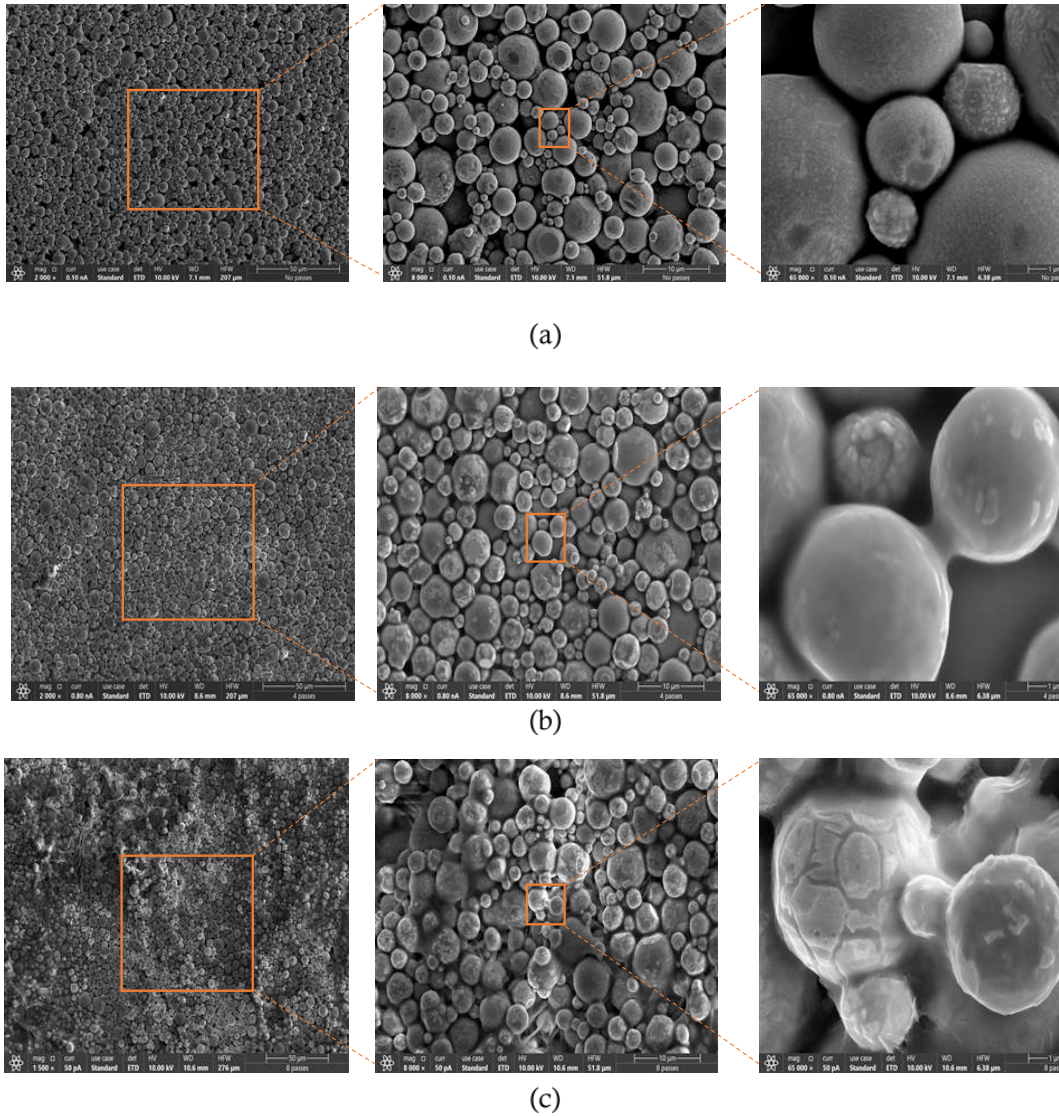
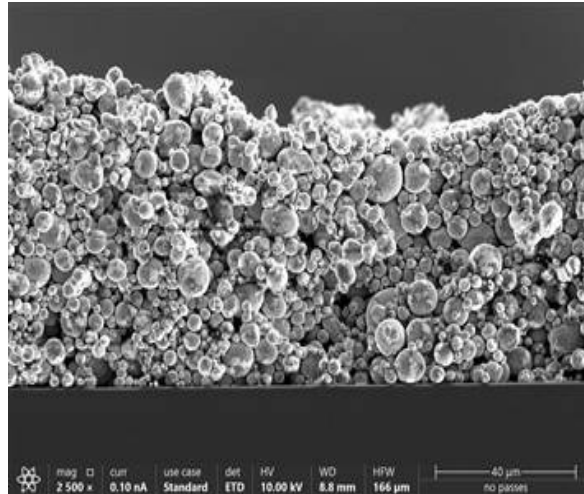


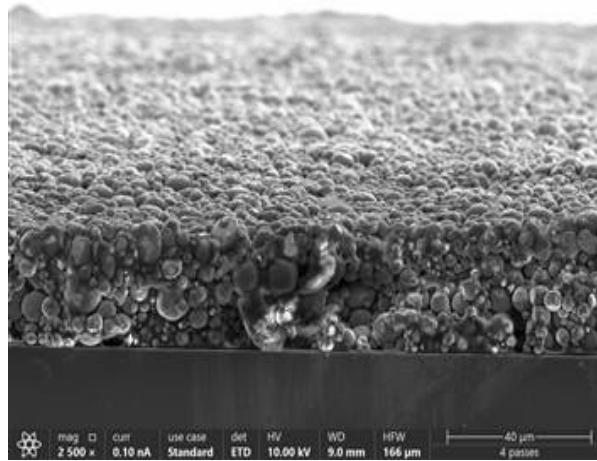
Figure 3-7: Plan-view low, medium and high magnification SEM images of screen printed Zn structures: (a) as-printed, (b) after 4 print passes, and (c) after 8 print passes.

To observe the effects of diffusion of acetic acid into the screen-printed Zn structures, cross-sectional SEM imaging was performed on samples printed on silicon (Si) substrates. Zn structures were printed on the unpolished side of a Si wafer and subjected to acetic acid exposure by RIJ printing for a proscribed number of print

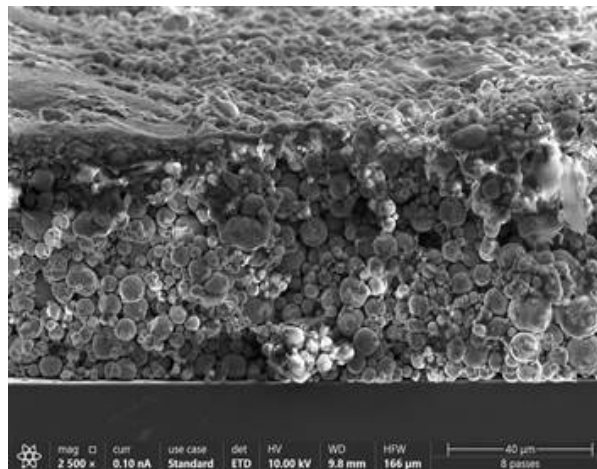
passes. The Si substrate was then cleaved to obtain mechanically sectioned samples for imaging purposes. Figure 3-8 presents cross-sectional SEM images from as-printed samples as well as samples after 4 print passes and 8 print passes. Consistent with the plan view images in Figure 3-7a, the SEM image in Figure 3-8a taken from the as-printed sample shows a dense pack distribution of Zn microparticles that is uniformly distributed throughout the thickness of the structure. There is no evidence of cold welding. The high image contrast between the Zn microparticles and the conducting Si substrate may be due to low intensity charging associated with the high electrical resistance of the Zn structure, a result of native oxide that encapsulates the untreated particles. The SEM image from the sample treated with 4 print passes (Figure 3-8b) indicates a dense pack microparticle structure with some evidence of particle welding and significantly less charging. The SEM image from the sample treated with 8 print passes shows additional evidence of cold welding, in particular in the near surface region of the structure where the structure loses its particle-based microstructure and appears to be fully densified. This SEM image also indicates that the structure consists of two regions; a dense near surface region that sits atop a microparticle base. Image contrasts suggest that the dense near surface region is more conductive than the microparticle base.



(a)



(b)



(c)

Figure 3-8: Cross-sectional SEM images of screen printed Zn structures: (a) as-printed, (b) after 4 print passes, and (c) after 8 print passes.

3.3.3 Analysis and Discussion

The XRD spectra presented in Figure 3-6 strongly indicate that exposure of the screen-printed Zn structures to acetic acid by drop casting and reactive inkjet printing did not result in a change in crystal orientation at the macroscale level. As such, the observed changes in sheet resistance and electrical resistance with respect to the drop spacing and number of print passes presented in Figures 3-4 and 3-5 cannot be ascribed to a change in crystal orientation. To investigate if the observed changes are related to changes in crystallite (grain) sizes as a result of acetic acid exposure, the crystallite sizes (D) for as-printed samples and samples treated with acetic acid using RIJ printing and drop casting were calculated using Scherrer equation:

$$D = \frac{k \lambda}{\beta_{hkl} \cos \theta_{hkl}} \quad (9)$$

where k is the dimensionless shape factor ($k = 0.9$), λ is the wavelength (= 0.179 nm for Co k-alpha source), β is the half-width of the diffraction band in radians and θ_{hkl} is the Bragg diffraction angle in radians.

Figure 3-9 shows the calculated crystallite sizes for each diffraction peak in the XRD spectra presented in Figure 3-6 with respect to the treatment conditions of the test specimens. In general, the crystallite sizes range from ~ 60 to ~80 nm depending on the crystal orientation. With respect to treatment conditions, the crystallite size associated with the (101) orientation is insensitive to acetic acid exposure. The crystallite size associated with the (102) peak initially increases by ~ 10 nm relative to as-printed Zn after 4 print passes and then decreases to nominally 60 nm after drop casting. Likewise, a similar trend is observed for the (100) and (002) orientations.

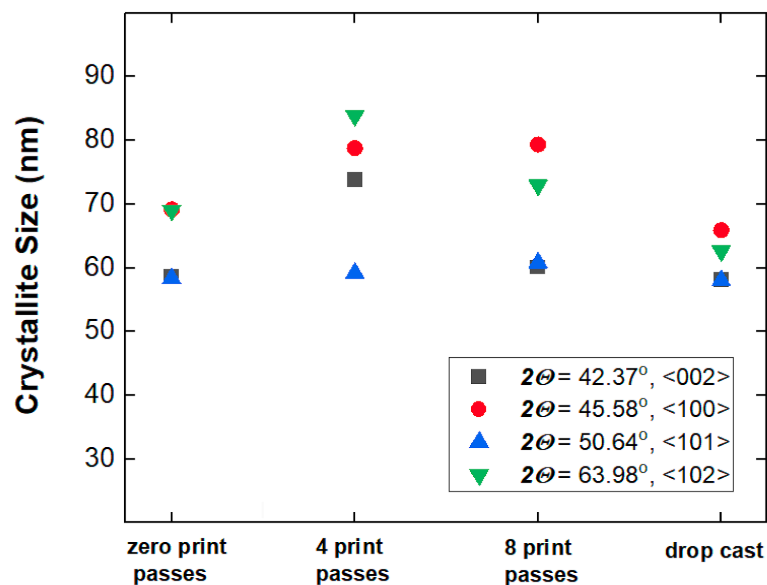


Figure 3-9: Calculated crystallite sizes from the XRD spectra presented in Figure 3-6. The inset indicates the XRD peaks used in this analysis.

Figure 3-10 illustrates the relationship between particle size and crystallite size. The crystallite size is typically submicron in size (He 2018). With respect to the screen-printed Zn microparticle structures developed in this dissertation, the XRD data presented in Figure 3-6 can be interpreted in one of two ways. The spectra could indicate that the structures are comprised of single crystal Zn particles with a particle distribution indicated by the individual diffraction peaks. The data in Figure 3-9 would then suggest that the average crystallite size is in the 60 to 80 nm range which is counter to the SEM images in Figures 3-7 and 3-8. A more likely interpretation is illustrated in Figure 3-10, in which the Zn particles are polycrystalline, with each particle comprised of (002), (100), (101) and (102) grains with grain sizes in the 60 to 80 nm range. The data presented herein is insufficient to determine a connection between grain size,

acetic acid exposure and electrical resistivity. However, the SEM images strongly suggest that the principal mechanism associated with electrical resistivity is the density of cold welds between adjacent Zn particles that is facilitated by deoxidation using acetic acid.

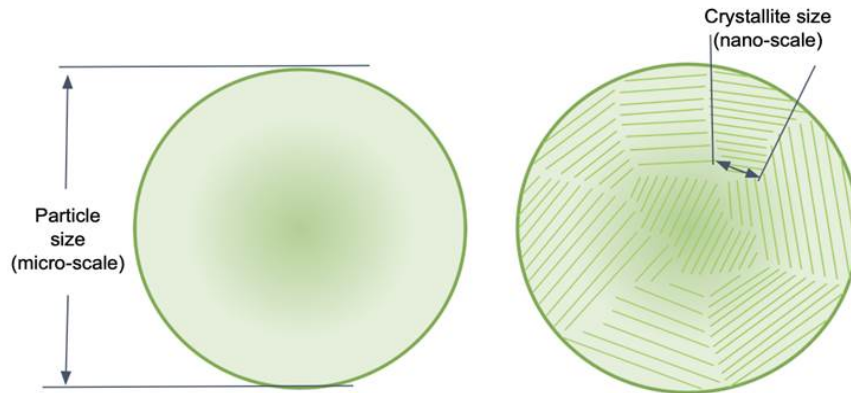


Figure 3-10: Illustration of particle size and crystallite size for a polycrystalline microparticle. The crystallite size is typically submicron in size. *Adapted in part from (Domi, Usui et al. 2019) with permission from John Wiley and Sons.*

3.4 Development of Zn-based Microheaters

3.4.1 Introduction

Recently, there has been an interest in flexible printed heaters due to their versatile applications in medical as well as wearable thermotherapy (Liu, Tian et al. 2020, Hu, Wang et al. 2021). Table 3-1 summarizes recent flexible heaters fabricated by different printing methods. Owing primarily to the popularity and availability of nanoparticle inks and the required printing processes, a common material used in printed microheaters is Ag. To the best of our knowledge, a printed microheater that incorporates a Zn heating element has yet to be developed.

Table 3-1: Summary of recently reported printed microheaters

	Printing Method	Printed Heater Material	Substrate Material	Resistance	Input Voltage → Temperature
<i>(Tiwari, Bhat et al. 2018)</i>	Screen Printing	Silver ink (LOCTITE ECI 1010)	PET	12 Ω	1.05 – 2.7 V → 37 – 92 $^{\circ}\text{C}$
<i>(Zhang, Huang et al. 2019)</i>	Surface Modification and Ion Exchange (SMIE) process	Silver (Prepared by inkjet printed carbon as a mask)	Polyimide	128 – 220 Ω	10 – 18V → 80 – 220 $^{\circ}\text{C}$
<i>(Liu, Tian et al. 2020)</i>	Screen Printing	Cu @ Ni rose-stem nanowires (RSNWs)	Paper	10 – 12 Ω	2 – 6 V → 45 – 175 $^{\circ}\text{C}$
<i>(Hu, Wang et al. 2021)</i>	Electro-Hydro-Dynamic (EHD) printing	Silver flake/polyaniline (PANI) composite ink	PET	18 Ω	0.5 – 2 V → 34 – 127 $^{\circ}\text{C}$
<i>(Mitra, Thalheim et al. 2021)</i>	Inkjet Printing	Silver nanoparticle	PEN	35 - 130 Ω (different design versions)	0.5 – 15 V → 25 – 120 $^{\circ}\text{C}$

Fundamentally, microheaters consist of a simple microfabricated resistor that exhibits stable electrical and chemical properties when heated. Functionally, when the resistor element of a microheater is supplied with an appropriate DC voltage, constant current flows through the structure which results in the dissipation of power by resistive Joule heating. The electrical power associated with the microheater can be calculated using:

$$P = \frac{V^2}{R} \quad (10)$$

where V is the applied voltage, and R is the resistance of the heating element. The dimensions of the microheater are selected such that a significant fraction of the electrical power associated with the resistive element is dissipated as heat.

3.4.2 Development of Linear Zn-based Microheaters

To evaluate the utility in using the aforementioned reactive inkjet printing process to fabricate Zn based microheaters, simple linear, resistive heating elements were fabricated on glass slides by screen printing and acetic acid exposure by inkjet printing. Figure 3-11 presents a photograph of a printed straight line microheater. Silver epoxy was placed on both ends of the resistor to serve as contact pads. These structures were 20 mm long, 2.5 mm wide and 80 μm thick. A drop spacing of 15 μm was used during the reactive inkjet printing step. Table 3-2 lists the measured resistance after each acetic acid print pass. From these data, it was determined that the first prototype microheater would be fabricated using 9 print passes and have a resistance of 5.9Ω , based in part from observations in Figure 3-5 which show that excessive acetic acid exposure, even by RIJ printing, can lead to an increase in electrical resistance.



Figure 3-11: A 20 mm x 2.5 mm Zn ink sample on a glass slide. The sample was sat on paper for better image capture.

Table 3-2: Resistance of a rectangular sample ($L = 20 \text{ mm}$, $w = 2.5 \text{ mm}$) after each acetic acid print pass

Number of Print Passes	Measured Resistance (Ω)
0	Open Circuit
1	3300
2	210
3	21
4	10
5	7.0
6	6.3
7	6.3
8	5.8
9	5.9

To evaluate the effectiveness of the linear Zn resistors as microheaters, an Agilent E3630A voltage supply was connected in series to the contact pads of each test device and the applied voltage was swept from 0 to 2.5V. A Fluke 79 III meter was used to measure the current through the resistor. An infrared camera was used to measure the temperature at each set input voltage. Figure 3-12 shows a series of images from the IR camera used to determine the temperature of the microheater as a function of applied voltage and Table 3-3 presents the current, electrical power and measured temperature at each input voltage setting. At 2.5V, the measured temperature of the microheater was 119 °C and the associated power was 0.925W. The calculated resistance using the applied voltage and measured current ranged from 5.56 to 6.76 Ω , which is consistent with the measured resistance values and indicates that the

microheater exhibits Ohmic behavior. These data show that the printed Zn structures have a high current carrying capacity and are well-suited for printed microheater applications.

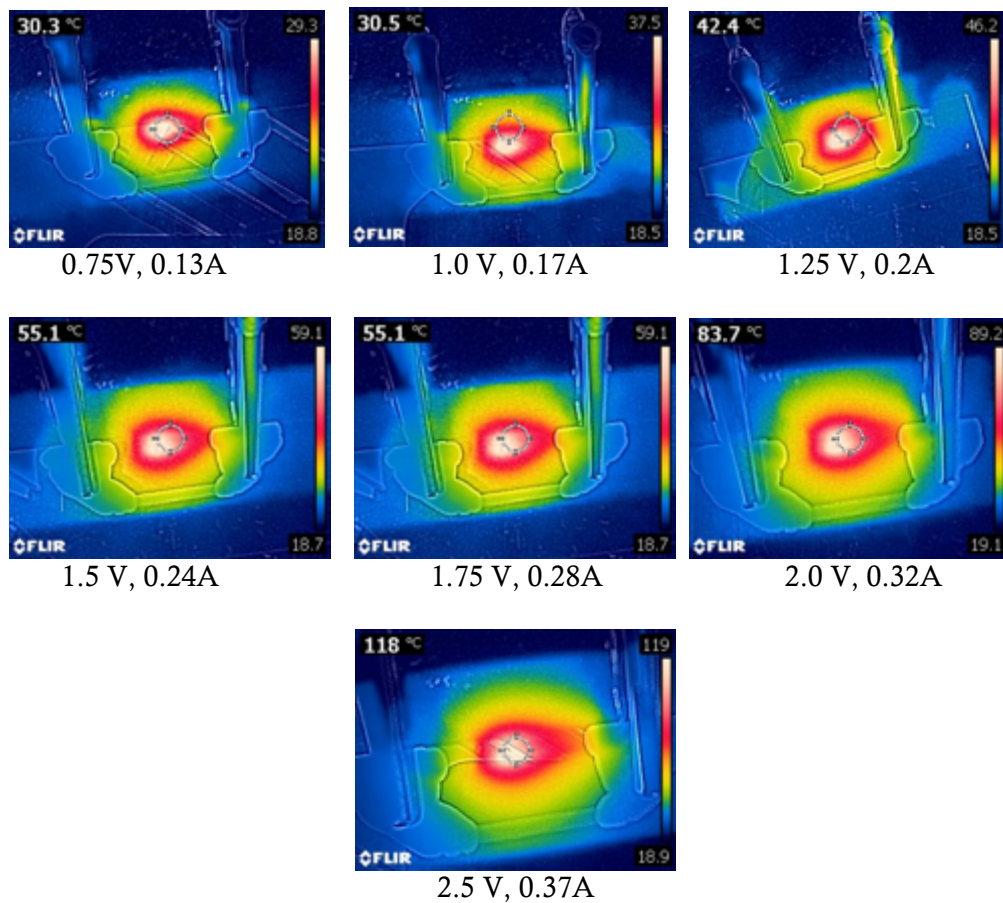


Figure 3-12: Infrared-based temperature measurements from a linear Zn ink microheater for a range of input powers.

Table 3-3: Temperature and power consumption of a representative 20 mm x 2.5 mm Zn linear microheater

Input Voltage (V)	Measured Current (A)	Power Consumption (mW)	Temperature (°C)
0	0	0	22
0.5	0.09	45	24
0.75	0.13	97.5	29
1	0.17	170	37.5
1.25	0.2	250	46
1.5	0.24	360	59
1.75	0.28	490	71
2	0.32	640	89
2.25	0.34	765	98
2.5	0.37	925	119

3.4.3 Development of Spiral and Serpentine Zn-based Microheaters

In addition to the aforementioned linear Zn-based microheaters, the spiral and serpentine microheater designs shown in Figure 3-13 were fabricated using the screen printing process described previously. The 5-turn serpentine and double spiral designs were fabricated on glass substrates whereas the 3-turn serpentine and spiral designs were fabricated on flexible Kapton substrates. Figures 3-14 through 3-19 summarize the development of these microheaters.

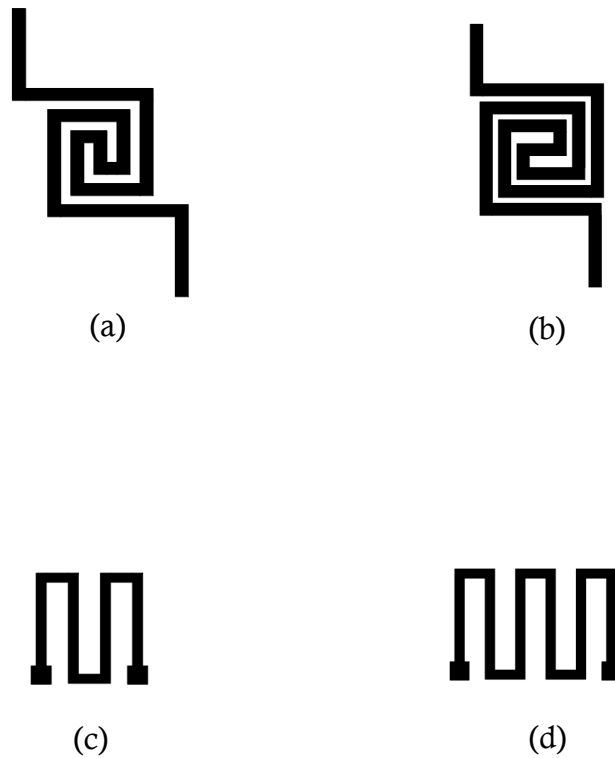


Figure 3-13: Zn Heater designs. (a) Spiral, $w = 1.3$ mm, gap = 1mm, heating area = 147 mm² (b) Double Spiral, $w = 1.3$ mm, gap = 0.65 mm, heating area = 186 mm² (c) Three-Turn Serpentine, $w = 1$ mm, heating area = 127 mm², (d) Five-Turn Serpentine, $w = 1$ mm, heating area = 204 mm²

Figures 3-13 and 3-14 summarize the fabrication and testing of the 5-turn serpentine microheater. Figures 3-14a and 3-14b are photographs of a microheater before and after acetic acid exposure, showing the distinct change in color from white to grey as acetic acid deoxidizes the Zn microparticles. The table in Figure 3-14c details the resistance of the printed structure for each print pass. The 5-turn microheaters were fabricated using 7 print passes to realize a resistance of 20 Ω . Figure 3-15 presents testing data from a 5-turn device. Figure 3-15c presents plots of measured temperature

versus applied voltage and measured input power versus applied voltage for the device imaged in Figure 3-15a and 3-15b. Measured input power was determined by measuring current for each input voltage. Temperatures ranged between room temperature and 118 °C for applied voltages between 0 and 5V. Likewise the input powers ranged between 0W and 1.2W over the same range of applied voltage. In general, the measured temperature exhibited a nonlinear relationship with respect to applied voltage. Likewise, the measured power exhibited a similar relationship with applied voltage. As a direct assessment of the stability of the microheater over the full range of temperature outputs, Figure 3-14c also shows a comparison of measured input power to that of calculated input power over the full range of applied voltages. The calculated input power was determined using the following fundamental equation for power dissipated by a resistor:

$$P = I^2R \quad (11)$$

where I is the measured current for each applied voltage setting and R is the nominal resistance of the microheater at room temperature prior to operating the heater, which for this device was 20 Ω . The calculated power values assume that the resistance of the microheater remains constant over the full range of output temperatures; therefore any difference between measured and calculated power values represents a temperature-induced change in resistance. The two power-related plots in Figure 3-14 are essentially indistinguishable except at applied voltages above 4V, with the largest difference being at 5V. At 5V, the calculated percentage difference in resistance is only 4.17%, indicating that the serpentine Zn microheater is extremely stable over the entire operating temperature range.



Print Pass	Resistance (Ω)
1	14k
2	360
3	66
4	31
5	24
6	21
7	20

(c)

Figure 3-14: (a) As-printed 5-turn serpentine heater on a glass substrate. (b) the device after acetic acid treatment. (c) Measured resistance versus print passes for this microheater.

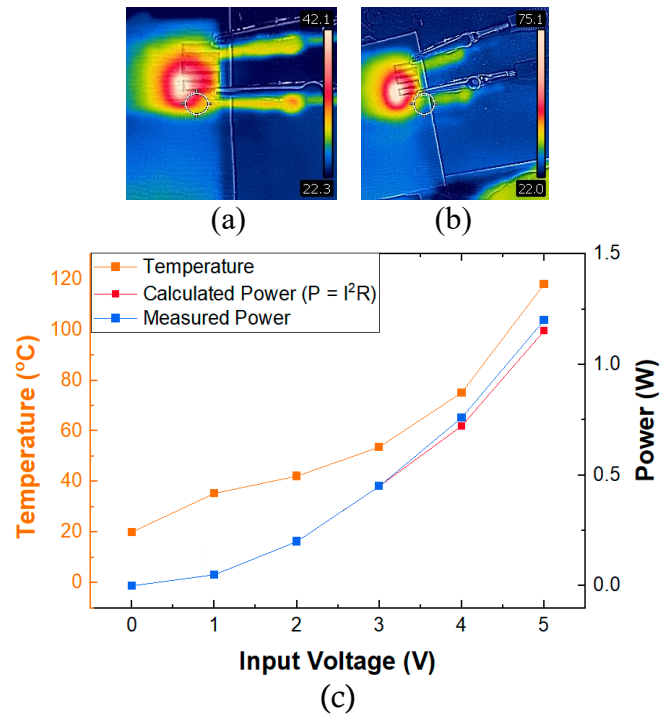
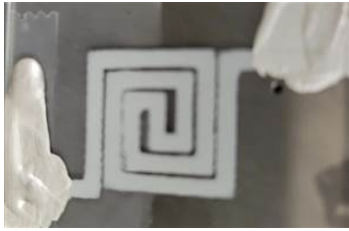


Figure 3-15: (a) Infrared image at 2V (42.1°C). (b) Infrared image at 4V (75.1°C). (c) Plot of temperature and power versus input voltage.

Figures 3-16 and 3-17 summarize the fabrication and testing of a double spiral microheater printed on a glass substrate. The table in Figure 3-16b shows that an acceptable resistance was achieved after 3 print passes. The temperature versus applied voltage plot in Figure 3-17b shows that a maximum temperature of 70°C was achieved at an applied voltage of 6.6 volts. The output temperature exhibits a nonlinear relationship with applied voltage and the measured input power is essentially indistinguishable from the calculated power.

Figures 3-18 and 3-19 summarize the fabrication and testing of a three-turn microheater printed on a Kapton substrate. The table in Figure 3-18b shows that the desired resistance for the heater was achieved after 9 print passes. The temperature versus applied voltage plot in Figure 3-19b shows that a maximum temperature of 100°C was achieved at an applied voltage of 5 volts. The output temperature exhibited a nonlinear relationship with applied voltage. The measured power essentially tracks the temperature profile and the measured input power is essentially indistinguishable from the calculated power except at applied voltages above 4V, with the largest difference being at 5V. The estimated percentage difference in resistance at the maximum operating temperature and room temperature was 11.41%.



(a)

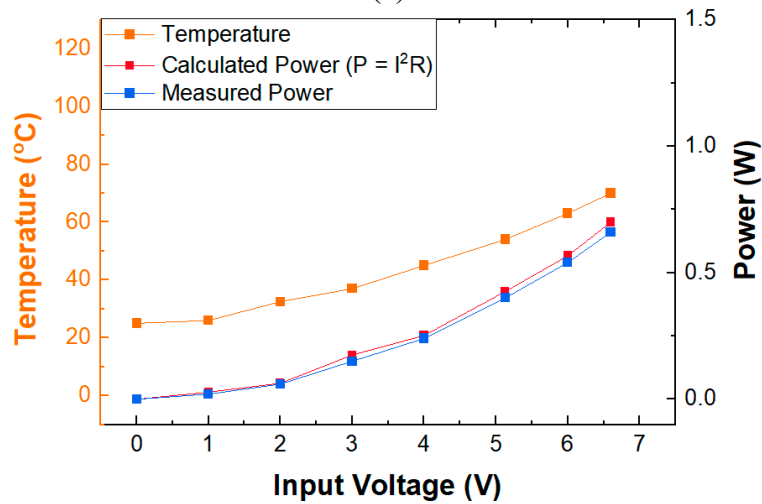
Print Pass	Resistance (Ω)
1	27k
2	1.45k
3	70

(b)

Figure 3-16: (a) An as-printed double spiral microheater printed on a glass substrate. (b) Measured resistance versus print passes for this microheater.



(a)



(b)

Figure 3-17: (a) Infrared image of a double spiral heater at 5V (54.1 °C). (b) Plot of temperature and power versus input voltage.



(a)

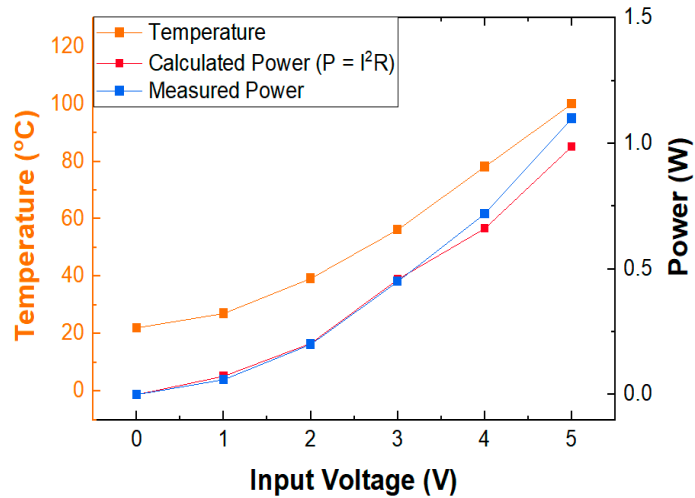
Print Pass	Resistance (Ω)
1	22.6k
2	1.05k
3	96.7
4	49.5
5	30.5
6	25.6
7	23.4
8	21.3
9	20.4

(b)

Figure 3-18: (a) Three-turn serpentine sample on a Kapton substrate. (b) Measured resistance versus print passes.



(a)

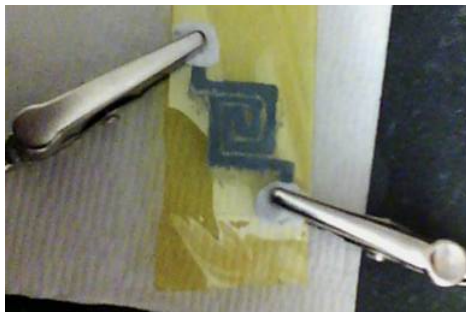


(b)

Figure 3-19: (a) Infrared image of a three-turn serpentine sample on Kapton substrate at 4V (78.1 °C). (b) Plot of temperature and power versus input voltage.

3.4.4 Stability Testing of Zn Microheaters

A 60-minute stability test was performed on the spiral microheater shown in Figure 3-20. After acetic acid treatment, the resistance of the device, which was printed on a Kapton substrate, dropped from over 1 k Ω to $\sim 25\Omega$. To achieve a constant operating temperature of 45 °C for the duration of the test, 2.5V_{DC} was applied across the sample and held constant for 60 minutes. Temperature measurements from infrared images and the microheater resistance were recorded at intervals of 1, 15, 30, 45 and 60 minutes, as shown in Figure 3-21c. The plot shows that the resistance slightly increased from 25 Ω to 30 Ω in the first 15 minutes of the test but remained stable thereafter. The increase in resistance is due to oxidation associated with operating the device at 45°C under ambient atmospheric conditions. After the initial 15 minute “burn in” the resistance remained constant for the remaining 45 minutes. This likely indicates cessation of the oxidation reaction on the surface of the microheater, which is a diffusion-governed, temperature-dependent process.

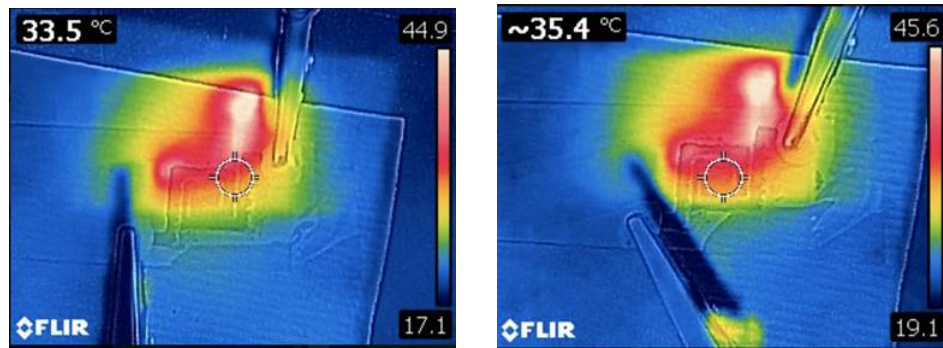


(a)

Print Pass	Resistance (Ω)
1	1.34k
2	~ 25

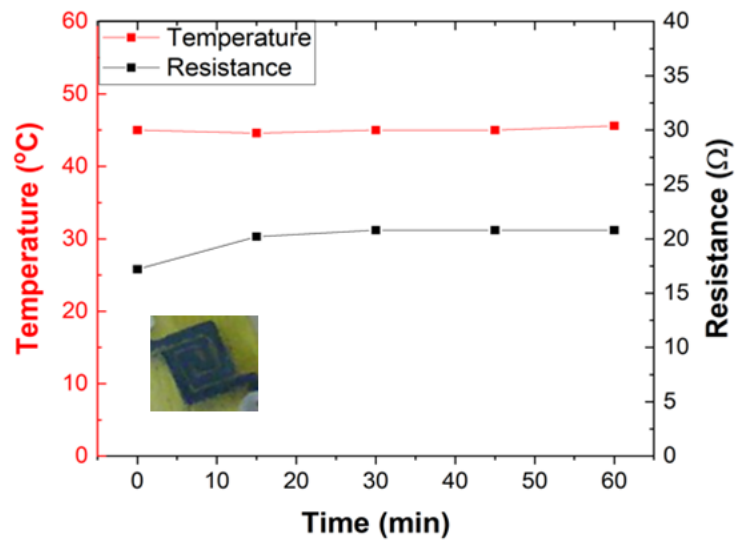
(b)

Figure 3-20: (a) The spiral serpentine sample on Kapton substrate used in the stability test. (b) Resistance for each print pass associated with the microheater.



(a)

(b)



(c)

Figure 3-21: (a) Infrared image at 1 minute (44.9°C). (b) Infrared image at 60 minutes (45.6°C). (c) Plot of temperature and resistance versus time.

3.4.5 Analysis and Discussion

The testing data presented in Figures 3-15, 3-17 and 3-19 show that Zn-based microheaters with output temperatures in the 100°C range can be fabricated by screen printing and RIJ printing based electrochemical sintering. As is typical for conventional microheaters, the maximum output temperature depends on heater dimensions and design. The minimum resistance achieved using the RIJ printing process (~20 to 70 Ω) was sufficient to fabricate microheaters with input voltages < 7V and input powers < 1.25W, which compare favorably to the state-of-the-art printed microheaters with comparable voltage and temperature characteristics. The measured input power is roughly proportional to the square of the input voltage, which is expected for a resistor-based heater. The measured output temperature roughly tracks the profile of the input power, which indicates that the generation of heat is a major energy loss mechanism in these structures. All microheater designs exhibit these behaviors.

With respect to instantaneous, dynamic microheater stability, comparisons between measured input power and calculated power indicate that the resistance of the microheaters is stable upon heating across the entire range of output temperatures. Extended, fixed temperature testing at a temperature near the midpoint of the output temperature range shows that the resistance of the structures is also stable. To the extent that electrical resistance is related to microstructure, these experiments suggest that the microstructure of screen-printed Zn after electrochemical sintering using RIJ printing is thermally stable in the short term, even under modest heating. These

investigations do not, however, shed light on the stability of the Zn structures in the long term.

3.5 Development of Zn-based RC Filters

3.5.1 Introduction

The direct-write capability of an inkjet printer when used to dispense a deoxidation agent enables the creation of planar metallic structures of a single material that exhibit significantly different electrical resistance depending on location. Hence printable circuits comprised of resistors and conductors of the same material and consisting of a single layer can potentially be fabricated using this method. This is a significant and potentially radical departure from conventional circuit fabrication that relies on different materials for the resistive and conductive elements and thus incorporates numerous material interfaces. Each of these interfaces adds a contact resistance to the circuit. To evaluate the potential of this RIJ printing method to create planar circuits comprised of both resistive and conductive components of a single material, this dissertation explores the fabrication of Resistor-Capacitor (RC) filters comprised of a single Zn layer using the RIJ-enabled selective deoxidation method to form both the resistor and capacitor. RC filters are an integral part of sensing and signal processing systems and recent advances in printed electronics has led to the development of printed RC filters on flexible substrates such as polyimide, PET, paper and textiles.

Table 3-4 summarizes recent advancements in fabricating inkjet-printed RC filters on flexible substrates by inkjet printing and Table 3-5 summarizes flexible RC filters fabricated by other methods. One of the main limitations of the state-of-the-art inkjet-printed, planar RC filters is that setting the cutoff frequency is not easily achievable because the resistor and capacitor structures must both be thermally annealed under significantly different conditions to achieve the desired level of conductivity in each structure, making it virtually impossible to fabricate the two components in a single layer. The RC filter designs described in Table 3-5 are inherently nonplanar.

Table 3-4: A Summary of Inkjet Printed RC Filters

	Resistor and Electrode Material	Substrate Material	Sintering Method	Capacitor Insulating Material	Cut-off Freq	Notes	Device Geometry
(Chen, Cui et al. 2003)	PEDOT:PSS (Conductive Polymer)	Transparency sheet	50 °C for 2 min (to completely dry)	PVPh Polyvinyl phenol	1 kHz (simulated)	Freq response was simulated. RC filter was tested as an integrator	Non-planar
(Li, Torah et al. 2012)	Silver Ink	65/35 polyester cotton textile	Silver ink: 150 °C for 10 min Dielectric ink: UV chamber at 160 nm wavelength for 100s	PVP	N/A	Objective was to design all inkjet capacitor, but this can be used as an RC filter	Non-planar
(Sinar and Knopf 2018)	Graphene-carboxymethyl cellulose (G-CMC)	Polyimide	Argon gas at 320°C for 30 min to decompose CMC	Silicone and polyimide	10 kHz Measured using oscilloscope		Planar
(Cao, Jochem et al. 2018)	PEDOT:PSS (resistor) Silver ink (electrodes)	PET	Silver ink: 100 °C in air for 3 min PEDOT-PSS: 100 °C air for 10 min	PEDOT:PSS	477 Hz (R=800 kΩ) 4.3 kHz (R=90 kΩ) 27 kHz (R=12 kΩ) C = 500 pF (fixed)	Resistance of pedot:pss polymer was varied using two different types of pedot mixture solutions: PH1000 (highly conductive) and AI408s (highly resistive)	Non-planar

Table 3-5: A Summary of Other Mechanically Flexible RC Filters

	<i>Resistor and electrode Material</i>	<i>Substrate material</i>	<i>Deposition method</i>	<i>Curing method</i>	<i>Capacitor Insulating material</i>	<i>Cut-off Freq</i>	<i>Device Geometry</i>
(Wang, Cui et al. 2020)	Graphene	Polyimide	Laser induced graphene (2.25W, 1.2mm depth) RC filter was then sealed with PDMS Silver paste as pads	Silver paste cured at 90 °C for 30min PDMS cured 80°C for 25min	PDMS	1.7 MHz R=580Ω C=168 pF	Planar
(Zulfiqar, Alam et al. 2021)	Graphite pencil (resistor) Copper tape (capacitor)	Letter size Paper	Pencil flaking	None	Aluminum foil	15- 190 kHz (corner frequency tuned by varying pencil flake)	Non-planar

3.5.2 Design and Fabrication of Zn-based RC Filters

Figure 3-22 is a photograph of a screen-printed Zn RC filter on a kraft paper substrate. The pad dimensions for this device are 2.5 mm x 2.5 mm. The total length of the resistor section is nominally 43 mm. The 9-finger capacitor comprises an area of 9 mm x 8 mm inclusive of the interdigitated electrodes. The electrode gap is 0.5 mm. The width of the resistor and connectors are 1 mm while the electrode finger width for the capacitor is 0.5 mm.

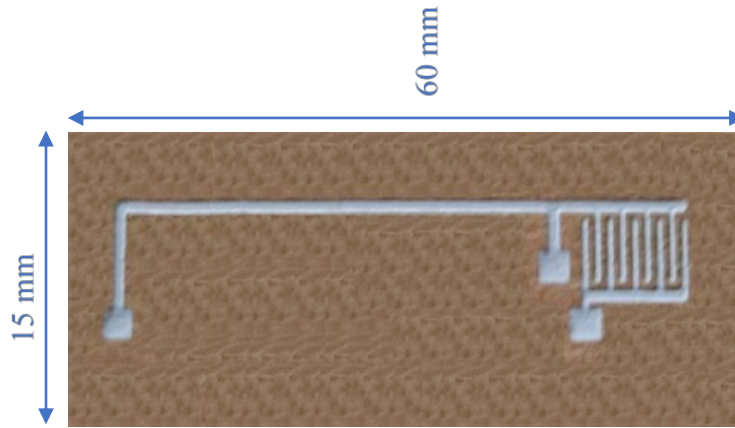


Figure 3-22: Photograph of a Zn RC filter printed on kraft paper.

Figure 3-23 illustrates the general approach used to fabricate the RC filters. The process involves screen printing the entire resistor-capacitor structure in one Zn layer followed by selective acetic acid exposure of the resistor and capacitor structures using an inkjet printer. The first step involves screen printing to form the entire RC structure out of a single printed layer. Next, the capacitor is exposed to acetic acid using the appropriate drop spacing and print passes that yield minimum resistivity, specifically, a drop spacing of $15\ \mu\text{m}$ and 2 print passes. Following capacitor fabrication, a high resistivity resistor was formed by dispensing acetic acid on the resistor using a drop spacing of $35\ \mu\text{m}$ and a predetermined number of print passes depending on the desired resistance of the resistor. Bode magnitude and phase measurements were then performed to evaluate the frequency response of the device. Subsequent RC filter devices were then fabricated by simply exposing the resistor to additional amounts of acetic acid using the inkjet printer. In this manner, a series of RC filter devices that differ only by the resistance of the resistor could be fabricated from a single screen

printed structure thereby enabling a direct comparison of device performance while eliminating the effects of geometric variation associated with screen printing individual devices.

The corner frequency (f_c) of a low-pass filter is calculated as:

$$f_c = \frac{1}{2\pi RC} \quad (12)$$

where R is the resistance and C is the capacitance of the filter device. Experimentally, the corner frequencies of each RC filter was determined from the Bode plots by assessing the frequency at which the magnitude drops by 3 dB. In this dissertation a total of five RC filter sets were fabricated with each set consisting of six individual RC filter devices that share a common capacitor but incorporate distinctly different resistors realized by the number of print passes used to fabricate them.

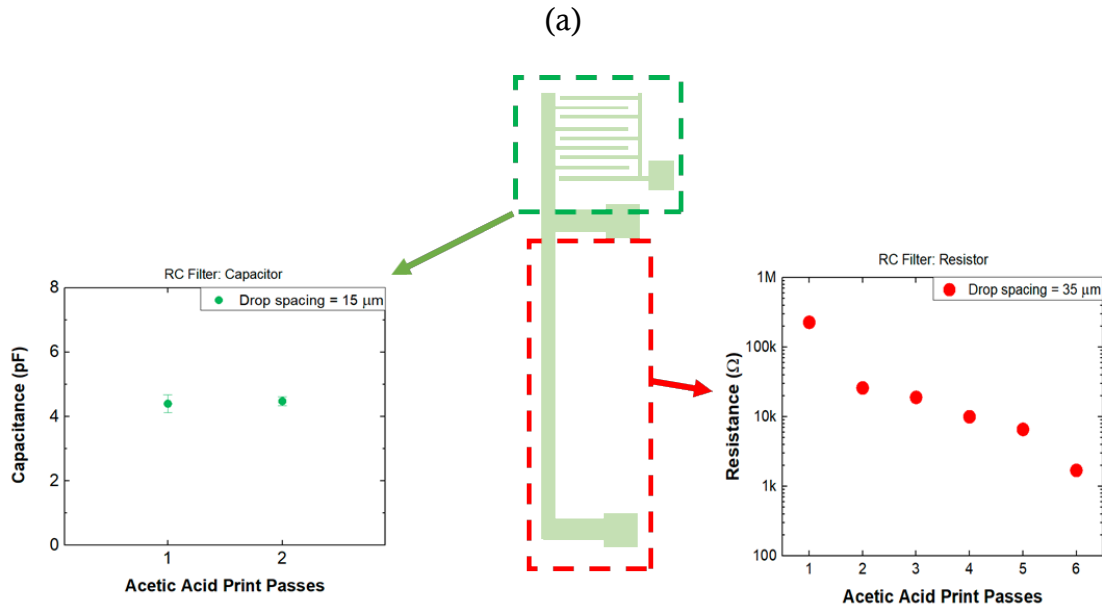


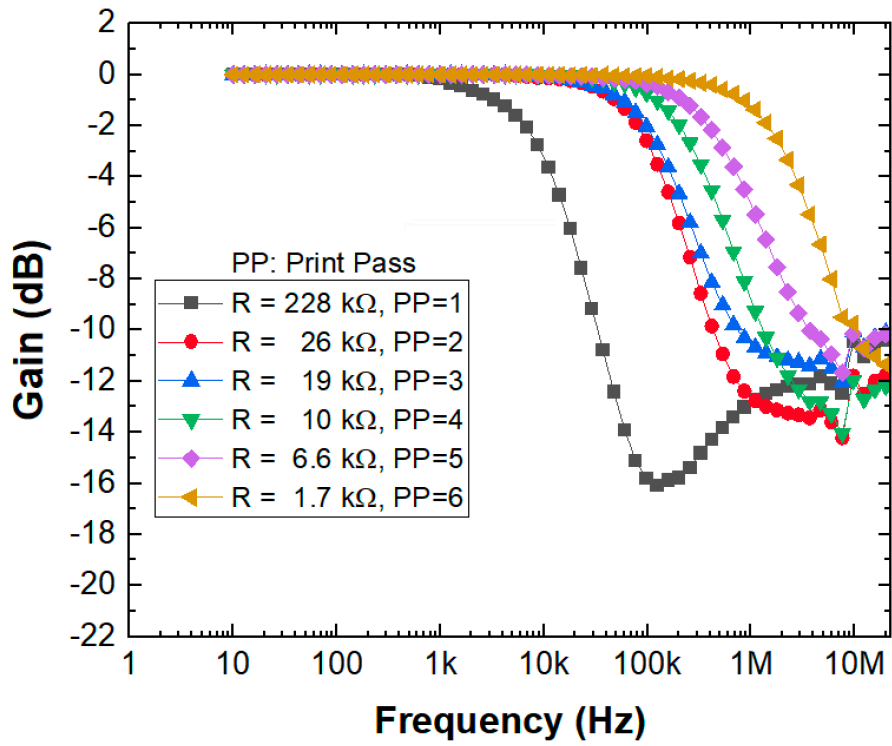
Figure 3-23: Pictorial representation of the RC filter fabrication process: (a) Screen printing of the RC filter (b) Exposure of the capacitor to acetic acid using 2 print passes at a drop spacing of 15 μm (c) Exposure of the resistor to acetic acid using 1 to 6 print passes at a drop spacing of 35 μm .

3.5.3 Frequency Response of Zn-based RC Filters

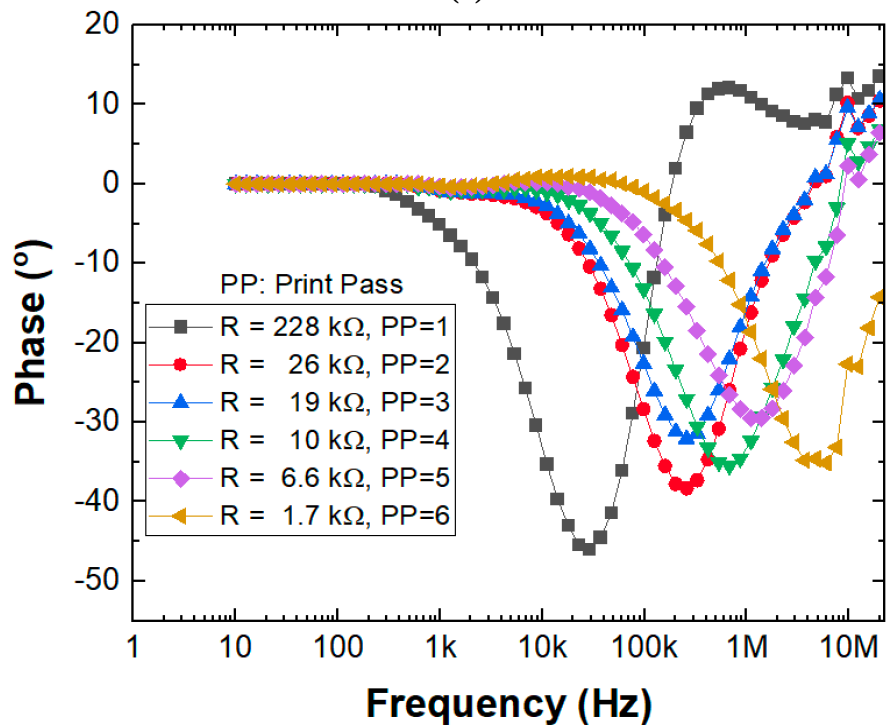
The frequency response of the RC filters after acetic acid exposure was assessed using a Keysight InfiniiVision MSOX3024 oscilloscope. Figure 3-24a and 3-24b present a set of measured Bode magnitude and phase plots for a series of RC filter devices from a single printed structure. For this particular set of measurements, the capacitor was fabricated using a drop spacing of 15 μm and 2 print passes while the resistors were fabricated using a drop spacing of 35 μm and a single print pass per resistor for a total of 6 print passes, thus yielding 6 distinct resistors for the single capacitor.

Bode magnitude and phase plots were generated for each RC device after fabricating the associated resistor. As such, subsequent resistors leveraged the baseline resistivity of the resistor that was realized by the previous acetic acid exposure.

Each of the magnitude plots in Figure 3-24a exhibits the characteristic of low pass filtering behavior expected of these devices. Each of the magnitude plots showed an exponential roll-off of ~ 12 dB/decade. The plot for the device with the $228 \text{ k}\Omega$ resistor, which had the lowest f_c at ~ 7 kHz, shows a modest increase in the magnitude for frequencies beyond 100 kHz, which ultimately plateaus at 1 MHz. Such behavior is possibly due to a parasitic inductance induced by the interdigitated electrode gaps which has been observed in graphene-based RC filters (Wang, Cui et al. 2020). Thus, the RC filter exhibits weak RLC filter-like characteristics with a resonance frequency at ~ 202 kHz when $R = 228 \text{ k}\Omega$ (after 1st print pass). The magnitude curve shows a trough at ~ 202 kHz, corresponding to a 0° phase in the phase response.



(a)



(b)

Figure 3-24: Bode plots of the RC Low Pass Filter: (a) Magnitude response (b) Phase response.

Each of the phase plots in Figure 3-24b exhibit characteristics expected of low pass filters. Each of the phase plots shows an increasingly negative phase angle when the frequency begins to exceed the corner frequency. For the RC filter incorporating the 228 k Ω resistor ($f_c = 7$ kHz), the phase angle drops to a minimum of nearly -46° at ~29 kHz. This indicates, in the time domain, the output voltage lags the input voltage by 46° at ~29 kHz. At $f_c = 7$ kHz, the phase angle is nearly -26°, which is slightly over half the phase angle at ~29 kHz. This is consistent with the stop band characteristics of a low pass filter. Beyond 29 kHz, the phase angle begins to rise, due to the parasitic inductance, until it reaches 0° at ~202 kHz, which is the resonance frequency associated with the RLC characteristics over high frequency ranges.

3.5.4 Transient Response of Zn-based RC Filters

To evaluate a representative RC filter as an integrator, the transient response of select devices was characterized by applying time-varying input signals with frequencies below and above the measured corner frequency of the device and evaluating the resulting output signal. These simple tests were performed using a function generator (TTi TG35 Function Generator) and an oscilloscope (Keysight InfiniiVision MSOX3024T Mixed Signal Oscilloscope). The input excitation signal consisted of a square wave, whereas the output waveform was the measured voltage across the capacitor. Square wave inputs represent the scenario of repeated on and off direct current inputs at a fixed frequency, and therefore enable the time constant of the RC filter circuit to be determined. Figure 3-25 presents the transient response for an RC filter with a corner frequency of ~130 kHz and a square wave input voltage

($V_{in, \text{amplitude}} = 1.375\text{V}$) at a frequency of 20 kHz. As can clearly be seen, when the frequency of the excitation signal was less than the measured corner frequency ($f < f_c$), the output signal is essentially a square wave in synchronization with the input. The time constant for this RC filter can be experimentally determined by estimating the time at which the signal reaches 63% of its final value, the estimated time constant for this device was $\sim 2 \mu\text{s}$. The calculated capacitance from such a time constant value is $\sim 100 \text{ pF}$. Because the pulse duration of the input square wave signal was larger than $5RC$ of the filter device ($25 \mu\text{s} > 5(2 \mu\text{s}) = 10 \mu\text{s}$), the capacitor was fully charged during this “on” time cycle and the output signal exhibits the square-wave like profile shown in Figure 3-25. The peak of the output voltage ($V_{\text{out peak}} = 1.14\text{V}$) is observed to be slightly lower than that of the input voltage ($V_{\text{in peak}} = 1.22\text{V}$). In other words, the gain ≈ 0.934 while it was expected to be close to unity. Such deviation can possibly be attributed to sampling resolution limitations of the oscilloscope device. Another possible reason might be the contribution of high frequency harmonics on the RC filter device

Figure 3-26 shows the output response for the same device when the frequency of the excitation signal was higher than the corner frequency ($f > f_c$). For this particular measurement, the input frequency was 220 kHz. Because the pulse width of the input square wave (both charging and discharging cycle) was smaller in this case ($2.5 \mu\text{s} < 5(2 \mu\text{s}) = 10 \mu\text{s}$), the capacitor was only partially charged during a single cycle, resulting in a triangular waveform at the output. The profile of the measured output in this case is characteristic of an RC integrator and is consistent with a typical first-order RC low pass filter.

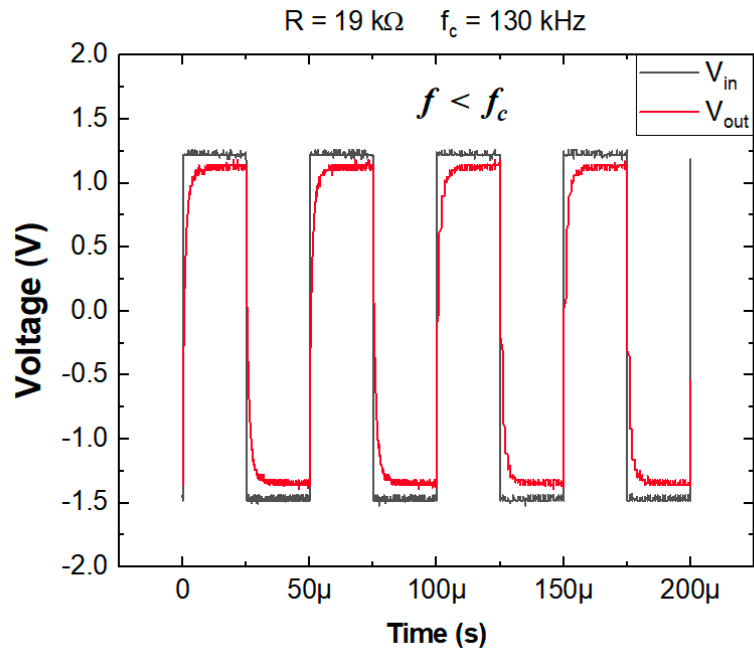


Figure 3-25: Transient response of a Zn-based RC filter with an input voltage (V_{in} , amplitude = 1.375V) at a frequency of ~20kHz, which is less than the corner frequency of the device ($f_c = 130 \text{ kHz}$).

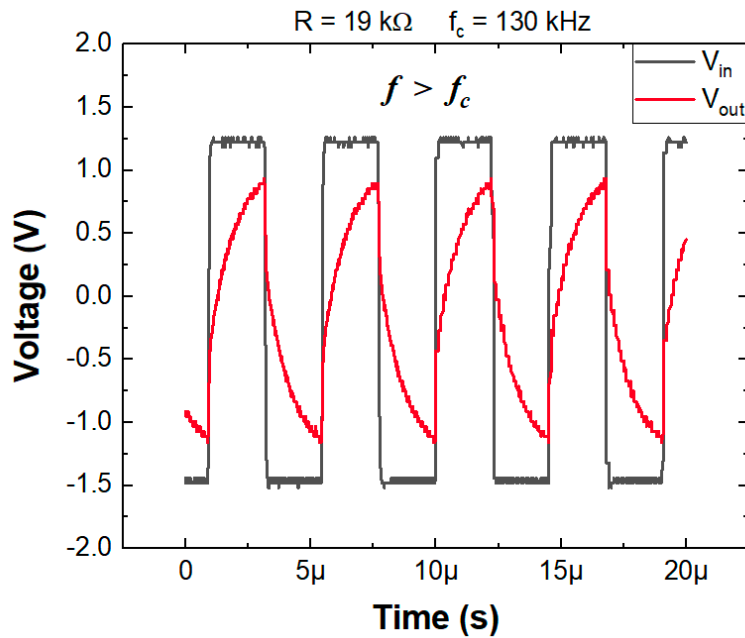


Figure 3-26: Transient response of a Zn-based RC filter with an input voltage at (V_{in} , amplitude = 1.375V) a frequency of 220 kHz, which is greater than the corner frequency of the device ($f_c = 130 \text{ kHz}$).

3.5.5 Analysis and Discussion

Figure 3-27 presents a plot of the measured corner frequency versus resistance for the device associated with the five RC devices whose Bode plots are presented in Figure 3-24. The corner frequency is observed to decrease from ~ 2 MHz to ~ 7 kHz as the resistance value of the resistor is increased from ~ 1.7 k Ω to ~ 228 k Ω by successive inkjet printing. The data exhibit a linear behavior in this log-log plot.

Figure 3-28 presents the measured f_c versus the reciprocal of the measured resistance (R^{-1}) for the data presented in Figure 3-27. The corner frequency increases in a linear fashion as R^{-1} increases from $\sim 4.39 \times 10^{-6}$ to $\sim 5.88 \times 10^{-4}$ Ω^{-1} . A fitted line ($R^2 = 0.9957$) has a slope of 3×10^9 Hz/ Ω , which using equation 12 indicates that the capacitance for the capacitor in this RC filter is ~ 53 pF. This value represents the total capacitance of the structure, which includes the capacitance of the interdigitated electrodes (IDE) as well as an unwanted parasitic capacitance. That a component of the total capacitance is comprised of a parasitic capacitance is not surprising for several reasons. First, the device does not incorporate an insulating capping layer to electrically isolate the resistor, capacitor and interconnects of which all three are made of Zn. Second, the devices incorporate a simple interconnect design to facilitate connections to both the resistor and capacitor including a resistor contact that is close to one set of capacitor electrodes. Third, the test setup was designed to facilitate quick connections between the device and the measurement instrumentation and thus was not designed to suppress parasitic capacitances. All of these could contribute to a relatively large parasitic capacitance. Independent measurements of the IDE-based capacitors indicate that the capacitance of the IDE structures is between 4 and 4.5 pF.

This suggests that the parasitic capacitance could be as high as ~ 49 pF. It was beyond the scope of this dissertation to explore and suppress the sources of the parasitic capacitance since the focus of this work was not on RC filter design, but on the RIJ process used to form the resistors. That being said, the strong linear fit of the data in Figure 3-28 indicates that the overall capacitance for the device is constant, and thus the presence of the parasitic capacitance does not affect the overall findings of this study.

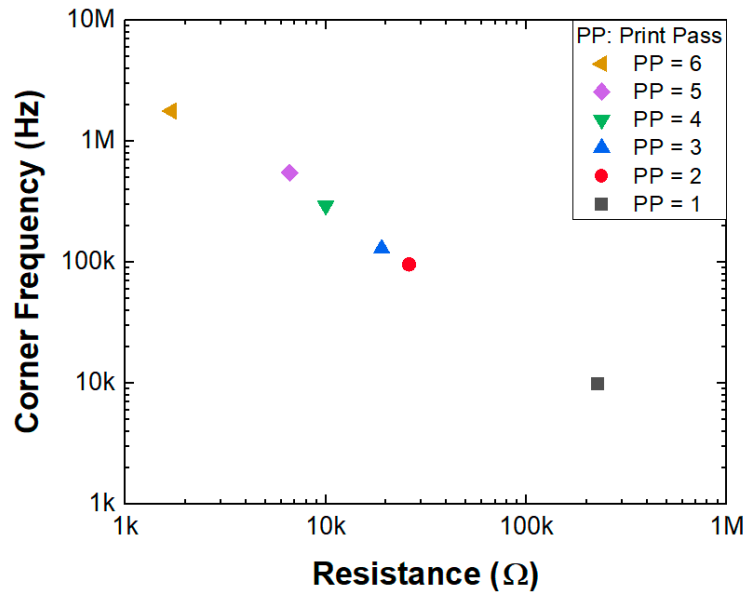


Figure 3-27: Measured corner frequency versus measured resistance obtained from the device characterized in Figure 3-24.

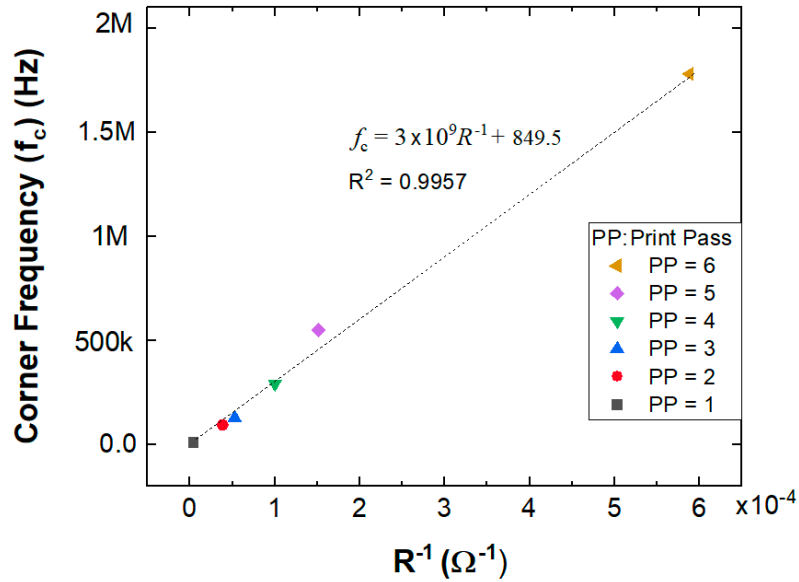


Figure 3-28: Measured corner frequency versus the reciprocal of the resistance (R^{-1}) obtained from Figure 3-25. The fitted line shows a linear relationship with squared-R, $R^2 = 0.9957$

Figure 3-29 summarizes the relationship between the average corner frequency with average resistance for the 5 RC filter sets developed in this dissertation. Consistent with the data presented in Figure 3-27, the data set aggregated across the five sets of RC devices exhibits a linear relationship between corner frequency and the resistance of the resistor in a log-log plot, which is also consistent with equation 12. This result is expected since a common device geometry and a common set of print passes were used to fabricate the five sets of RC devices. As such, Figure 3-29 is a representation of the repeatability of the fabrication process described in this dissertation.

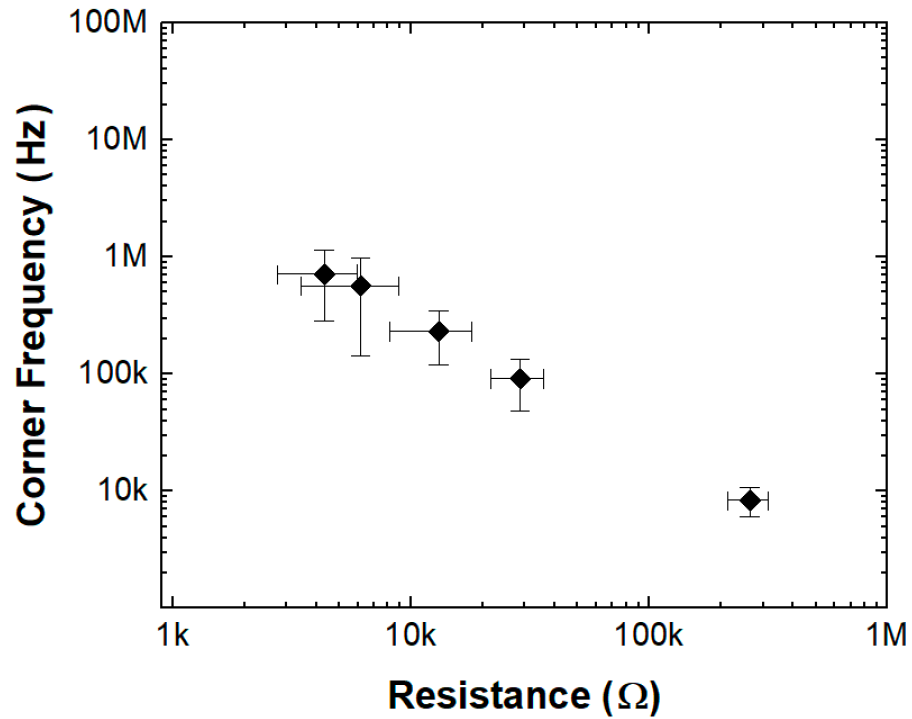


Figure 3-29: Measured average corner frequency versus average resistance of the Zn-based RC filter devices evaluated in this dissertation.

Figure 3-30 summarizes the relationships between the average corner frequency (f_c) the number of print passes used to fabricate the resistor for the five RC filter sets developed in this dissertation. The average f_c is observed to increase significantly from ~7 kHz to ~1 MHz as the number of print passes increases from 1 to 5. In contrast to the plots that describe the relationship between corner frequency and resistance, the behavior in this plot is nonlinear because the number of print passes are discrete values and thus Figure 3-30 is presented as a semilog plot. The data presented in Figure 3-30

shows that the corner frequency for these Zn based devices can be tuned by the number of print passes used to form the resistor.

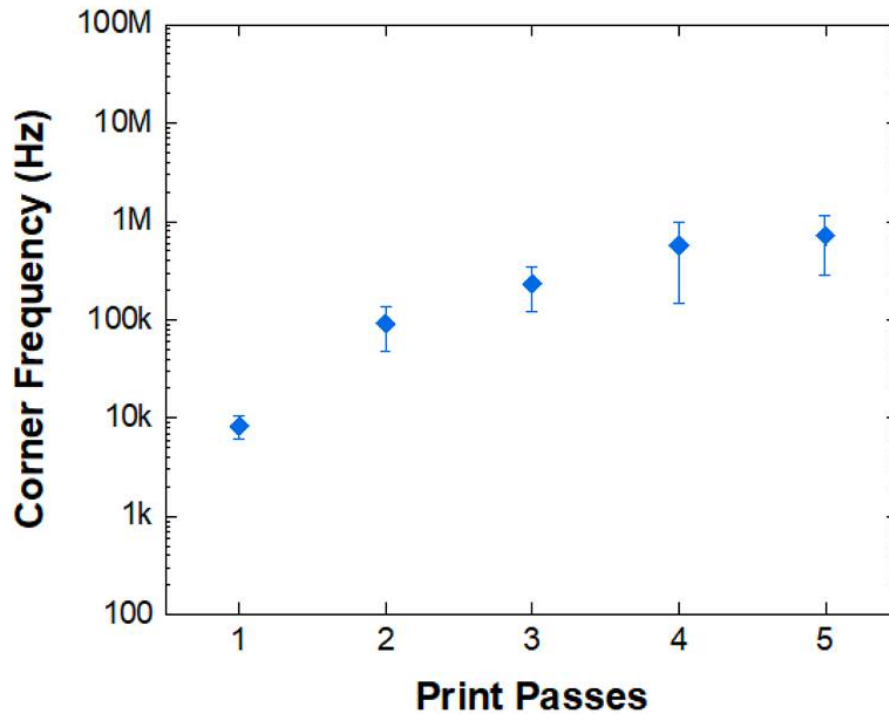


Figure 3-30: Average corner frequency versus number of print passes for the Zn-based RC filter devices developed in this dissertation.

3.6 Stability Testing of Zn-based Resistors

3.6.1 Experimental Details

As stated in Section 3.1, Zn is of interest for metallic structures in biodegradable microdevices because it is one of only a few metals that can be safely used in biodegradable circuits owing to its high degree of biocompatibility combined with its propensity to chemically degrade into inert components under normal environmental conditions. While much is known about the biodegradable properties of Zn structures prepared using conventional means, widespread adoption of the RIJ technique in

fabricating Zn-based microdevices requires knowledge about the stability of such structures under a wide range of relevant environmental conditions. In this dissertation, a first study to assess the stability of Zn-based resistors under ambient conditions was performed in order to provide a baseline for future work in this area.

To evaluate the stability of the Zn structures under ambient conditions, static resistance measurements were carried out on two sets of samples over a 30-day period. Each day, a simple two-point resistance measurement was performed on a series of linear resistors that were continuously exposed to room conditions. Silver epoxy was applied on the ends of each sample to ensure measurement consistency. Test samples consisted of 2 mm x 5 mm linear resistors that were screen printed using the process described previously. These samples were divided into two sets; the first set was exposed to acetic acid using a single print pass with a drop spacing of 10 μm (DS = 10 μm). The second set was exposed to acetic acid using a single print pass with a drop spacing of 5 μm (DS = 5 μm). Each set was comprised of 5 samples. Figures 3-31 and 3-32 present plots of measured resistance versus measurement day for the 30-day stability test.

Figure 3-31 presents the results of the stability test for the set prepared using a drop spacing of 10 μm . In general, the results were inconsistent. Sample #2 and #3 exhibited measurable resistances throughout the entire 30-day test period whereas Sample #1, #4 and #5 failed to register a measurable resistance before the end of the test period. The upper limit of the resistance meter was 40 M Ω . The resistance of Sample #2 and #3 increased from nearly 10 Ω on Day 1 to nearly 2k Ω after Day 27. Comparatively, the measured resistance of Sample #5, #1 and #4 increased much

faster, as their resistances rose by an order of magnitude in less than 15 days, and their resistances were too high to be measured by the multimeter after Day 8, 14 and 18, respectively.

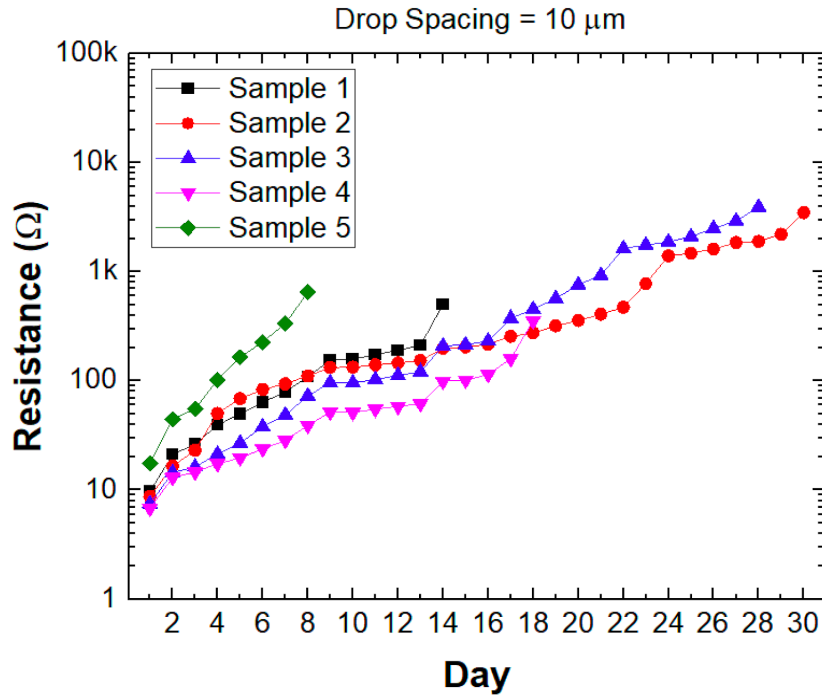


Figure 3-31: Resistance versus time for Zn samples treated using a single print pass with a drop spacing of $10 \mu\text{m}$.

Figure 3-32 presents the results of the stability test for the set prepared using a drop spacing of $5 \mu\text{m}$. In contrast to data presented in Figure 3-31, the measured resistances, for the sample set prepared using a drop spacing of $5 \mu\text{m}$ set, were much more consistent in that all five of the test samples exhibited a measurable resistance throughout the 30-day test. As a group, the resistance of most samples rose from $\sim 3\Omega$ on Day 1 to multiples of 100Ω on Day 30, which is nominally one order of magnitude over the 30-day period. The reason for the stepwise increase in resistance observed for samples 1-4 on Day 28 cannot be determined from these data.

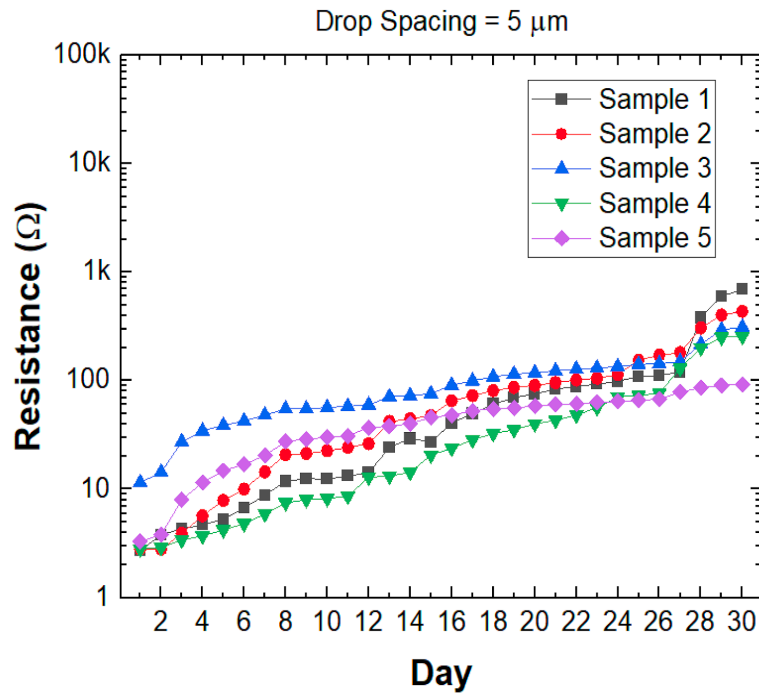


Figure 3-32: Resistance versus time for Zn samples treated using a single print pass with a drop spacing of 5 μm .

3.6.2 Analysis and Discussion

The 30-day stability test results suggest that the drop spacing used in the RIJ process significantly influences the stability of the electrochemically sintered Zn particles during long-term exposure under ambient conditions. During the RIJ process, the native oxide passivation layer on the surface of the Zn particles was dissolved by the aqueous acetic acid. This dissolution promoted, at the Zn-H₂O interface, a self-exchange between Zn and Zn²⁺ at the particle interfaces, which welded adjacent Zn particles. Upon evaporation of the solvent, a new passivation layer that encapsulates the newly welded particles is formed. According to Chen, et al., the interaction of Zn with the surrounding atmosphere occurs in an interfacial system, involving reaction kinetics (Chen, Schneider et al. 2012). These reaction kinetics are affected by

environmental conditions including relative humidity, temperature and contamination (Chen, Schneider et al. 2012). The surface passivation layer formed on the Zn particles is normally a few nanometers thick and is electrically insulating. The thickness of this layer is dependent upon the exposure time as well as the surrounding temperature and humidity (Lee, Kim et al. 2017). The data presented in Figures 3-31 and 3-32 show that a small drop spacing produces more stable Zn structures. The resistance measurements in Figures 3-31, 3-32 and 3-4, as well as the sheet resistance measurements in Figure 3-5 indicate that a small drop spacing produces a higher density of cold welding between Zn particles than a large drop spacing. Moreover, the contact regions of these cold welds are likely to be larger for small drop spacing due to the relative abundance of the liquid deoxidation agent per unit volume during the RIJ process. Consequently, the electrical stability of these structures under ambient conditions is higher than for Zn structures formed using a large drop spacing which produce welded particles that have smaller contact regions and at a lower density.

These findings indicate that resistor-based Zn devices require protection from reoxidation after RIJ treatment by encapsulating the structures in a protective coating. For many applications, this could be a thin film of Parylene, which is a biocompatible polymer that has excellent moisture and gas barrier properties, electrically insulating and is a common packaging material in biomedical microdevices. Alternatively, for biodegradable devices, Sui, et. al showed that a biodegradable wax could be used to protect electrochemically sintered Zn structures from oxidation (Sui, Radwan et al. 2022).

Chapter 4

Conclusions

This dissertation focuses on the development of two distinct approaches to advance the use of inkjet printing as a platform additive manufacturing technique for printed sensors that incorporate resistor-based sensing elements. The first approach centered on the development of inkjet-printed, resistor-based devices by developing novel particle-free inks designed specifically for moderate to high resistance structures based on AgNO_3 and three chemically different forms of ethylene glycol as the ink solvent. Strain gauges and temperature sensors were fabricated to evaluate these inks for their utility in producing resistor-based sensors as well as to explore the relationships between ink solvent, microstructure and device performance. From a technology perspective, this project was successful in producing inkjet-printed strain gauges and temperature sensors with performance characteristics that compete with comparable sensors made from Ag nanoparticle inks but at significantly lower substrate temperatures ($< 140\text{ }^\circ\text{C}$) during fabrication. The highest GF was 11.5 and

the highest TCR was $1.75 \times 10^{-3} \text{ }^\circ\text{C}^{-1}$. From a scientific perspective, this project elucidated the relationships that link process parameters and ink composition with microstructure and sensor performance.

The second approach sought to advance the development of a printing technology for the Zn-based systems, focusing on the development of inkjet printing to perform selective chemical deoxidation of the native zinc oxide on Zn microparticles, and the subsequent formation of connected Zn structures by electrochemical sintering. This part of the dissertation specifically focused on the formation of Zn structures by precision dispensing of acetic acid on screen-printed Zn structures and explored the relationships between key printing parameters (drop spacing and number of print passes) and the electrical resistivity of the resulting Zn structures. From a technology perspective, this project was successful in demonstrating that an inkjet printer could dispense acetic acid at sufficiently small volumes to enable precision control of electrical resistance during oxidation and electrochemical sintering. Zn microheaters with performance characteristics on par with conventional printed microheaters were successfully developed. The RIJ-based electrochemical sintering process enabled the fabrication of a planar RC filter in which all components, including the resistor, capacitor, interconnects and contact pads, were fabricated from the same screen-printed layer. To the best of our knowledge, this is the first time such a device has been fabricated. From a scientific perspective, this dissertation explored the connections between electrical resistance and microstructure in screen-printed Zn after deoxidation and electrochemical sintering using extremely

low volumes of the chemical agent. The following section summarizes the major achievements and major findings of this dissertation.

The major achievements of this dissertation in areas related to inkjet printing technology include:

- Successful printing of Ag structures using a particle-free AgNO₃/EG ink with sheet resistances that vary over four orders of magnitude and in a range that is well suited for resistor-based devices such as strain gauges and temperature sensors.
- Successful development of inkjet-printed Ag strain gauges with gauge factors that are dependent on plasma exposure time and the type of glycol solvent in the ink. This dissertation provides a method to “tune” the gauge factor in printed Ag strain gauges using a conveniently controllable plasma process parameter in conjunction with ink composition. Such ability is difficult to achieve using Ag nanoparticle-based inks.
- The successful development of inkjet-printed Ag temperature sensors with TCR values that are dependent on the type of glycol solvent in the ink. This dissertation provides a method to “tune” the TCR in Ag strain gauges using ink composition. Such ability is challenging to achieve using Ag nanoparticle-based inks.
- The development of reactive inkjet (RIJ) printing for acetic acid-based electrochemical sintering of screen-printed Zn devices in order to control

electrical resistance during the sintering step. Sheet resistances span over five orders of magnitude depending on the drop spacing and number of print passes used to dispense the acetic acid. The range of achievable sheet resistances enabled the fabrication of both resistive and conductive structures in screen-printed Zn. The RIJ printing process offers a level of volume and spatial control unachievable using other methods of electrochemical sintering, namely drop casting or dip coating.

- Successful development of a biodegradable, low-power Zn microheater with voltage, power and output temperature characteristics that are comparable to similar printed microheaters made from other materials. These microheaters are made by screen printing and RIJ printing enabled electrochemical sintering and thus are fabricated at room temperature, making them compatible with temperature sensitive substrates.
- Successful development of a “first-of-a-kind”, planar printed RC filter with the resistor, capacitor, interconnects and contact pads all fabricated from a single printed layer. In this particular implementation, the RC filter consisted of a screen-printed Zn structure that was converted into an RC filter device by selective electrochemical sintering of the various device elements. All processing steps were performed at room temperature, enabling the fabrication of the RC filter on paper substrates. This process is easily extended to other devices that consist of resistive and conductive elements.

The major findings of this dissertation include:

- The principal characteristics associated with AgNO₃/EG inks that were formulated to achieve structures with low electrical resistance (Sui, Hess-Dunning et al. 2020, Sui, Hess-Dunning et al. 2022) translate directly to ink formulations with a three-fold lower concentration of AgNO₃. Specifically:
 1. For all three ethylene glycol solvents used in the AgNO₃/EG inks, the sheet resistance of the plasma converted Ag structures decreased roughly exponentially with increasing plasma exposure time. The minimum sheet resistance value for each ink type converged to a value of $\sim 10^1 \Omega/\square$ after plasma exposure for 30 minutes, which was still an order of magnitude higher than for the highly concentrated inks (1.5M AgNO₃). The significant change in sheet resistance indicates that the resistance of structures printed using these inks is tunable using plasma exposure time as a control parameter.
 2. The sheet resistance exhibits a strong dependence on the solvent used in the ink. Structures printed using the triEG ink exhibit the highest sheet resistance with respect to plasma exposure time, followed by the diEG ink and then by the monoEG ink. At 30 minutes of plasma exposure, the sheet resistance values associated with all three ink solvents roughly converged. These findings indicate that the resistance of structures printed using these inks is tunable using the type of ink solvent as a control parameter.

3. The microstructure of the printed structures after plasma treatment depends strongly on the vapor pressure of the ink solvent. The triEG ink produces the most porous structures while monoEG ink the densest structures, with moderate porosity produced using the diEG ink. Thus, the connections between the vapor pressure of the ink solvent and porosity of the plasma treated structures for inks with high AgNO_3 concentrations reported elsewhere (Sui, 2019, Sui, Hess-Dunning et al. 2020, Sui, Hess-Dunning et al. 2022) are also observed in inks with low AgNO_3 concentrations. As such, the model that describes the formation on Ag structures from the AgNO_3/EG inks during plasma treatment also translates to low concentration inks.
- The gauge factor of Ag strain gauges fabricated using the AgNO_3/EG inks depends on the microstructure of the Ag resistors which, in turn, depends on the vapor pressure of the ink solvent. The highest gauge factors were measured from strain gauges made using the triEG ink, which has the lowest vapor pressure of the three forms of ethylene glycol. These resistors had the highest porosity. As the vapor pressure of the ink solvent increases, the microstructure of the resistors is less porous and the gauge factor decreases.
 - The TCR of Ag temperature sensors fabricated using the AgNO_3/EG inks depends on the microstructure of the Ag resistors which, in turn, depends on the vapor pressure of the ink solvent. Unlike the strain gauges, the highest TCR values were measured from temperature sensors made using the monoEG ink, which has the highest vapor pressure of the three forms of ethylene glycol.

These resistors had the lowest porosity. As the vapor pressure of the ink solvent decreases, the microstructure of the resistors is more porous and the TCR decreases.

- Electrochemical sintering using an inkjet printer to dispense pico-liter droplets of acetic acid is an effective means to control the electrical resistance of screen-printed Zn structures. By proper selection of drop spacing and number of print passes, the sheet resistance of screen-printed Zn structures RIJ-based electrochemical sintering ranged 2×10^5 to $0.5 \Omega/\square$, depending on drop spacing and number of print passes. This broad range enables the resistance of screen-printed Zn structures to be “tuned” using the RIJ printing process to dispense acetic acid.
- Electrochemical sintering of Zn microparticles using the RIJ printing process does not result in a change in the crystal orientation or average size of the Zn particles. Rather, as with the drop casting method, the acetic acid dissolves the native oxide that encases the Zn particles and facilitates cold welding of adjacent Zn particles, a process that becomes more prevalent with an increasing number of print passes. These observations are consistent with the sheet resistance measurements, indicating that the conduction pathways in the sintered Zn structures are primarily through the fused Zn particles.
- As a result of the high degree of volume and dimensional control associated with inkjet printing, planar Zn structures that incorporate both resistors and conductors can be fabricated from a single screen-printed layer using RIJ-based

electrochemical sintering. The inkjet printer enables the resistors to be fabricated using one set of printing parameters while the conductors another set. The RIJ process avoids damage to the Zn structures associated with overexposure to acetic acid.

- Zn-based RC circuits fabricated using RIJ-based electrochemical sintering exhibit the frequency response and transient response expected of a low pass filter. Due to the wide range of resistances that are achievable using the RIJ-based electrochemical sintering, the range of corner frequencies that were realized in a RC filter of fixed dimensions was ~ 7 kHz to ~ 1 MHz. The RIJ-based deoxidation and electrochemical sintering process is compatible with any substrate that is tolerant to acetic acid, including paper substrates.

Appendix 1

Figure A-1 presents temperature versus plasma exposure time for substrates subjected to the low-pressure Ar plasma reduction step detailed in Chapter 2 of this dissertation. The temperature data in this figure are temperature measurements of the substrate holder while under plasma exposure. The data in this figure is used to estimate the substrate temperature for plasma treatment at 150 W and 300 W.

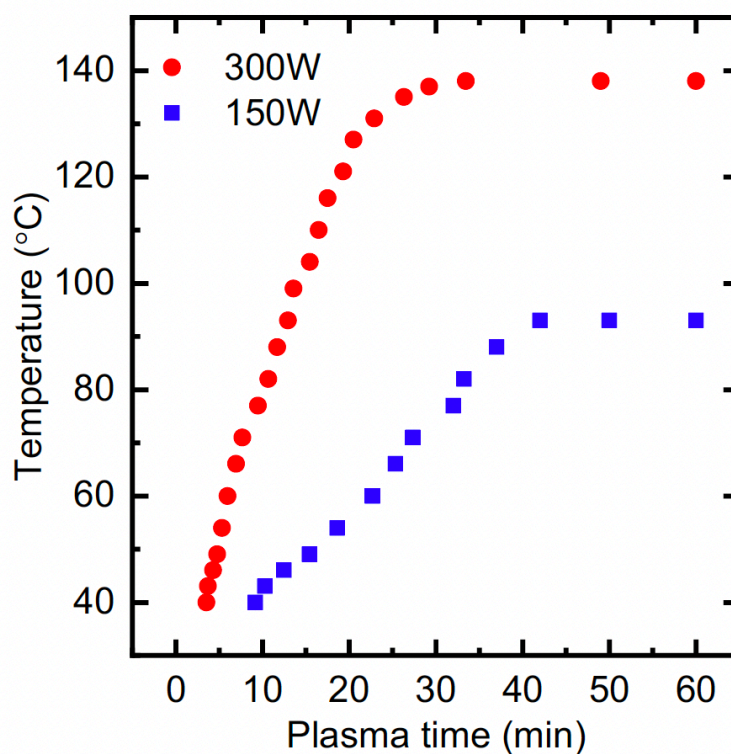


Figure A-1: Measured temperature of the plasma chamber electrodes as a function of argon plasma exposure time for RF powers of 150W and 300W (Sui, Dai et al. 2019). Copyright of John Wiley and Sons. Reproduced with Permission from John Wiley and Sons.

References

- Abu-Khalaf, J., L. Al-Ghussain, A. Nadi, R. Saraireh, A. Rabayah, S. Altarazi and A. a. Al-Halhouli (2019). "Optimization of geometry parameters of inkjet-printed silver nanoparticle traces on pdms substrates using response surface methodology." *Materials* **12**(20): 3329.
- Alhendi, M., R. S. Sivasubramony, D. L. Weerawarne, J. Iannotti, P. Borgesen and M. D. Poliks (2020). "Assessing Current-Carrying Capacity of Aerosol Jet Printed Conductors." *Advanced Engineering Materials* **22**(11): 2000520. 2001438-2001656.
- Aliane, A., V. Fischer, M. Galliari, L. Tournon, R. Gwoziecki, C. Serbutoviez, I. Chartier and R. Coppard (2014). "Enhanced printed temperature sensors on flexible substrate." *Microelectronics Journal* **45**(12): 1621-1626. 0026-2692.
- Annese, V. F., D. De Venuto, C. Martin and D. R. S. Cumming (2014). Biodegradable pressure sensor for health-care, In *2014 21st IEEE International Conference on Electronics, Circuits and Systems (ICECS)* (pp. 598-601). IEEE
- Barmpakos, D., A. Segkos, C. Tsamis and G. Kaltsas (2018). A disposable inkjet-printed humidity and temperature sensor fabricated on paper. *Multidisciplinary Digital Publishing Institute Proceedings*, **2**(13), p.977.
- Beckwith, T. G. and D. Roy (1982). "Marangoni. Mechanical Measurements." *Reading: Addison-Wesley* **353**.
- Bermel, A. D., and Bugner, D. E. (1999). Particle size effects in pigmented ink jet inks. *Journal of imaging science and technology*, **43**(4), 320-324.
- Borghetti, M., M. Serpelloni, E. Sardini and S. Pandini (2016). "Mechanical behavior of strain sensors based on PEDOT: PSS and silver nanoparticles inks deposited on polymer substrate by inkjet printing." *Sensors and Actuators A: Physical* **243**(71-80).

Briand, D., F. Molina-Lopez, A. V. Quintero, C. Ataman, J. Courbat and N. F. de Rooij (2011). "Why going towards plastic and flexible sensors?" *Procedia Engineering* **25**(8-15): 1877-7058.

Briand, D., A. Oprea, J. Courbat and N. Bârsan (2011). "Making environmental sensors on plastic foil." *Materials Today* **14**(9): 416-423. 1369-7021.

Callister, W. D. and D. G. Rethwisch (2011). *Materials Science and Engineering*, John Wiley & sons New York.

Cao, M., K. Jochem, W. J. Hyun, L. F. Francis and C. D. Frisbie (2018). "Self-aligned inkjet printing of resistors and low-pass resistor–capacitor filters on roll-to-roll imprinted plastics with resistances ranging from 10 to 106 Ω ." *Flexible and Printed Electronics* **3**(4): 045003. 042058-048585.

Chang, J.-K., H. Fang, C. A. Bower, E. Song, X. Yu and J. A. Rogers (2017). "Materials and processing approaches for foundry-compatible transient electronics." *Proceedings of the National Academy of Sciences* **114**(28): E5522-E5529. 0027-8424.

Chen, B., T. Cui, Y. Liu and K. Varahramyan (2003). "All-polymer RC filter circuits fabricated with inkjet printing technology." *Solid-State Electronics* **47**(5): 841-847. 0038-1101.

Chen, Q., J. Li and Y. Li (2015). "A review of plasma–liquid interactions for nanomaterial synthesis." *Journal of Physics D: Applied Physics* **48**(42): 424005. 420022-423727.

Chen, Y., P. Schneider and A. Erbe (2012). "Investigation of native oxide growth on zinc in different atmospheres by spectroscopic ellipsometry." *physica status solidi (a)* **209**(5): 846-853. 1862-6300.

Choi, Y., K. d. Seong and Y. Piao (2019). "Metal organic decomposition ink for printed electronics." *Advanced Materials Interfaces* **6**(20): 1901002. 1902196-1907350.

Courbat, J., Y. B. Kim, D. Briand and N. F. De Rooij (2011). Inkjet printing on paper for the realization of humidity and temperature sensors, *16th International Solid-State Sensors, Actuators and Microsystems Conference* (pp. 1356-1359). IEEE.

Cummins, G. and M. P. Y. Desmulliez (2012). "Inkjet printing of conductive materials: a review." *Circuit world* 38(4), pp.193-213.

Cutress, I. (2020). "Better Yield on 5nm than 7nm, TSMC: Update on Defect Rates for N5." Retrieved Nov 22, 2021, from <https://www.anandtech.com/show/16028/better-yield-on-5nm-than-7nm-tsmc-update-on-defect-rates-for-n5>.

Dankoco, M. D., G. Y. Tesfay, E. Bènevent and M. Bendahan (2016). "Temperature sensor realized by inkjet printing process on flexible substrate." *Materials Science and Engineering: B* 205(1-5). 0921-5107.

Derby, B. (2010). "Inkjet printing of functional and structural materials: fluid property requirements, feature stability, and resolution." *Annual Review of Materials Research* 40(395-414). 1531-7331.

Domi, Y., H. Usui, K. Sugimoto and H. Sakaguchi (2019). "Effect of Silicon Crystallite Size on Its Electrochemical Performance for Lithium-Ion Batteries." *Energy Technology* 7(5): 1800946. 1802194-1804288.

Diethylene Glycol, A. A. (2021). Retrieved October 11, 2021, from <https://www.fishersci.com/us/en/catalog/search/products?keyword=diethylene+glycol>.

EGF, C. (2021). Retrieved October 11, 2021, from <https://www.fishersci.com/shop/products/ethylene-glycol-laboratory-fisher-chemical-2/E1774#?keyword=ethylene+glycol>.

Fedlheim, D. L., and Foss, C. A. (2001). Metal nanoparticles: synthesis, characterization, and applications. CRC press.

Felba, J., K. Nitsch, T. Piasecki, P. Paluch, A. Moscicki and A. Kinart (2009). The influence of thermal process on electrical conductivity of microstructures: Made by ink-jet painting with the use of ink containing nano sized silver particles, *9th IEEE Conference on Nanotechnology (IEEE-NANO)* (pp. 408-411). IEEE.

Ferguson, G. S., M. K. Chaudhury, G. B. Sigal and G. M. Whitesides (1991). "Contact adhesion of thin gold films on elastomeric supports: cold welding under ambient conditions." *Science* **253**(5021): 776-778. 0036-8075.

Gao, M., Li, L., and Song, Y. (2017). Inkjet printing wearable electronic devices. *Journal of Materials Chemistry C*, **5**(12), 2971-2993.

Ghosh, S. (2017). Atmospheric-Pressure In Situ Plasma Reduction and Patterning of Metal-Ion Containing Polymers, PhD Dissertation. Case Western Reserve University.

Glycol, D. (2021). Retrieved October 11, 2021, from <https://www.fishersci.com/shop/products/bis-2-hydroxyethyl-ether-99-acros-organics-3/AC121160010#?keyword=111-46-6>.

Glycol, T. (2021). Retrieved October, 11, 2021, from <https://www.fishersci.com/shop/products/triethylene-glycol-99-acros-organics-4/AC139590010#?keyword=triethylene+glycol>.

Gräbner, D., Tintelott, M., Dumstorff, G., and Lang, W. (2017). Low-cost thin and flexible screen-printed pressure sensor. *Multidisciplinary Digital Publishing Institute Proceedings*, **1**(4), 616.

Hansen, C. J., Saksena, R., Kolesky, D. B., et al. (2013). Inkjet Printing: High-Throughput Printing via Microvascular Multinozzle Arrays (Adv. Mater. 1/2013). *Advanced Materials*, **25**(1), 2-2.

Hannah, R. L. and S. E. Reed (1992). Strain gage users' handbook, Springer Science and Business Media.

He, B. B. (2018). Two-dimensional X-ray diffraction, John Wiley & Sons.

Herrmann, J., K. H. Müller, T. Reda, G. R. Baxter, B. d. Raguse, G. De Groot, R. Chai, M. Roberts and L. Wiczorek (2007). "Nanoparticle films as sensitive strain gauges." *Applied Physics Letters* **91**(18): 183105. 180003-186951.

Hu, X., S. Wang, H. Zhang, Y. Wang, C. Hang, J. Wen and Y. Tian (2021). "Silver flake/polyaniline composite ink for electrohydrodynamic printing of flexible heaters." *Journal of Materials Science: Materials in Electronics* **32**(23): 27373-27383. 21573-27482X.

Jabari, E., Ahmed, F., Liravi, F., Secor, E. B., Lin, L., and Toyserkani, E. (2019). 2D printing of graphene: a review. *2D Materials*, **6**(4), 042004.

Jahn, S. F., T. Blaudeck, R. R. Baumann, A. Jakob, P. Ecorchard, T. Ruffer, H. Lang and P. Schmidt (2010). "Inkjet printing of conductive silver patterns by using the first aqueous particle-free MOD ink without additional stabilizing ligands." *Chemistry of Materials* **22**(10): 3067-3071. 0897-4756.

Jang, J. H. and J. I. Han (2017). "Cylindrical relative humidity sensor based on polyvinyl alcohol (PVA) for wearable computing devices with enhanced sensitivity." *Sensors and Actuators A: Physical* **261**(268-273). 0924-4247.

Kamyshny, Alexander and Magdassi, Shlomo (2014). Conductive nanomaterials for printed electronics. *Small*, **10**(17), 3515-3535.

Kravchuk, O., Y. Bobitski and M. Reichenberger (2016). Electrical sintering of inkjet printed sensor structures on polyimide substrate, *IEEE 36th International Conference on Electronics and Nanotechnology (ELNANO)* (pp. 104-106). IEEE.

Lee, H., D. Lee, J. Hwang, D. Nam, C. Byeon, S. H. Ko and S. Lee (2014). "Silver nanoparticle piezoresistive sensors fabricated by roll-to-roll slot-die coating and laser direct writing." *Optics Express* **22**(8): 8919-8927. 1094-4087.

Lee, Y.-D. and W.-Y. Chung (2009). "Wireless sensor network based wearable smart shirt for ubiquitous health and activity monitoring." *Sensors and Actuators B: Chemical* **140**(2): 390-395. 0925-4005.

- Lee, Y. K., J. Kim, Y. Kim, J. W. Kwak, Y. Yoon and J. A. Rogers (2017). "Room temperature electrochemical sintering of Zn microparticles and its use in printable conducting inks for bioresorbable electronics." *Advanced Materials* **29**(38): 1702665. 1700935-1709648.
- Li, Y., R. Torah, S. Beeby and J. Tudor (2012). An all-inkjet printed flexible capacitor on a textile using a new poly (4-vinylphenol) dielectric ink for wearable applications, *SENSORS, 2012 IEEE* (pp. 1-4). IEEE.
- Liu, Q., B. Tian, C. Luo, J. Liang and W. Wu (2020). "Printed Flexible Heaters-Based Thermo-therapy Platform for Multiduty Thermal Management." *Advanced Materials Technologies* **5**(8): 2000278. 2002365-2000709X.
- Lu, D., T. L. Liu, J. K. Chang, D. Peng, Y. Zhang, J. Shin, T. Hang, W. Bai, Q. Yang and J. A. Rogers (2019). "Transient Light-Emitting Diodes Constructed from Semiconductors and Transparent Conductors that Biodegrade Under Physiological Conditions." *Advanced Materials* **31**(42): 1902739. 1900935-1909648.
- Lu, Y., J. Y. Huang, C. Wang, S. Sun and J. Lou (2010). "Cold welding of ultrathin gold nanowires." *Nature Nanotechnology* **5**(3): 218-224. 1748-3395.
- Lue, J. T. (2001). A review of characterization and physical property studies of metallic nanoparticles. *Journal of physics and chemistry of solids*, **62**(9-10), 1599-1612.
- Magdassi, S., M. Grouchko, O. Berezin and A. Kamyshny (2010). "Triggering the sintering of silver nanoparticles at room temperature." *ACS Nano* **4**(4): 1943-1948. 1936-0851.
- Maiwald, M., C. Werner, V. Zoellmer and M. Busse (2010). "INKtelligent printed strain gauges." *Sensors and Actuators A: Physical* **162**(2): 198-201. 0924-4247.
- Mattana, G., T. Kinkeldei, D. Leuenberger, C. Ataman, J. J. Ruan, F. Molina-Lopez, A. V. Quintero, G. Nisato, G. Tröster and D. Briand (2013). "Woven temperature and

humidity sensors on flexible plastic substrates for e-textile applications." *IEEE Sensors Journal* **13**(10): 3901-3909. 1530-3437X.

Meier, H., U. Löffelmann, D. Mager, P. J. Smith and J. G. Korvink (2009). "Inkjet printed, conductive, 25 μm wide silver tracks on unstructured polyimide." *physica status solidi (a)* **206**(7): 1626-1630. 1862-6300.

Michel, T. R., M. J. Capasso, M. E. Cavusoglu, J. Decker, D. Zeppilli, C. Zhu, S. Bakrania, J. A. Kadlowec and W. Xue (2020). "Evaluation of porous polydimethylsiloxane/carbon nanotubes (PDMS/CNTs) nanocomposites as piezoresistive sensor materials." *Microsystem Technologies* **26**(4): 1101-1112. 1432-1858.

Mitra, D., R. Thalheim and R. Zichner (2021). "Inkjet Printed Heating Elements Based on Nanoparticle Silver Ink with Adjustable Temperature Distribution for Flexible Applications." *physica status solidi (a)* **218**(17): 2100257. 2101862-2106300.

Molina-Lopez, F., A. V. Quintero, G. Mattana, D. Briand and N. F. de Rooij (2012). "P1. 8.6 All-additive Inkjet Printed Humidity and Temperature Sensors Fabricated and Encapsulated at Foil Level." *Proceedings IMCS 2012*: 1122-1125.

Morris, B. A. (2016). *The science and technology of flexible packaging: multilayer films from resin and process to end use*, William Andrew.

Nayak, L., S. Mohanty, S. K. Nayak and A. Ramadoss (2019). "A review on inkjet printing of nanoparticle inks for flexible electronics." *Journal of Materials Chemistry C* **7**(29): 8771-8795.

Nir, M. M., Zamir, D., Haymov, I., Ben-Asher, L., Cohen, O., Faulkner, B., and De La Vega, F. (2010). Electrically conductive inks for inkjet printing. *the chemistry of inkjet inks*, 225-254.

Pantelopoulos, A. and N. G. Bourbakis (2009). "A survey on wearable sensor-based systems for health monitoring and prognosis." *IEEE Transactions on Systems, Man, and Cybernetics, Part C (Applications and Reviews)* **40**(1): 1-12. 1094-6977.

Patel, S., H. Park, P. Bonato, L. Chan and M. Rodgers (2012). "A review of wearable sensors and systems with application in rehabilitation." *Journal of Neuroengineering and Rehabilitation* **9**(1): 1-17. 1743-0003.

Paunonen, S. (2013). "Strength and barrier enhancements of cellophane and cellulose derivative films: a review." *BioResources* **8**(2): 3098-3121. 1930-2126.

Peterson, S. M. (2007). Influence of scale, geometry, and microstructure on the electrical properties of chemically deposited thin silver films, PhD Dissertation. University of Oregon.

Phuah, E. W. C., W. L. Hart, H. Sumer and P. R. Stoddart (2020). "Patterning of biomaterials by aerosol jet printing: a parametric study." *Bioprinting* **18**: e00081. 02405-08866.

Piel, A. (2017). Plasma physics: an introduction to laboratory, space, and fusion plasmas, Springer.

Pramanik, C. and H. Saha (2006). "Piezoresistive pressure sensing by porous silicon membrane." *IEEE Sensors Journal* **6**(2): 301-309. 1530-1437X.

Radwan, A. N., Sui, Y., and Zorman, C. A. (2021, June). An Inkjet Printed Ag Strain Gauge on Flexible Cellophane using a Metal-Salt based Ink. In *2021 IEEE International Conference on Flexible and Printable Sensors and Systems (FLEPS)* (pp. 1-4). IEEE.

Radwan, A. N., Y. Sui and C. A. Zorman (2022). "Inkjet Printed Strain Gauges Fabricated Using AgNO₃/Ethylene Glycol-based Inks." *IEEE Sensors Journal*. 1530-437X.

Rahman, M. T., R. Moser, H. M. Zbib, C. V. Ramana and R. Panat (2018). "3D printed high performance strain sensors for high temperature applications." *Journal of Applied Physics* **123**(2): 024501. 020021-028979.

- Rausch, J., L. Salun, S. Griesheimer, M. Ibis and R. Werthschützky (2011). Printed resistive strain sensors for monitoring of light-weight structures, International Society for Optics and Photonics *Smart Sensor Phenomena, Technology, Networks, and Systems 2011*, **7982**(161-172). SPIE, 2011.
- Rudez, R., Pavlič, J., and Bernik, S. (2015). Preparation and influence of highly concentrated screen-printing inks on the development and characteristics of thick-film varistors. *Journal of the European Ceramic Society*, **35**(11), 3013-3023.
- Rumbach, P., D. M. Bartels, R. M. Sankaran and D. B. Go (2015). "The effect of air on solvated electron chemistry at a plasma/liquid interface." *Journal of Physics D: Applied Physics* **48**(42): 424001. 420022-423727.
- Schoner, C., Jahn, S. F., Jakob, A., Blaudeck, T., Lang, H., and Baumann, R. R. (2011). Concepts of metal-organic decomposition (MOD) silver inks for structured metallization by inkjet printing. *MRS Online Proceedings Library (OPL)*, **1**.
- Shin, D. Y., Lee, Y., & Kim, C. H. (2009). Performance characterization of screen printed radio frequency identification antennas with silver nanopaste. *Thin Solid Films*, **517**(21), 6112-6118.
- Silva, A. F., H. Paisana, T. Fernandes, J. Góis, A. Serra, J. F. J. Coelho, A. T. de Almeida, C. Majidi and M. Tavakoli (2020). "High Resolution Soft and Stretchable Circuits with PVA/Liquid-Metal Mediated Printing." *Advanced Materials Technologies* **5**(9): 2000343. 2002365-2000709X.
- Sinar, D. and G. K. Knopf (2018). "Printed graphene derivative circuits as passive electrical filters." *Nanomaterials* **8**(2): 123.
- Smith, P. J. and A. Morrin (2012). "Reactive inkjet printing." *Journal of Materials Chemistry* **22**(22): 10965-10970.

Somalu, M. R., Muchtar, A., Daud, W. R. W., and Brandon, N. P. (2017). Screen-printing inks for the fabrication of solid oxide fuel cell films: A review. *Renewable and Sustainable Energy Reviews*, 75(426-439).

Sui, Y. (2019). A Low-Temperature Printing Technology for Fabricating Electrically Conductive Structures and Devices Using Plasma-Activated Stabilizer-Free Inks, PhD Dissertation. Case Western Reserve University.

Sui, Y., Y. Dai, C. C. Liu, R. M. Sankaran and C. A. Zorman (2019). "A New Class of Low-Temperature Plasma-Activated, Inorganic Salt-Based Particle-Free Inks for Inkjet Printing Metals." *Advanced Materials Technologies* 4(8): 1900119. 1902365-1900709X.

Sui, Y., S. Ghosh, C. Miller, D. Pappas, R. Mohan Sankaran and C. A. Zorman (2018). "Tunable resistivity in ink-jet printed electrical structures on paper by plasma conversion of particle-free, stabilizer-free silver inks." *Journal of Vacuum Science and Technology A: Vacuum, Surfaces, and Films* 36(5): 051302. 050734-052101.

Sui, Y., A. Hess-Dunning, **A. N. Radwan**, R. M. Sankaran and C. A. Zorman (2022). "Engineering the surface morphology of inkjet printed Ag by controlling solvent evaporation during plasma conversion of AgNO₃ inks." *Journal of Materials Chemistry C* 10(13): 5257-5265.

Sui, Y., A. Hess-Dunning, R. M. Sankaran and C. A. Zorman (2020). "Inkjet-Printed Hydrogen Peroxide Sensor With Sensitivity Enhanced by Plasma Activated Inorganic Metal Salt Inks." *Journal of Microelectromechanical Systems* 29(5): 1026-1031. 1057-7157.

Sui, Y., L. P. Kreider, K. M. Bogie and C. A. Zorman (2019). "Fabrication of a silver-based thermistor on flexible, temperature-sensitive substrates using a low-temperature inkjet printing technique." *IEEE Sensors Letters* 3(2): 1-4. 2475-1472.

Sui, Y., **A. N. Radwan**, A. Gopalakrishnan, K. Dikshit, C. J. Bruns, C. A. Zorman and G. L. Whiting (2022). "A Reactive Inkjet Printing Process for Fabricating

Biodegradable Conductive Zinc Structures." *Advanced Engineering Materials*: 2200529. 2201438-2201656.

Sui, Y. and C. A. Zorman (2020). "Inkjet printing of metal structures for electrochemical sensor applications." *Journal of The Electrochemical Society* **167**(3): 037571. 031945-037111.

Syaizwadi, S. M., S. S. Noradilah, M. G. M. Sabri, W. A. W. Rafizah, K. Syara and O. J. Lee (2018). Effect of sintering temperature on zinc oxide varistor ceramics, *IOP Conference Series: Materials Science and Engineering*, vol. 440, no. 1, p. 012037. IOP Publishing, 2018.

Tan, M. J., C. Owh, P. L. Chee, A. K. K. Kyaw, D. Kai and X. J. Loh (2016). "Biodegradable electronics: cornerstone for sustainable electronics and transient applications." *Journal of Materials Chemistry C* **4**(24): 5531-5558.

Tehrani, Z., Korochkina, T., Govindarajan, S., Thomas, D. J., O'Mahony, J., Kettle, J., ... and Gethin, D. T. (2015). Ultra-thin flexible screen printed rechargeable polymer battery for wearable electronic applications. *Organic Electronics*, **26**, 386-394.

Thibert, S., Jourdan, J., Bechevet, B., Chaussy, D., Reverdy-Bruas, N., and Beneventi, D. (2014). Influence of silver paste rheology and screen parameters on the front side metallization of silicon solar cell. *Materials science in semiconductor processing*, **2**(790-799).

Tiwari, S. K., S. Bhat and K. K. Mahato (2018). "Design and fabrication of screen printed microheater." *Microsystem Technologies* **24**(8): 3273-3281. 1432-1858.

Toriyama, T. and S. Sugiyama (2003). "Single crystal silicon piezoresistive nano-wire bridge." *Sensors and Actuators A: Physical* **108**(1-3): 244-249. 0924-4247.

Trease, R. E., and Dietz, R. L. (1972). Rheology of pastes in thick-film printing. *Solid state technology*, **15**(1), 39.

Triethylene-glycol-for-synthesis. (2021). Retrieved October 11, 2021, from https://www.emdmillipore.com/US/en/product/Triethylene-glycol,MDA_CHEM-808245.

Wang, X., Y. Cui, Y. Tao, H. Yang and J. Zhao (2020). "A Flexible Low-Pass Filter Based on Laser-Induced Graphene." *Journal of Electronic Materials* **49**(11): 6348-6357. 1543-6186X.

Yang, P. and H. J. Fan (2020). "Inkjet and extrusion printing for electrochemical energy storage: a minireview." *Advanced Materials Technologies* **5**(10): 2000217. 2002365-2000709X.

Zapka, Werner (2017). *Handbook of industrial inkjet printing: a full system approach*. John Wiley & Sons.

Zeng, P., Tian, B., Tian, Q., Yao, W. et al. (2019). Screen-printed, low-cost, and patterned flexible heater based on Ag fractal dendrites for human wearable application. *Advanced Materials Technologies*, **4**(3), 1800453.

Zhang, N., Huang, C., Wan, S., et al. (2019). A novel flexible silver heater fabricated by a solution-based polyimide metallization and inkjet-printed carbon masking technique. *ACS Applied Electronic Materials*, **1**(6), 928-935.

Zheng, Y. F., X. N. Gu and F. Witte (2014). "Biodegradable metals." *Materials Science and Engineering: R: Reports* **77**(1-34). 0927-0796X.

Zhu, X., Z. Qian, X. Chen, L. Liu, C. Sheng and W. Gu (2020). "Electrohydrodynamics-Printed Silver Nanoparticle Flexible Pressure Sensors With Improved Gauge Factor." *IEEE Sensors Journal* **21**(5): 5836-5844. 1530-5437X.

Zlebič, Č., L. Zivanov, A. Menićanin, N. Blaz and M. Damnjanović (2016). "Inkjet printed resistive strain gages on flexible substrates." *Facta universitatis-series: Electronics and Energetics* **29**(1): 89-100.

Zulfiqar, M. H., A. Alam, M. M. Saleem, M. Zubair, M. Q. Mehmood and K. Riaz (2021). "Tunable and foldable paper-based passive electronic components and filter circuits." *Cellulose* **28**(15): 9959-9970. 1572-9882X.